A COUPLED-MOMENTUM METHOD TO MODEL BLOOD FLOW AND VESSEL DEFORMATION IN HUMAN ARTERIES: APPLICATIONS IN DISEASE RESEARCH AND SIMULATION-BASED MEDICAL PLANNING

A DISSERTATION
SUBMITTED TO THE DEPARTMENT OF MECHANICAL ENGINEERING
AND THE COMMITTEE ON GRADUATE STUDIES
OF STANFORD UNIVERSITY
IN PARTIAL FULFILLMENT OF THE REQUIREMENTS
FOR THE DEGREE OF
DOCTOR OF PHILOSOPHY

C. Alberto Figueroa

March 2006

I certify that I have read this dissertation and that, in my opinion, it is fully adequate in scope and quality as dissertation for the degree of Doctor of Philosophy.

Charles A. Taylor (Principal Advisor)
Associate Professor of Bioengineering, Surgery and Mechanical Engineering (by courtesy)

I certify that I have read this dissertation and that, in my opinion, it is fully adequate in scope and quality as dissertation for the degree of Doctor of Philosophy.

Christopher K. Zarins
Professor of Surgery

I certify that I have read this dissertation and that, in my opinion, it is fully adequate in scope and quality as dissertation for the degree of Doctor of Philosophy.

Kenneth E. Jansen
Associate Professor of Mechanical, Aeronautical and Nuclear Engineering
Rensselaer Polytechnic Institute

Approved for the University Committee on Graduate Studies:

Abstract

Blood velocity and pressure fields in large arteries are greatly influenced by the deformability of the vessel. Moreover, wave propagation phenomena in the cardiovascular system can only be described considering wall deformability since blood is usually described as an incompressible fluid. However, computational methods for simulating blood flow in three-dimensional models of arteries have either considered a rigid wall assumption for the vessel or significantly simplified or reduced geometries when modeling blood flow in deformable arteries. Computing blood flow in deformable domains using standard techniques like the ALE method remains a formidable problem for large, realistic anatomic and physiologic models of the cardiovascular system.

We have developed a new method termed the Coupled-Momentum Method for Fluid-Solid Interaction to simulate blood flow in three-dimensional deformable models of arteries. In this method, the effect of the vessel wall boundary is added in a monolithic way to the fluid equations using a shear-enhanced membrane model for the wall, resulting in a remarkably robust scheme. We present here the mathematical formulation of the method and discuss issues related to the fluid-solid coupling, membrane formulation, time integration method, and boundary and initial conditions.

We have verified the method by comparing it against Womersley's analytical solution for pulsatile flow in a straight cylindrical elastic vessel, and have obtained excellent agreement between the numerical and analytical solutions.

The method was then applied to a number of different geometries, ranging from simple, idealized models to large, patient-specific models with over 1 million element finite element meshes. The simple geometries have provided a clear framework to illustrate concepts like wave propagation phenomena, impact of boundary conditions, etc. The patient-specific models have demonstrated the potential of the method to be applied to surgical-planning and disease-research problems in a clinically-relevant timeframe.

This research shows great promise for the application of computational methods representing fluid-solid interactions to clinical applications. We have suggested future directions to expand the work developed in this thesis to obtain even more realistic models of blood flow in arteries, while still maintaining an emphasis on computational efficiency so essential to clinical applications.

Acknowledgments

I would like to express my sincere gratitude to the following individuals and organizations:

Professor Charles A. Taylor, my Ph.D. advisor and mentor. He has provided me with guidance and support during the course of my studies and has always been open to exciting discussions about research. I have learned many valuable lessons from him; I will keep Professor Taylor as a reference for academic excellence and as a close friend for years to come.

Professor Kenneth E. Jansen, for the help provided in the many phone conference calls during the course of this work. He has given me very valuable programming advice to incorporate the method developed in this thesis into the PHASTA© code.

Professor Christopher K. Zarins, for encouraging and helping me to find the biological and clinical applications of the methods developed in this thesis. He has always been able to find some time for me in his busy schedule at the Stanford Hospital.

Professor Thomas J.R. Hughes, for his decisive guidance during a number of critical stages of this research. His authority and accomplishments in the field of

Computational Mechanics have always been a reference for me. It has been an honor to have him as a collaborator in this work.

Professor Charbel Farhat, for his suggestions to this work and for serving on my thesis committee. His work in fluid-structure interaction algorithms will serve as a guidepost for my own research.

Professor Juan J. Alsonso, for serving as chair of my thesis committee.

Irène Vignon, for her help, support, and friendship during all these years. Working with her has been very exciting and productive. She has become a friend for life and I will always remember very fondly our Stanford years.

Rubén Juanes. We have been closest friends since our high school years. He has always been there for me, in the good and bad times. I deeply admire both his scientific and human sides.

Juanjo Mata, for all the fun moments, stories and friendship we have shared since I arrived in California. He has been a terrific roommate and is now one of my best friends.

Natalia Camprubí, for all the love, help and support she gave me for years.

Chris Cheng, for being such a cool housemate and for giving me so many valuable pieces of advice over the last year.

The friends that have shared with me many discussions, activities, trips, etc. over the last six years: César Sánchez and Teresa Madrid, Juan Luis Alonso and

Marsida Saraci, Pablo Molinero, Víctor Calo and Natacha Poggio, José Manuel Garde, Willow Sussex, Amit Mookerjee, Mario Galarreta and Álvaro Martínez.

Nacho Ardá, for his friendship and efforts to keep in touch despite the long distance.

My friends and lab-mates of the Stanford Cardiovascular Biomechanics Research Lab. They have made the lab a very fun place to work in. Special thanks to Nathan Wilson, for his assistance with software development, and also to John LaDisa, Peter Feenstra, Bev Tang, Ryan Spilker, Alison Marsden, Andrea Les, Chase Yarbrough, Hyun Jin Kim, Shyla Barker, Mary Draney, Mary O'Connell, Joan Greve, Rashmi Raghu and Erik Bekkers.

My mentors of the Civil Engineering School of the University of La Coruña (Spain): Professors Manuel Casteleiro, Fermín Navarrina and Ignasi Colominas. They introduced me to the area of Computational Mechanics and encouraged me to pursue a Ph.D. degree in the United States. I owe them a great deal of gratitude for their guidance during the early years of my graduate studies.

The Pedro Barrié de la Maza Foundation, for their financial support during my first year and a half in Stanford University. They awarded me a scholarship that funded my Masters of Science degree. Without their support, I would not have achieved this goal.

The National Science Foundation for supporting my research during the last three and a half years of my Ph.D.

Finally, I owe, by far, the greatest gratitude to my family: my parents José Luis Figueroa and Divina Álvarez; my sister Judith and my brother Adrián. They have taught me the most valuable lessons in life, more than any academic learning. They have supported me with endless love during my entire life, and have managed to make me feel them very close every day, despite the long distance.

A mis padres, por su continuo amor y por todos los sacrificios que han hecho por mí.

Table of Contents

List of tables

List of figures

Number *Page*

Chapter 1

Chapter 1. Introduction

1.1 Motivation

Congenital and acquired cardiovascular diseases represent one of the most important causes of morbidity and mortality in the world. Congenital heart disease affects more than 33,000 children per year in the United States alone and is the leading cause of death from birth defects during infancy. Among the acquired cardiovascular diseases, atherosclerosis is the most common manifestation. This disease, often characterized by arterial narrowing and reductions in blood flow, accounts for 75% of all cardiovascular disease-related deaths in the United States [1]. While the risk factors of this disease such as nicotine, high cholesterol and familial history are systemic (i.e., they are present in the entire cardiovascular system), the manifestations (typically in the form of plaque deposits) are localized in areas of complex flow like the coronary, carotid, abdominal and femoral arteries. Hemodynamic quantities such as blood velocity, pressure and shear stress play a very important role in the localization of disease and in the efficacy of treatments [2,3,4,5]. For both congenital and acquired cardiovascular diseases, a deep understanding of the altered blood flow conditions can enable the optimization of interventions employed to treat these conditions.

In recent years, computational techniques have been used widely by researchers seeking to simulate blood flow in three-dimensional models of arteries. Applications include disease research where fluid mechanical conditions are correlated to regions prone to atherosclerosis [6,7,8], medical device design where the interactions between a device and the blood stream are modeled [9,10,11] and, more recently, surgical planning [12,13,14,15].

However, the tools and methods used to model blood flow in the cardiovascular system are in many cases still too crude and new developments are required in order to improve the accuracy and faithfulness of the results. Very often, classic engineering fluid mechanics formulations are used to approximate the behavior of blood flow in the cardiovascular system, without paying enough attention to a number of factors that drastically affect the faithfulness of the simulations:

1. Model construction from medical image data. This component of the simulation process determines the geometry used in the computation, and it is therefore very important to reproduce as closely as possible the actual anatomy of the patient.
2. Boundary conditions. Prescribing adequate inflow and outflow conditions enables computations at physiologic levels of pressure and with realistic flow division between the different vascular branches.
3. Fluid-Solid Interactions between the blood and the vessel wall. The impact of vessel wall deformability on the wave propagation phenomena present in the blood flow, as well as on other quantities, such as pressure pulse, flow distribution between systole and diastole, wall shear stress, dynamic pressure, etc. makes it a fundamental aspect to be considered in the simulation process.

The work developed in this thesis in focused on this latter factor. A new formulation to model blood flow in deformable models of arteries is presented, implemented, and applied to various problems, including large patient-specific models of the vasculature, with applications to disease research and simulation-based medical planning.

1.2 The Importance of Including Wall Deformability when Modeling Blood Flow in Arteries

Most computational techniques applied to model blood flow in three-dimensional, patient-specific models of arteries have either examined only the velocity field (not the pressure field), treating the vessel walls of patient-specific models as rigid [16,17,18,19,20], or have considered significantly simplified or reduced geometries of deformable wall models [21,22]. The rigid-wall approximation is made in large part because of the difficulty of solving the coupled blood flow / vessel deformation problem and is justified by the observation that, under normal conditions, wall deformability does not significantly alter the velocity field [21]. However, this observation was made for arteries where wall motion is small and may not be valid for arteries where deformations are larger (e.g., the thoracic aorta). Perhaps most importantly, the assumption of rigid vessel walls precludes wave propagation phenomena (see Figure 1-1), fundamentally changes the character of the resultant solutions, and results in difficulties in coupling three-dimensional domains with domains described using one-dimensional wave propagation methods [23,24].

Therefore, it is clear that in order to accurately represent some of the fundamental characteristics of blood flow in the cardiovascular system, vessel wall deformability must be taken into account in the mathematical formulation of the problem.

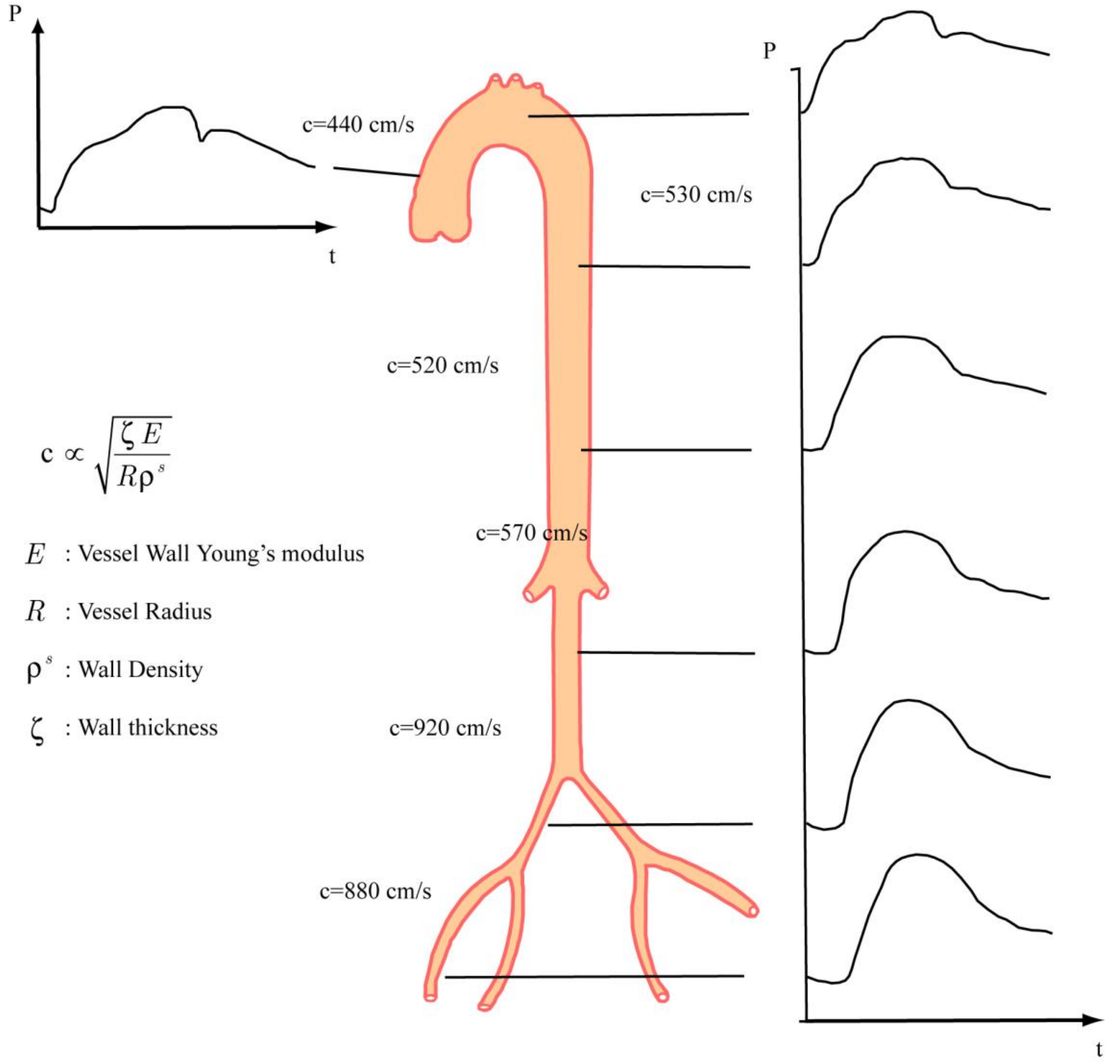

Figure 1-1: Changes in blood pressure pulse and blood pressure wave speed due to variations in the compliance and geometry of the blood vessels. Modified from [25]. c represents the speed of the pressure and flow waves in the arteries.

1.3 Models of the Cardiovascular System

Vessel wall deformability can be easily included when modeling the cardiovascular system using reduced-order methods like the Lumped Parameter Method [26,27,28] or One-Dimensional Formulations (linear and non-linear) ([29,30,31,32]). However, these techniques cannot provide the level of information about many of the different variables and their derived quantities (like wall shear stress, or wall tensile stress) that are of interest to vascular biologists and physicians. These variables can only be obtained using three-dimensional formulations where patient-specific models of the geometry of the patient can be generated and the flow fields and derived quantities can be obtained. However, the increase in computational cost of three-dimensional techniques is very significant compared to that of reduced-order methods, especially when the combined problem of blood flow and vessel wall deformation is considered.

One of the better-known methods for including wall deformability in three-dimensional geometric models is the ALE (Arbitrarily Lagrangian - Eulerian) formulation for fluid-structure interaction problems [33,34]. Exemplary work describing the development and application of ALE methods includes that of Tezduyar ([35,36]) and Farhat ([37,38]). Significant progress has been made in recent years in solving blood flow problems in deformable domains using ALE methods (see, e.g.,[39,40,41,42]). A theoretical analysis of this method can be found in [43] and [44]. However, ALE formulations are computationally expensive when considering large models of the vasculature and often not very robust since they necessitate the continual updating of the geometry of the fluid and structural elements. Other formulations that account for wall deformability are based on the Immersed Boundary Method [45,46] or on transpiration techniques based on linearization principles [47,48].

Modeling the three-dimensional blood flow in compliant arteries, which are tethered to and supported by surrounding tissue and organs, is extremely challenging for a number of additional reasons: geometry acquisition, accurate constitutive description of the behavior of the tissue, and outflow boundary conditions are only a few examples. Application of fluid-structure interaction methods in simulation-based medical planning is additionally demanding in that multiple surgical interventions need to be modeled, solved, analyzed, and compared in a clinically relevant time-frame (hours). Simpler methods for incorporating wall motion are essential for these applications.

1.4 Proposed Methodology

In this thesis, we present a new formulation for modeling blood flow in deformable arteries called the Coupled Momentum Method for Fluid-Solid Interaction problems (CMM-FSI). This formulation starts from a conventional stabilized finite element formulation for the Navier-Stokes equations in a rigid domain and modifies it in such a way that the deformability of the wall domain surrounding the fluid is taken into account. With this approach, the effects of the vessel wall motion are embedded in the weak form representing the blood flow resulting in a single weak form for the combined problem. As a result of this, only minimal changes in the stiffness matrices and residuals of the rigid wall finite element model are required to incorporate the effects of the wall motion. This approach results in a tractable, efficient and robust procedure to simulate fluid-structure interactions in three-dimensional models of the cardiovascular system. The computational effort is comparable to that of rigid wall formulations while at the same time it respects the essential physics and enables realistic simulation of wave-propagation phenomena in the arterial system as well as a linearized description of wall deformation.

1.5 Contributions

The main contributions of this thesis are:

1. The development of a new mathematical formulation to model blood flow in deformable models of arteries. This formulation utilizes a single variational form for the combined blood flow/vessel wall motion problem, using identical degrees-of-freedom for the lateral surface of the fluid domain and the solid domain. A shear-enhanced membrane element for the vessel wall has been developed, as well as an extension of the generalized-α time integration algorithm.
2. The implementation of this mathematical formulation into a pre-existing Stabilized Finite Element Solver for Fluids (PHASTA$^{©}$[49]).
3. The verification of the mathematical formulation by comparing it against the results provided by Womersley's mathematical model of pulsatile blood flow in a deformable cylindrical vessel.
4. The application of the formulation to a number of different models, ranging from simple idealized geometries to large, patient-specific models of various parts of the cardiovascular system, with particular emphasis on disease-research and simulation-based medical planning applications.

1.6 Organization of Thesis

The remainder of this thesis is organized in the following manner: Chapter 2 presents some of the fundamental concepts related to the mathematics and physics of pulsatile flow in deformable vessels. This is done by first reviewing, in detail, Womersley's deformable wall theory. Then, a brief summary of the equations describing general three-dimensional coupled fluid-solid interactions is provided. Chapter 3 presents the Finite Element formulation of the CMM-FSI. This includes the development of a new single variational formulation for the combined problem, the Finite Element model for the vessel wall and the adaptation of the generalized-α time integration algorithm for this formulation. Chapter 4 presents the verification of the CMM-FSI by comparing it against Womersley's deformable wall mathematical theory. Chapter 5 presents the application of the method to problems of increasing complexity. The impact of wall deformability and outflow boundary conditions is analyzed and discussed for a number of these problems. The last three models of this chapter correspond to disease-research and simulation-based medical planning applications. Lastly, Chapter 6 presents conclusions and suggestions for future work.

Chapter 2

Chapter 2. Mathematics and Physics of Pulsatile Flow in Deformable Vessels

2.1 Introduction

In this chapter, we first review in detail Womersley's deformable wall theory. Then, a brief summary of the equations describing general three-dimensional fluid-solid interactions is provided. These two topics supply the necessary background to the work developed in this thesis. The significance of Womersley's theory can be summarized in three points:

1. It represents an excellent framework to understand some of the basic principles that govern wave propagation phenomena and blood flow velocity patterns in the cardiovascular system.
2. It has provided our inspiration to derive the theory of the Coupled-Momentum Method. As we will see in Chapter 3, we have adopted the same strategy used by Womersley to couple the fluid and solid equations together. In his work, he defined a body force for the solid equations using the pressure and shear stress fields of the fluid domain (see Section 2.2.2.2, equation(2.81)) to derive the analytical solution. We have generalized this approach to arbitrary geometries and flow regimes.
3. Womersley's theory provides the mathematical model to perform the verification study for the Coupled-Momentum Method performed in Chapter 4 of this thesis.

We have adopted Zamir's book [50] as the starting point for the work developed in Section 2.2.

Womersley's analytical solution is only applicable to axisymmetric flows in cylindrical, straight, long vessels; therefore, we need to resort to numerical formulations to solve the problem of blood flow and vessel wall deformation in arbitrary three-dimensional geometries. In Section 2.3, we briefly describe the general nonlinear partial differential equations governing flow in three-dimensional deformable domains. In general these problems require the modification of the Eulerian formulation used to represent flows in fixed grids. We provide a schematic description of how these problems are treated with the well-known *Arbitrary Lagrangian-Eulerian* (ALE) formulation. However, the computational cost of this formulation for large, patient-specific models of the vasculature is very high, making it expensive to use in surgical planning applications since in these cases multiple surgical interventions need to be modeled, solved, analyzed, and compared in a clinically relevant time-frame (hours). This justifies the need for the formulation developed in this thesis (the CMM-FSI method) which represents a computationally efficient alternative to ALE formulations.

2.2 Womersley Theory for Blood Flow in Elastic Tubes

The pumping action of the heart produces a driving force that pushes blood through the arterial tree. This driving force, or pressure differential, can be decomposed into a constant part that does not vary in time and that produces a steady flow forward as in Poiseuille flow, plus an oscillatory part that moves the blood back and forth, with zero net flow over each cardiac cycle. We can use the terms *steady* and *oscillatory* to refer to these two components of the flow. We can also decompose a given pressure gradient $k(t)$ into the steady, k_s, and oscillatory, $k_\phi(t)$, components

$$\frac{\partial p}{\partial z} = k(t) = k_s + k_\phi(t) \tag{2.1}$$

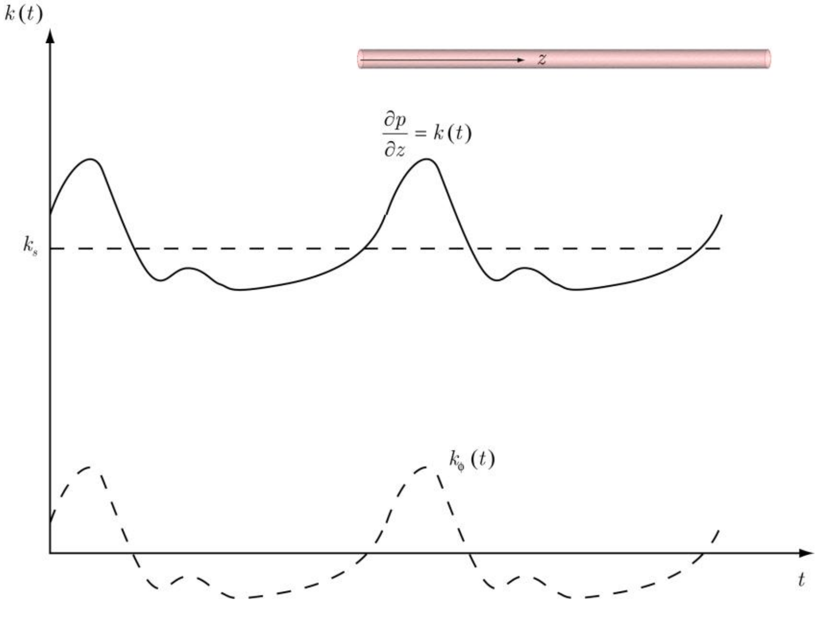

Figure 2-1: Decomposition of the driving force (pressure gradient) into its steady and oscillatory components.

as illustrated in Figure 2-1.

The simplifications to the Navier-Stokes equations that we consider in this chapter will be such that the resulting equations are linear. As a result, we can decompose flow into steady and oscillatory parts by using linear superposition.

It is important to note that the expressions derived in this chapter for the different flow variables correspond only to the oscillatory component of the total solution. Once the oscillatory components of the velocity field in the radial (u_ϕ) and longitudinal (w_ϕ) directions are obtained, we reconstruct the total solution by adding these components to the steady (Poiseuille) solution profile. This latter solution provides the longitudinal velocity w_s generated by a steady pressure gradient in a circular, straight vessel of radius *R*. Its expression is given by:

$$w_s(r) = \frac{k_s}{4\mu}\left(r^2 - R^2\right) \tag{2.2}$$

Therefore, the total solution for the different flow velocity components is:

- Longitudinal

$$w = w_s(r) + w_\phi(r,z,t) = \frac{k_s}{4\mu}\left(r^2 - R^2\right) + w_\phi(r,z,t) \tag{2.3}$$

- Radial

$$u = u_s(r) + u_\phi(r,z,t) = u_\phi(r,z,t) \tag{2.4}$$

The objective of this chapter is to obtain the expressions for the oscillatory components of the flow velocity in the longitudinal (w_ϕ) and radial (u_ϕ) directions. We will also obtain expressions for the displacement of the wall in the longitudinal (ζ_ϕ) and radial (ξ_ϕ) directions. Note that these components will be purely oscillatory as well.

For the sake of notational simplicity, we omit the oscillatory subscript ϕ from all the variables considered hereafter.

2.2.1 Equations of Motion for the Rigid Wall Theory

We start by reviewing the expressions of Womersley's rigid wall theory. The general mass and momentum conservation equations defining the incompressible Navier-Stokes equations can be greatly simplified under the following assumptions:

1. Cylindrical, axisymmetric straight vessel.
2. Constant in space (fully-developed) pressure gradient $\dfrac{\partial p}{\partial z}$.
3. Rigid walls.

Considering this, the velocity vector $\vec{v}$ in cylindrical coordinates is simply

$$\vec{v} = \begin{Bmatrix} v_r \\ v_\varphi \\ v_z \end{Bmatrix} = \begin{Bmatrix} 0 \\ 0 \\ w \end{Bmatrix} \tag{2.5}$$

The continuity equation is trivially satisfied and the momentum vector equation reduces to the longitudinal component given by:

$$\frac{\partial^2 w}{\partial r^2} + \frac{1}{r}\frac{\partial w}{\partial r} - \frac{\rho}{\mu}\frac{\partial w}{\partial t} = \frac{1}{\mu}\frac{\partial p}{\partial z} \tag{2.6}$$

where ρ and μ represent the density and viscosity of the fluid, respectively.

If a complex exponential is used to represent each mode of the oscillatory pressure gradient, we have

$$\frac{\partial p}{\partial z} = A e^{i\omega t} \tag{2.7}$$

where A represents the amplitude of the oscillation and ω its frequency. Now, if we consider a separation of variables for the unknown velocity w of the form

$$w(r,t) = W(r) e^{i\omega t} \tag{2.8}$$

we obtain the following (complex) ordinary differential equation

$$\frac{d^2 W}{dr^2} + \frac{1}{r}\frac{dW}{dr} - \frac{i\rho\omega}{\mu} W = \frac{A}{\mu} \tag{2.9}$$

Now, we introduce the Womersley number to simplify this equation further. The Womersley number is a dimensionless parameter that represents the ratio between oscillatory inertial forces and viscous forces:

$$\alpha = \sqrt{\frac{\rho\omega}{\mu}} R \tag{2.10}$$

Considering this, equation (2.9) can be rewritten as

$$\frac{d^2W}{dr^2}+\frac{1}{r}\frac{dW}{dr}-\frac{i\alpha^2}{R^2}W=\frac{A}{\mu} \tag{2.11}$$

Equation (2.11) is a form of Bessel's equation that has a known general solution. To obtain it, we need to perform a coordinate transformation to write this equation in the form of the standard Bessel equation, which is given by the following expression:

$$x^2y''+xy'+\left(x^2-n^2\right)y=0 \qquad \text{n} \geq 0 \tag{2.12}$$

The solution to this equation is given by

$$y=GJ_n(x)+HY_n(x) \tag{2.13}$$

where G and H are arbitrary constants and $J_n(x)$ and $Y_n(x)$ the Bessel functions of first and second kind (of order n), respectively. The expressions for the Bessel functions of order zero, (which are the ones we obtain after the coordinate transformation) are given by the following series expansions:

$$J_0(x)=1-\frac{x^2}{2^2}+\frac{x^4}{2^2\cdot 4^2}-\frac{x^6}{2^2\cdot 4^2\cdot 6^2}+\ldots \tag{2.14}$$

$$\begin{aligned} Y_0(x)&=\frac{2}{\pi}\left\{\ln\left(\frac{x}{2}\right)+\gamma\right\}J_0(x)\\ &+\frac{2}{\pi}\left\{\frac{x^2}{2^2}-\frac{x^4}{2^2\cdot 4^2}\left(1+\frac{1}{2}\right)+\frac{x^6}{2^2\cdot 4^2\cdot 6^2}\left(1+\frac{1}{2}+\frac{1}{3}\right)-\ldots\right\}, \quad \gamma=0.5772156\ldots \end{aligned} \tag{2.15}$$

If we introduce the following coordinate transformation:

$$\eta = i^{\frac{3}{2}}\alpha \frac{r}{R}, \qquad \eta^2 = i^3\alpha^2 \frac{r^2}{R^2} = -i\alpha^2 \frac{r^2}{R^2} \tag{2.16}$$

equation (2.11) can be rewritten as follows:

$$\eta^2 \frac{d^2W}{d\eta^2} + \eta \frac{dW}{d\eta} + \eta^2 W = \eta^2 \frac{A}{\mu}\frac{R^2}{\alpha^2} i \tag{2.17}$$

The solution to the previous equation is the sum of the solution of its homogeneous counterpart (identical to equation (2.12) with $n=0$) plus the particular solution

$$W_p = \frac{A}{\mu}\frac{R^2}{\alpha^2} i \tag{2.18}$$

Therefore, we have

$$W = W_h + W_p = GJ_0(\eta) + HY_0(\eta) + \frac{A}{\mu}\frac{R^2}{\alpha^2} i \tag{2.19}$$

The boundary conditions are

$$W(r = R) = W\left(\eta = i^{\frac{3}{2}}\alpha\right) = 0 \tag{2.20}$$

$$W(r = 0) = W(\eta = 0) < \infty \tag{2.21}$$

The second boundary condition gives $H=0$, since $Y_0(\eta = 0) = \infty$. Enforcing the boundary condition at $r=R$, we obtain:

$$GJ_0\left(i^{\frac{3}{2}}\alpha\right)+\frac{A}{\mu}\frac{R^2}{\alpha^2}i=0 \quad\Rightarrow\quad G=-\frac{A}{\mu}\frac{R^2}{\alpha^2}i\frac{1}{J_0\left(i^{\frac{3}{2}}\alpha\right)} \tag{2.22}$$

and therefore the final expression for the function $W(r)$ becomes:

$$\begin{aligned} W(r) &= -\frac{A}{\mu}\frac{R^2}{\alpha^2}i\frac{J_0\left(i^{\frac{3}{2}}\alpha\frac{r}{R}\right)}{J_0\left(i^{\frac{3}{2}}\alpha\right)}+\frac{A}{\mu}\frac{R^2}{\alpha^2}i= \\ &= \frac{A}{\mu}\frac{R^2}{\alpha^2}i\left[1-\frac{J_0\left(i^{\frac{3}{2}}\alpha\frac{r}{R}\right)}{J_0\left(i^{\frac{3}{2}}\alpha\right)}\right] \end{aligned} \tag{2.23}$$

Now, if we define

$$\Lambda = i^{\frac{3}{2}}\alpha \tag{2.24}$$

we can rewrite equation (2.23) as

$$W(r)=\frac{A}{\mu}\frac{R^2}{\alpha^2}i\left[1-\frac{J_0\left(\Lambda\frac{r}{R}\right)}{J_0(\Lambda)}\right] \tag{2.25}$$

and the final expression for the longitudinal velocity profile w becomes

$$\boxed{w(r,t)=\frac{A}{\mu}\frac{R^2}{\alpha^2}i\left[1-\frac{J_0\left(\Lambda\frac{r}{R}\right)}{J_0(\Lambda)}\right]e^{i\omega t}} \tag{2.26}$$

Normalizing the previous expression using the maximum centerline velocity of the Poiseuille flow with a steady pressure gradient k_s of the same magnitude as the amplitude of the oscillatory pressure gradient A, (i.e., $A = k_s$), we get:

$$\hat{w}(r,t) = \frac{w(r,t)}{w_s(r=0)} = \frac{4\mu w(r,t)}{-k_s R^2} = \frac{4i}{-\alpha^2}\left[1 - \frac{J_0\left(\Lambda \frac{r}{R}\right)}{J_0(\Lambda)}\right] e^{i\omega t} \tag{2.27}$$

Recalling the expression for the parameter Λ given by equation (2.24), we can express the normalized longitudinal velocity for pulsatile flow in a rigid cylindrical vessel as follows:

$$\boxed{\hat{w}(r,t) = \frac{-4}{\Lambda^2}\left[1 - \frac{J_0\left(\Lambda \frac{r}{R}\right)}{J_0(\Lambda)}\right] e^{i\omega t}} \tag{2.28}$$

2.2.2 Equations of Motion for the Deformable Wall Theory

2.2.2.1 Equations of motion for the blood flow

One of the fundamental differences between Womersley's solutions for rigid and deformable cylindrical vessels is the existence of a radial component of the velocity u in the deformable wall case. This component of the velocity is much smaller than the longitudinal velocity w, but is of critical importance, since it is intimately related with other important differences between the two sets of solutions, namely the existence of wave propagation phenomena in the deformable wall theory.

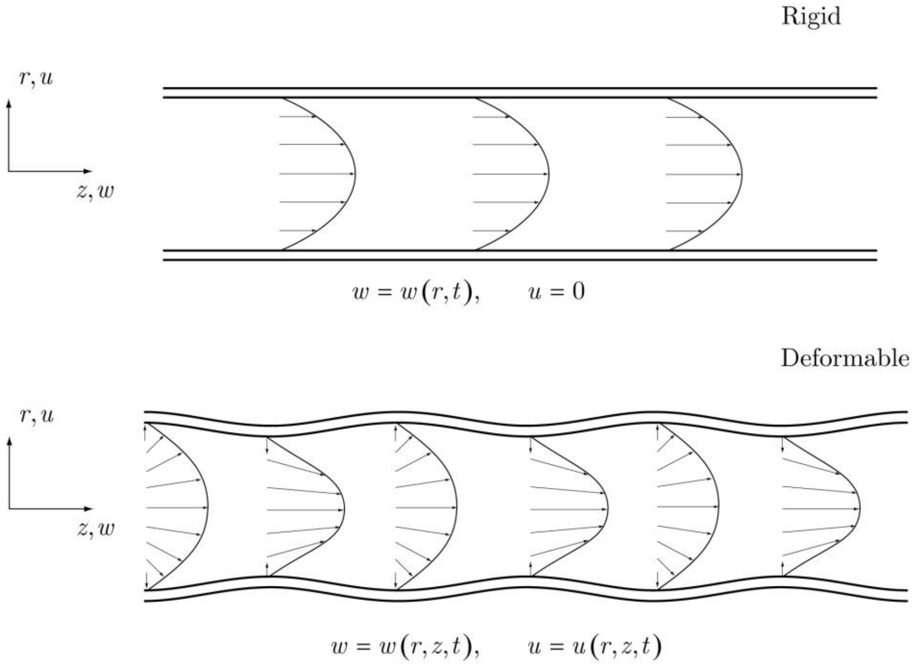

Figure 2-2: Qualitative differences in the velocity profiles of Womersley's rigid and deformable wall theories. The radial velocity component and the dependence of the profiles on the longitudinal coordinate *z* are both factors related to the presence of wave propagation in the mathematical model. Note: for illustrative purposes, the wavelength of the flow is shown as much shorter than it is in reality

Figure 2-2 illustrates this small but important difference between the velocity profiles present in the two theories. As a consequence of this, the solutions for the deformable theory are no longer fully developed, since as we will see in this section, the velocity profiles (both longitudinal and circumferential) will depend on the position along the vessel (z): this is again in agreement with the existence of waves propagating through the vessel at a *finite* speed. Therefore, the velocity profiles at a given time t will differ slightly at different positions along the vessel.

Considering the axisymmetry of the velocity field, the radial and longitudinal components of the Navier-Stokes equations of motion become:

$$\frac{\partial u}{\partial t} + \left(u\frac{\partial u}{\partial r} + w\frac{\partial u}{\partial z} \right) = -\frac{1}{\rho}\frac{\partial p}{\partial r} + \nu\left[\frac{\partial^2 u}{\partial r^2} + \frac{1}{r}\frac{\partial u}{\partial r} - \frac{u}{r^2} + \frac{\partial^2 u}{\partial z^2} \right] \tag{2.29}$$

$$\frac{\partial w}{\partial t} + \left(u\frac{\partial w}{\partial r} + w\frac{\partial w}{\partial z} \right) = -\frac{1}{\rho}\frac{\partial p}{\partial z} + \nu\left[\frac{\partial^2 w}{\partial r^2} + \frac{1}{r}\frac{\partial w}{\partial r} + \frac{\partial^2 w}{\partial z^2} \right] \tag{2.30}$$

whereas the continuity equation is simply:

$$\frac{\partial u}{\partial r} + \frac{u}{r} + \frac{\partial w}{\partial z} = 0 \tag{2.31}$$

The fluid equations of motion given by (2.29)-(2.31) can be simplified significantly if long-wave approximations are considered. These assumptions consist of mainly two points:

- The length of the propagating wave (L) is much larger than the vessel radius R.
- The wave speed c is much higher than the average longitudinal velocity $\bar{w}$ within the tube.

These two assumptions imply:

$$\frac{R}{L}, \frac{\bar{w}}{c} \ll 1 \tag{2.32}$$

To support these assumptions with physiologic data, let us consider the example of a common carotid artery. For this vessel, one can estimate the pulse velocity c using the Moen-Korteweg formula for wave speed c_0 for an inviscid fluid:

$$c_0 = \sqrt{\frac{Eh}{2\rho R}} \tag{2.33}$$

For a common carotid artery, with $E = 4 \cdot 10^6$ dyn/cm^2, h=0.03 cm, R=0.3 cm and $\rho = 1\,\text{g/cm}^3$, we have $c_0 = 450\,\text{cm/s}$. We can estimate the mean velocity $\bar{w}$ by dividing the flow rate (7.5 cm^3/s) by the cross sectional area of the artery. This produces a value for $\bar{w}$ of 25 cm/s. Therefore, the ratio of mean velocity to wave speed is

$$\frac{\bar{w}}{c_0} = \frac{25}{450} = 0.055 \ll 1 \tag{2.34}$$

Womersley considered trial functions compatible with the long-wave assumption for the flow variables u, w and p of the form:

$$u(r,z,t) = u_1(r)\, e^{i\omega\left(t-\frac{z}{c}\right)} \tag{2.35}$$

$$w(r,z,t) = w_1(r)\, e^{i\omega\left(t-\frac{z}{c}\right)} \tag{2.36}$$

$$p(r,z,t) = p_1(r)\, e^{i\omega\left(t-\frac{z}{c}\right)} \tag{2.37}$$

where ω is the frequency of oscillation of the pressure and velocity waves and c is the wave speed. Note that these expressions are a generalization of the 'infinite wave speed' for the rigid case given by equation (2.8).

Using the long-wave assumptions it is possible to estimate the scaling of the radial component of the velocity of the fluid u relative to the longitudinal component w. From (2.31) and (2.36), we have:

$$\frac{\partial u}{\partial r}+\frac{u}{r}+\frac{\partial w}{\partial z}\Rightarrow\frac{\bar{u}}{R}-\frac{\omega}{c}\bar{w}=0 \tag{2.38}$$

and we obtain:

$$\bar{u}=\frac{\omega R\bar{w}}{c} \tag{2.39}$$

It follows that the nonlinear terms in equations (2.29)-(2.30) are in general of order $1/c$ compared with the main linear terms and can therefore be neglected as a first approximation. Similarly, the terms containing second-order derivatives in z, can be neglected as well:

$$\frac{\partial^2 u}{\partial z^2}=-\frac{\omega^2}{c^2}u_1(r)e^{i\omega\left(t-\frac{z}{c}\right)}\ll\frac{\partial^2 u}{\partial r^2}=\frac{\partial^2 u_1(r)}{\partial r^2}e^{i\omega\left(t-\frac{z}{c}\right)} \tag{2.40}$$

$$\frac{\partial^2 w}{\partial z^2}=-\frac{\omega^2}{c^2}w_1(r)e^{i\omega\left(t-\frac{z}{c}\right)}\ll\frac{\partial^2 w}{\partial r^2}=\frac{\partial^2 w_1(r)}{\partial r^2}e^{i\omega\left(t-\frac{z}{c}\right)} \tag{2.41}$$

Considering all these simplifications, the momentum equations reduce to:

$$\frac{\partial u}{\partial t} = -\frac{1}{\rho}\frac{\partial p}{\partial r} + \nu\left[\frac{\partial^2 u}{\partial r^2} + \frac{1}{r}\frac{\partial u}{\partial r} - \frac{u}{r^2}\right] \tag{2.42}$$

$$\frac{\partial w}{\partial t} = -\frac{1}{\rho}\frac{\partial p}{\partial z} + \nu\left[\frac{\partial^2 w}{\partial r^2} + \frac{1}{r}\frac{\partial w}{\partial r}\right] \tag{2.43}$$

Now, substituting the expressions for u, w, and p given by equations (2.35)-(2.37) into the simplified momentum and continuity equations and canceling the exponential terms, we obtain:

$$i\omega u_1(r) = -\frac{1}{\rho}\frac{dp_1(r)}{dr} + \nu\left[\frac{d^2 u_1(r)}{dr^2} + \frac{1}{r}\frac{du_1(r)}{dr} - \frac{u_1(r)}{r^2}\right] \tag{2.44}$$

$$i\omega w_1(r) = \frac{i\omega}{c\rho} p_1(r) + \nu\left[\frac{d^2 w_1(r)}{dr^2} + \frac{1}{r}\frac{dw_1(r)}{dr}\right] \tag{2.45}$$

$$\frac{du_1(r)}{dr} + \frac{u_1(r)}{r} - \frac{i\omega}{c} w_1(r) = 0 \tag{2.46}$$

Rearranging the terms, we obtain the following system of *ordinary* differential equations:

$$\frac{d^2 u_1(r)}{dr^2} + \frac{1}{r}\frac{du_1(r)}{dr} - \left(\frac{1}{r^2} + \frac{i\rho\omega}{\mu}\right) u_1(r) = \frac{1}{\mu}\frac{dp_1(r)}{dr} \tag{2.47}$$

$$\frac{d^2 w_1(r)}{dr^2} + \frac{1}{r}\frac{dw_1(r)}{dr} - \frac{i\rho\omega}{\mu} w_1(r) = -\frac{i\omega}{\mu c} p_1(r) \tag{2.48}$$

$$\frac{du_1(r)}{dr} + \frac{u_1(r)}{r} - \frac{i\omega}{c} w_1(r) = 0 \tag{2.49}$$

Equations (2.47),(2.48) are (similar to what we obtained for the rigid wall theory) forms of Bessel equations with known solutions. To put equations (2.47)-(2.49) in standard form, we introduce the same change of variables defined by equations (2.10), (2.16) and (2.24):

$$\alpha = \sqrt{\frac{\rho\varpi}{\mu}}R, \qquad \Lambda = i^{\frac{3}{2}}\alpha, \qquad \eta = i^{\frac{3}{2}}\alpha\frac{r}{R} = \Lambda\frac{r}{R}$$

Using these parameters, we can rewrite the momentum and continuity equations as follows:

$$\frac{d^2u_1(\eta)}{d\eta^2} + \frac{1}{\eta}\frac{du_1(\eta)}{d\eta} + \left(1 - \frac{1}{\eta^2}\right)u_1(\eta) = \frac{i\Lambda}{\rho\varpi R}\frac{dp_1(\eta)}{d\eta} \tag{2.50}$$

$$\frac{d^2w_1(\eta)}{d\eta^2} + \frac{1}{\eta}\frac{dw_1(\eta)}{d\eta} + w_1(\eta) = \frac{1}{\rho c}p_1(\eta) \tag{2.51}$$

$$\frac{du_1(\eta)}{d\eta} + \frac{u_1(\eta)}{\eta} - \frac{i\varpi R}{c\Lambda}w_1(\eta) = 0 \tag{2.52}$$

The boundary conditions are zero velocity at the wall and finite velocity at the center of the vessel. However, because the vessel wall is in motion, the first of these boundary conditions presents a very important difficulty, given that the position of the vessel wall is unknown since it is part of the solution. This makes it impossible to obtain an analytical solution for the equations in their present form. We can circumvent this problem by applying the boundary condition at a fixed radius R, which is assumed to be the *average position* of the vessel wall. By doing this, the *approximate* boundary conditions become:

$$\begin{aligned} u_1\left(\alpha i^{\frac{3}{2}}\right) &= 0 \\ w_1\left(\alpha i^{\frac{3}{2}}\right) &= 0 \end{aligned} \tag{2.53}$$

$$\begin{aligned} \left|u_1(0)\right| &< \infty \\ \left|w_1(0)\right| &< \infty \end{aligned} \tag{2.54}$$

Solutions to the momentum equations that satisfy the continuity equation as well as the boundary conditions are:

$$u_1(\eta) = G\frac{\chi}{\Lambda}J_1(\eta) + H\frac{R\chi}{\mu\left(i\alpha^2 + \chi^2\right)}J_1\left(\frac{\chi}{\Lambda}\eta\right) \tag{2.55}$$

$$w_1(\eta) = GJ_0(\eta) + H\frac{R\chi}{\mu\left(i\alpha^2 + \chi^2\right)}J_0\left(\frac{\chi}{\Lambda}\eta\right) \tag{2.56}$$

$$p_1(\eta) = HJ_0\left(\frac{\chi}{R}\eta\right) \tag{2.57}$$

where G, H are arbitrary constants and

$$\chi = \frac{i\omega R}{c} \tag{2.58}$$

These solutions can be simplified by noting that:

$$\chi \sim \frac{R}{L} \ll 1 \tag{2.59}$$

so that

$$J_0\left(\chi \frac{r}{R}\right) \approx 1 \tag{2.60}$$

and

$$J_1\left(\chi \frac{r}{R}\right) \approx \frac{1}{2}\chi \frac{r}{R} \tag{2.61}$$

Using these simplifications, the solutions given by equations (2.55)-(2.57) become:

$$\boxed{\begin{gathered} u_1(r) = G\frac{i\omega R}{c\Lambda}J_1(\eta) + H\frac{i\omega r}{2\rho c^2} \\[2em] w_1(r) = GJ_0(\eta) + H\frac{1}{\rho c} \\[2em] p_1(r) = H \end{gathered}} \qquad \begin{gathered} (2.62) \\[2em] (2.63) \\[2em] (2.64) \end{gathered}$$

The constants G, H will be determined by matching the fluid and wall velocities at the interface ($r = R$). Note that equation (2.64) implies that the pressure is constant over the cross section of the vessel.

We now proceed to obtain the expressions that describe the motion of the vessel wall.

2.2.2.2 Equations of motion for the vessel wall

The vessel wall equations of motion are written in the context of *linear elasticity* and *thin-walled tube* theories. Cauchy's equation of motion is:

$$\rho^s \frac{\partial^2 \vec{u}}{\partial t^2} = \vec{B}_0 + \nabla \cdot \underset{\sim}{T} \tag{2.65}$$

where $\vec{u}$ is the displacement vector whose expression in cylindrical coordinates is:

$$\vec{u} = \begin{Bmatrix} \xi \\ 0 \\ \zeta \end{Bmatrix} \tag{2.66}$$

where ξ and ζ represent the wall displacement in the radial and longitudinal directions, respectively. Furthermore, the axisymmetry assumption makes the second component of the displacement vector identically zero. $\vec{B}_0$ represents a body force per unit volume which will be related to the pressure and shear forces coming from the fluid domain. Lastly, $\underset{\sim}{T}$ represents the Cauchy stress tensor for the vessel wall. The divergence of this tensor will be obtained by considering two different stress states separately and then combining them together using linear superposition:

- Internal pressurization with no axial strain
- Axial force with no internal pressure

Figure 2-3 lists the variables describing the two stress states mentioned above, where R and h represent the vessel radius and thickness, respectively. E, ρ^s and σ are the vessel wall's Young's modulus, density and Poisson's ratio, and ρ is the blood density.

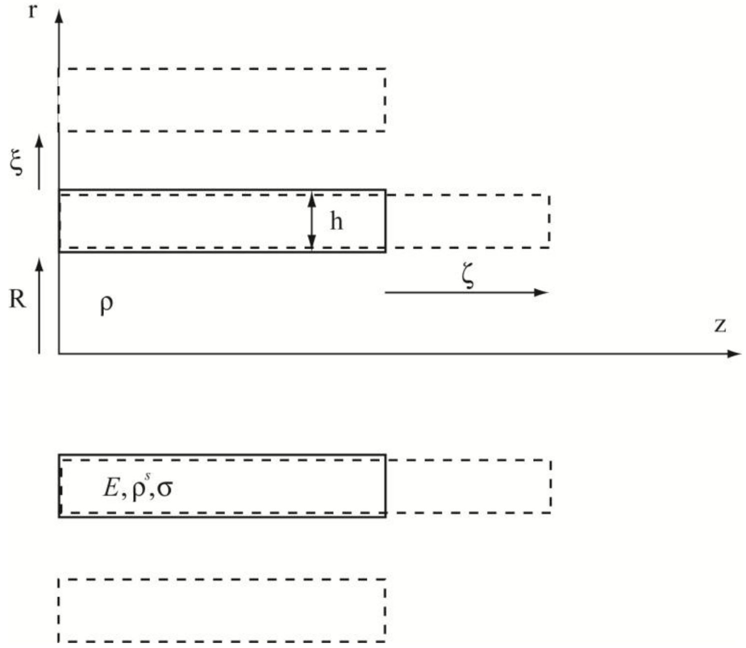

Figure 2-3: Scheme of the radial (ξ) and longitudinal (ζ) displacements of a thin-walled cylindrical segment.

The stresses and strains of the vessel wall are related by the linear elastic constitutive equation given by:

$$\underset{\sim}{\varepsilon} = \frac{1}{E}\left[(1+\sigma)\underset{\sim}{T} - \sigma T_{kk}\underset{\sim}{I}\right] \tag{2.67}$$

<u>Internal pressurization with no axial strain</u>

In this state, making use of thin-walled membrane theory, we assume that the radial stress T_{rr} is small compared to the circumferential or longitudinal stresses $T_{\theta\theta}$ and T_{zz}. Since there is no axial strain, we have:

$$\varepsilon_{zz} = \frac{1}{E}\left[(1+\sigma)T_{zz} - \sigma\left(T_{\theta\theta} + T_{zz}\right)\right] = 0 \quad \Rightarrow \quad T_{zz} = \sigma T_{\theta\theta} \tag{2.68}$$

The circumferential strain $\varepsilon_{\theta\theta}$ for a thin-walled tube is given by

$$\varepsilon_{\theta\theta} = \frac{2\pi(R+\xi) - 2\pi R}{2\pi R} = \frac{\xi}{R} \tag{2.69}$$

Using equation (2.67) to write this strain component as a function of the stresses, and using the result obtained in equation (2.68), we have:

$$\varepsilon_{\theta\theta} = \frac{1}{E}\left[(1+\sigma)T_{\theta\theta} - \sigma\left(T_{\theta\theta} + T_{zz}\right)\right] = \frac{\xi}{R} \quad \Rightarrow \quad T_{\theta\theta} = \frac{E}{\left(1-\sigma^2\right)}\frac{\xi}{R} \tag{2.70}$$

Therefore, if we define

$$B = \frac{E}{\left(1-\sigma^2\right)} \tag{2.71}$$

we obtain

$$T_{\theta\theta} = B\frac{\xi}{R} \quad , \quad T_{zz} = \sigma B\frac{\xi}{R} \tag{2.72}$$

Axial force with no internal pressure

In this state, we assume that the radial stress T_{rr} is small compared to the circumferential or longitudinal stresses $T_{\theta\theta}$ and T_{zz}. Since there is no circumferential strain, we have:

$$\varepsilon_{\theta\theta} = \frac{1}{E}\left[(1+\sigma)T_{\theta\theta} - \sigma\left(T_{\theta\theta} + T_{zz}\right)\right] = 0 \quad \Rightarrow \quad T_{\theta\theta} = \sigma T_{zz} \tag{2.73}$$

The longitudinal strain ε_{zz} is given by

$$\varepsilon_{zz} = \frac{\partial \zeta}{\partial z} = \frac{1}{E}\left[(1+\sigma)T_{zz} - \sigma\left(T_{\theta\theta} + T_{zz}\right)\right] \quad \Rightarrow \quad T_{zz} = \frac{E}{\left(1-\sigma^2\right)}\frac{\partial \zeta}{\partial z} \tag{2.74}$$

and therefore the stresses for this state can be written as:

$$T_{\theta\theta} = \sigma B \frac{\partial \zeta}{\partial z} \quad , \quad T_{zz} = B\frac{\partial \zeta}{\partial z} \tag{2.75}$$

By combining, using linear superposition, the states defined by equations (2.72) and (2.75) we obtain the following expressions for the stresses:

$$T_{\theta\theta} = B\left(\frac{\xi}{R} + \sigma\frac{\partial \zeta}{\partial z}\right) \quad , \quad T_{zz} = B\left(\sigma\frac{\xi}{R} + \frac{\partial \zeta}{\partial z}\right) \tag{2.76}$$

Using the thin wall assumption, where $r \approx R,\ h \ll R$, the divergence of the stress tensor for the combined state results in the following radial and longitudinal components:

$$\left(\nabla \cdot \underset{\sim}{T}\right)_r = \frac{T_{rr} - T_{\theta\theta}}{r} + \frac{\partial T_{rr}}{\partial r} + \frac{1}{r}\frac{\partial T_{\theta r}}{\partial \theta} + \frac{\partial T_{zr}}{\partial z} = -\left.\frac{T_{\theta\theta}}{r}\right|_{r=R} = -\frac{B}{R}\left(\frac{\xi}{R} + \sigma\frac{\partial \zeta}{\partial z}\right) \tag{2.77}$$

$$\left(\nabla \cdot \underset{\sim}{T}\right)_z = \frac{1}{r}\frac{\partial}{\partial r}\left(rT_{rz}\right) + \frac{1}{r}\frac{\partial T_{\theta z}}{\partial \theta} + \frac{\partial T_{zz}}{\partial z} = B\left(\frac{\sigma}{R}\frac{\partial \xi}{\partial z} + \frac{\partial^2 \zeta}{\partial z^2}\right) \tag{2.78}$$

Therefore, the radial and axial equations of motion for the vessel wall can be expressed as follows:

$$\frac{\partial^2 \xi}{\partial t^2} = \frac{B_r}{\rho^s} - \frac{B}{\rho^s}\left(\frac{\xi}{R^2} + \frac{\sigma}{R}\frac{\partial \zeta}{\partial z}\right) \tag{2.79}$$

$$\frac{\partial^2 \zeta}{\partial t^2} = \frac{B_z}{\rho^s} + \frac{B}{\rho^s}\left(\frac{\sigma}{R}\frac{\partial \xi}{\partial z} + \frac{\partial^2 \zeta}{\partial z^2}\right) \tag{2.80}$$

Using the thin wall assumptions, the radial and longitudinal components of the body force vector can be related to the pressure and shear stresses acting on the interface of the wall with the fluid domain as follows (see Figure 2-4):

$$B_r = \frac{p}{h} \quad , \quad B_z = -\frac{\tau}{h} \tag{2.81}$$

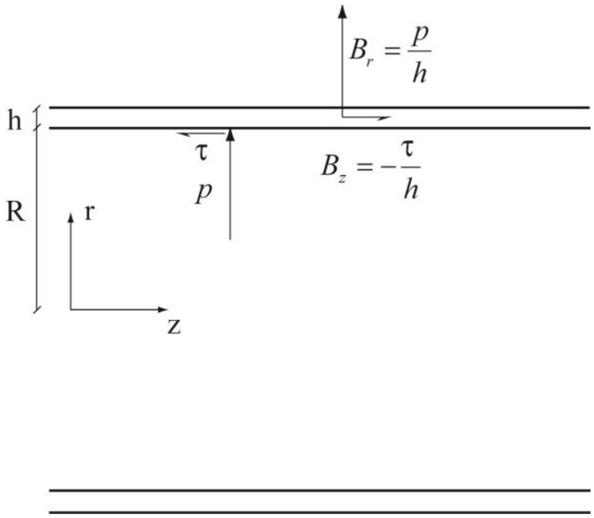

Figure 2-4: Radial and longitudinal components of the vessel wall body force vector $\vec{B}_0$.

The fluid vector $\vec{v}$ is of the form

$$\vec{v} = \begin{Bmatrix} v_r \\ 0 \\ v_z \end{Bmatrix} = \begin{Bmatrix} u \\ 0 \\ w \end{Bmatrix} \tag{2.82}$$

and the fluid shear τ can be written follows:

$$\tau = \tau_{rz} = \tau_{zr} = \rho\nu\left(\frac{\partial u}{\partial z} + \frac{\partial w}{\partial r}\right) \tag{2.83}$$

where ν represents the kinematic viscosity of the fluid. We can express the longitudinal body force B_z as follows:

$$B_z = -\frac{\tau}{h} = -\frac{\rho\nu}{h}\left(\frac{\partial u}{\partial z} + \frac{\partial w}{\partial r}\right)\bigg|_{r=R} \tag{2.84}$$

and therefore, the final expressions for the radial and axial equations of motion for the vessel wall can be expressed as follows:

$$\frac{\partial^2 \xi}{\partial t^2} = \frac{p}{\rho^s h} - \frac{B}{\rho^s}\left(\frac{\xi}{R^2} + \frac{\sigma}{R}\frac{\partial \zeta}{\partial z}\right) \tag{2.85}$$

$$\frac{\partial^2 \zeta}{\partial t^2} = -\frac{\rho}{\rho^s}\frac{\nu}{h}\left(\frac{\partial u}{\partial z} + \frac{\partial w}{\partial r}\right)\bigg|_{r=R} + \frac{B}{\rho^s}\left(\frac{\sigma}{R}\frac{\partial \xi}{\partial z} + \frac{\partial^2 \zeta}{\partial z^2}\right) \tag{2.86}$$

2.2.2.3 Coupling of the Fluid and Solid motions

The motion of the fluid is coupled with the motion of the vessel wall through the action of the pressure and shear stress on the wall as illustrated in Figure 2-4. Mathematically, the coupling is manifest by the presence of the pressure p and the velocities u and w in equations (2.85)-(2.86).

The pressure acting on the vessel wall, from equations (2.37) and (2.64) is:

$$p(r,z,t) = He^{i\omega\left(t-\frac{z}{c}\right)} \tag{2.87}$$

hence, the radial momentum equation for the wall becomes:

$$\boxed{\frac{\partial^2 \xi}{\partial t^2} = \frac{H}{\rho^s h} e^{i\omega\left(t-\frac{z}{c}\right)} - \frac{B}{\rho^s R}\left(\frac{\xi}{R} + \sigma \frac{\partial \zeta}{\partial z}\right)} \tag{2.88}$$

For the longitudinal equation (2.86), we can make use of the long-wave approximation and neglect the gradient of the radial velocity u with respect to the longitudinal coordinate z, since it is small compared to the gradient of the longitudinal velocity w with respect to r. By doing this, equation (2.86) reduces to:

$$\frac{\partial^2 \zeta}{\partial t^2} = -\frac{\rho}{\rho^s}\frac{\nu}{h}\left(\frac{\partial w}{\partial r}\right)\bigg|_{r=R} + \frac{B}{\rho^s}\left(\frac{\sigma}{R}\frac{\partial \xi}{\partial z} + \frac{\partial^2 \zeta}{\partial z^2}\right) \tag{2.89}$$

Using the result for the velocity w given by equations (2.36) and (2.56), we have that the gradient of w with respect to r is

$$\left(\frac{\partial w}{\partial r}\right)\bigg|_{r=R}=\frac{\partial}{\partial r}\left(GJ_0\left(\frac{\Lambda}{R}r\right)+H\frac{R\chi}{\mu\left(i\alpha^2+\chi^2\right)}J_0\left(\frac{\chi}{R}r\right)\right)\bigg|_{r=R}e^{i\omega\left(t-\frac{z}{c}\right)} \tag{2.90}$$

This expression, after using the approximations given by equations (2.59)-(2.61) becomes:

$$\left(\frac{\partial w}{\partial r}\right)\bigg|_{r=R}=\left(-\frac{G\Lambda J_1(\Lambda)}{R}+H\frac{\omega^2 R}{2\rho c^3}\right)e^{i\omega\left(t-\frac{z}{c}\right)} \tag{2.91}$$

and therefore the longitudinal momentum equation results in:

$$\boxed{\frac{\partial^2\zeta}{\partial t^2}=-\frac{1}{\rho^s h}\left(-\frac{\mu G\Lambda J_1(\Lambda)}{R}+\frac{\mu H\omega^2 R}{2\rho c^3}\right)e^{i\omega\left(t-\frac{z}{c}\right)}+\frac{B}{\rho^s}\left(\frac{\sigma}{R}\frac{\partial\xi}{\partial z}+\frac{\partial^2\zeta}{\partial z^2}\right)} \tag{2.92}$$

2.2.2.4 Matching the boundary conditions at the vessel wall

The vessel wall equations (2.88) and (2.92) contain two arbitrary constants (G and H) that are yet to be determined. These can be obtained by matching the motion of the fluid and the vessel wall at the interface, in both the radial and the longitudinal directions. We must impose the condition that the radial and longitudinal velocities of the fluid and wall at the interface are identical, since we are considering a Newtonian (and therefore viscous) fluid. As we saw in equations (2.53)-(2.54), these conditions are applied only approximately at the neutral position of the wall ($r=R$), since the position of the vessel wall forms part of the solution and therefore can not be obtained analytically. Furthermore, it is reasonable to assume the same functional form for the radial and longitudinal motion of the wall as the one used for the pressure and flow velocities. The frequencies of the oscillations of the wall motion will be the same as those present in the fluid (although this does not mean that the wall motion is necessarily in phase with the oscillations of the fluid). Considering this, we have:

Radial direction:

$$\xi(z,t) = Ke^{i\omega\left(t-\frac{z}{c}\right)} \tag{2.93}$$

$$\frac{\partial \xi}{\partial t} = u(R,z,t) \tag{2.94}$$

Longitudinal direction:

$$\zeta(z,t) = Ne^{i\omega\left(t-\frac{z}{c}\right)} \tag{2.95}$$

$$\frac{\partial \zeta}{\partial t} = w(R,z,t) \tag{2.96}$$

where K and N are two new constants to be determined.

Inserting the expressions of ξ and ζ into equations (2.88) and (2.92), and writing the explicit expression of the boundary conditions given by equations (2.94) and (2.96), we obtain (after simplifying the exponential terms):

Coupled equations of motion

Radial

$$-\omega^2 K = \frac{H}{\rho^s h} - \frac{B}{\rho^s R}\left(\frac{K}{R} + \sigma\left(\frac{-i\omega}{c}\right)N\right) \tag{2.97}$$

Longitudinal

$$-\omega^2 N = -\frac{1}{\rho^s h}\left(-\frac{\mu\Lambda J_1(\Lambda)}{R}G + \frac{\mu\omega^2 R}{2\rho c^3}H\right) + \frac{B}{\rho^s}\left(\frac{\sigma}{R}\left(\frac{-i\omega}{c}\right)K - \frac{\omega^2}{c^2}N\right) \tag{2.98}$$

Boundary conditions

Radial

$$i\omega K = \frac{i\omega R J_1(\Lambda)}{c\Lambda}G + \frac{i\omega R}{2\rho c^2}H \tag{2.99}$$

Longitudinal

$$i\omega N = J_0(\Lambda)G + \frac{1}{\rho c}H \tag{2.100}$$

Some simplifications are possible by noting that in equation (2.98), the term multiplied by H is small compared with the others, since it is divided by c^3. Furthermore, in equation (2.97), out of the two factors multiplying the constant K, the one on the left-hand-side of the equation is much smaller that the one on the right-hand-side. Considering these two simplifications, equations (2.97)-(2.100) can be rewritten as:

$$0 = \frac{H}{\rho^s h} - \frac{B}{\rho^s R}\left(\frac{K}{R} + \sigma\left(\frac{-i\omega}{c}\right)N\right) \tag{2.101}$$

$$-\omega^2 N = \frac{\mu \Lambda J_1\left(\Lambda\right)}{\rho^s h R} G + \frac{B}{\rho^s}\left(\frac{\sigma}{R}\left(\frac{-i\omega}{c}\right)K - \frac{\omega^2}{c^2} N\right) \tag{2.102}$$

$$i\omega K = \frac{i\omega R J_1\left(\Lambda\right)}{c\Lambda} G + \frac{i\omega R}{2\rho c^2} H \tag{2.103}$$

$$i\omega N = J_0\left(\Lambda\right) G + \frac{1}{\rho c} H \tag{2.104}$$

These 4 equations (2 coupled equations of motion and 2 boundary conditions), contain 4 undetermined arbitrary constants (G, H, K and N). However, these arbitrary constants are not the only unknowns in the system, since the wave speed c is still to be determined. In the next section we describe how the wave speed can be obtained from the system given by equations (2.101)-(2.104).

2.2.2.5 Obtaining the wave speed for the fluid-solid system

Equations (2.101)-(2.104) can be written in the form of the following system of linear equations:

$$\begin{bmatrix} 0 & a_{12} & a_{13} & a_{14} \\ a_{21} & 0 & a_{23} & a_{24} \\ a_{31} & a_{32} & a_{33} & 0 \\ a_{41} & a_{42} & 0 & a_{44} \end{bmatrix} \begin{Bmatrix} G \\ H \\ K \\ N \end{Bmatrix} = \begin{Bmatrix} 0 \\ 0 \\ 0 \\ 0 \end{Bmatrix} \tag{2.105}$$

where the matrix coefficients a_{ij} are given by the different terms of equations (2.101)-(2.104). Since the system defined in equation (2.105) is homogeneous, a nontrivial solution is obtained only if the determinant of the matrix is zero. Therefore, if we enforce that

$$\det\left(a_{ij}\right) = 0 \tag{2.106}$$

we obtain, after some algebra, the following quadratic equation:

$$\left[(g-1)\left(\sigma^2-1\right)\right]\upsilon^2 + \left[\frac{\rho^s h}{\rho R}(g-1) + \left(2\sigma - \frac{1}{2}\right)g - 2\right]\upsilon + \frac{2\rho^s h}{\rho R} + g = 0 \tag{2.107}$$

In this equation, υ is defined as

$$\upsilon = \frac{Bh}{\rho R c^2} \tag{2.108}$$

and g is

$$g = \frac{2J_1(\Lambda)}{\Lambda J_0(\Lambda)} \tag{2.109}$$

Solution to equation (2.107) will provide an expression for the wave speed c (after the parameter υ is obtained) as a function of the material properties of the fluid and wall, as well as the frequency of the flow. Equation (2.107) is usually referred to as the "frequency equation". If we recall the expression for the wave speed c_0 in inviscid flow given by equation (2.33):

$$c_0^2 = \frac{Eh}{2\rho R}$$

we can re-write equation (2.108) as follows:

$$\upsilon = \frac{2Eh}{2\left(1-\sigma^2\right)\rho R c^2} = \frac{2}{\left(1-\sigma^2\right)}\frac{c_0^2}{c^2} \tag{2.110}$$

and therefore, the final expression for the wave speed c as a function of the parameter υ is:

$$c = \sqrt{\frac{2}{\left(1-\sigma^2\right)\upsilon}}c_0 \tag{2.111}$$

Equation (2.107) has two solutions for the parameter υ, and consequently for the wave speed *c*. Only one of them has physical relevance for this problem: the one whose modulus is smaller than the inviscid wave speed given by equation (2.33) [51], since waves travel slower in more viscous fluids. Furthermore, *c* is a complex number and therefore (unlike c_0) is not a true speed in the physical sense. If we decompose the complex wave speed c into its real and imaginary parts as follows:

$$\frac{1}{c} = \frac{1}{c_R} + i\frac{1}{c_I} \tag{2.112}$$

we can study the consequences of its complex nature in the velocity and pressure solutions, by recalling the exponential expression governing the phase variation:

$$e^{i\omega\left(t-\frac{z}{c}\right)}=e^{i\omega\left(t-\frac{z}{c_R}-i\frac{z}{c_I}\right)}=e^{\frac{\omega z}{c_I}}e^{i\omega\left(t-\frac{z}{c_R}\right)}$$

We can observe that the imaginary part of the wave speed c_I is effectively changing the amplitude of the pressure and velocity waves. This effect is known as *attenuation*, and it is not present in the inviscid case. On the other hand, the real part of the wave speed c_R will effectively change the phase of the wave, adopting different values for different frequencies. This effect is known as *dispersion*.

2.2.2.6 Arbitrary constants of the flow and vessel wall solutions

The matrix defined in equation (2.105) is a rank-three matrix, and therefore once the wave equation c is obtained, we must specify the value for one of the four arbitrary constants (G, H, K and N). By looking at the flow field solutions given by equations (2.62)-(2.64), H is the obvious choice for this constant. This constant will represent the prescribed amplitude of the input oscillatory pressure (at $z = 0$). We can then obtain the expressions for the rest of the constants (G, K and N) once H is fixed. Therefore, we have:

$$p(r,z,t)=p_1(r)e^{i\omega\left(t-\frac{z}{c}\right)}=He^{i\omega\left(t-\frac{z}{c}\right)} \tag{2.113}$$

Using the equations defining the system (2.105) to eliminate H, we get, after some algebra:

$$G = \frac{1}{\rho c J_0(\Lambda)} \left[\frac{2 + \upsilon(2\sigma - 1)}{\upsilon(g - 2\sigma)} \right] H \tag{2.114}$$

$$N = \frac{i}{\rho c \omega} \left[\frac{2 - \upsilon(1 - g)}{\upsilon(2\sigma - g)} \right] H \tag{2.115}$$

$$K = \frac{R}{\rho c^2} \left[\frac{g + \sigma\upsilon(g - 1)}{\upsilon(g - 2\sigma)} \right] H \tag{2.116}$$

We are now ready to write down the final expressions for the velocity components of the flow.

2.2.2.7 Final expressions for the flow velocities

The longitudinal flow velocity is now fully determined, using equations (2.36), (2.63) and (2.114):

$$w(r,z,t) = \frac{H}{\rho c} \left[1 - M \frac{J_0\left(\frac{\Lambda r}{R}\right)}{J_0(\Lambda)} \right] e^{i\omega\left(t - \frac{z}{c}\right)} \tag{2.117}$$

where M is a constant usually referred to as the “elasticity factor”, whose expression is given by:

$$M = \frac{2 + \upsilon(2\sigma - 1)}{\upsilon(2\sigma - g)} \tag{2.118}$$

It is interesting to compare equation (2.117) with its rigid wall counterpart. As we will see, they are very similar, except for the presence of the elasticity factor. To make a valid comparison, we must take some care in writing equation (2.117), since there H represents the prescribed input oscillatory pressure, whereas in the rigid case A (or k_s) represents the prescribed oscillatory pressure *gradient*. We can therefore calculate the oscillatory pressure gradient for the deformable case using equation (2.113) and set it equal to the pressure gradient of the rigid wall case (A or k_s). By doing this, we have:

$$p(r,z,t) = He^{i\omega\left(t-\frac{z}{c}\right)} \Rightarrow \frac{\partial p}{\partial z} = -\frac{i\omega}{c} He^{i\omega\left(t-\frac{z}{c}\right)} \tag{2.119}$$

Therefore, we can set (recall equation (2.7)):

$$-\frac{i\omega}{c} H = A \quad \Rightarrow \quad H = \frac{ic}{\omega} A \tag{2.120}$$

If we now insert this definition for the parameter H as a function of the pressure gradient of the rigid case into equation (2.117), and normalize it using the maximum centerline velocity of the Poiseuille solution of the same pressure gradient (see equation (2.27)), we obtain the deformable wall counterpart of the rigid wall longitudinal velocity given by equation (2.28):

$$\hat{w}(r,z,t) = \frac{-4}{\Lambda^2}\left[1 - M\frac{J_0\left(\frac{\Lambda r}{R}\right)}{J_0(\Lambda)}\right] e^{i\omega\left(t-\frac{z}{c}\right)} \tag{2.121}$$

As we stated previously, the difference between equations (2.121) and (2.28) reduces to the elasticity factor M. However, since this factor is a complex number whose real and imaginary parts depend on the frequency of the flow, the impact on the differences between the rigid and deformable wall solutions is not obvious.

In the interpretation of equations (2.117) and (2.121), it is important to realize that the oscillatory flow in a deformable vessel has two oscillations: one in time, and one in space. Both oscillations are related to the same frequency ω and therefore the same period $T = 2\pi / \omega$. During this period T, the input oscillatory pressure completes one cycle in time, whereas the pressure within the vessel completes one cycle in space: this is the essence of wave propagation. The spatial wave has a length of $L = cT$, and points in the vessel separated a distance L will have in-phase pressures and velocities for each time t.

The differences between the rigid and deformable wall solutions for the longitudinal velocity profiles will be especially significant if the vessel considered is long enough for the spatial wave to be complete. If the length l of the vessel is much smaller than the wavelength L of the flow and velocity waves, then the differences between the rigid and deformable wall solutions for the axial velocity are quite small, because the spatial wave does not occur in full. This is indeed the case in most vessels in the cardiovascular system, whose length l is much shorter than the characteristic length of the waves associated with the physiologic frequencies.

We can now obtain the expression for the radial velocity of the vessel using equations (2.35), (2.62) and (2.114). Using these equations, we obtain:

$$u(r,z,t) = \frac{Hi\omega R}{2\rho c^2}\left[\frac{r}{R} - M\frac{2J_1\left(\frac{\Lambda r}{R}\right)}{\Lambda J_0(\Lambda)}\right]e^{i\omega\left(t-\frac{z}{c}\right)} \tag{2.122}$$

Now, if we normalize this expression using the pressure parameter as previously defined by equation (2.120) and the maximum centerline velocity of the Poiseuille solution, we get:

$$\hat{u}(r,z,t) = \frac{u(r,z,t)}{w_s(r=0)} = \frac{2\mu}{\rho c R}\left[\frac{r}{R} - M\frac{2J_1\left(\frac{\Lambda r}{R}\right)}{\Lambda J_0(\Lambda)}\right]e^{i\omega\left(t-\frac{z}{c}\right)} \tag{2.123}$$

or, equivalently

$$\hat{u}(r,z,t) = \frac{2R\omega}{i\Lambda^2 c}\left[\frac{r}{R} - M\frac{2J_1\left(\frac{\Lambda r}{R}\right)}{\Lambda J_0(\Lambda)}\right]e^{i\omega\left(t-\frac{z}{c}\right)} \tag{2.124}$$

If we evaluate this expression at the vessel wall ($r = R$), we have:

$$\hat{u}(R,z,t) = \frac{2R\omega}{i\Lambda^2 c}\left[1 - Mg\right]e^{i\omega\left(t-\frac{z}{c}\right)} \tag{2.125}$$

where g is given by equation (2.109). Equation (2.125) is of particular interest since it provides the radial velocity of the vessel wall.

To finish the present chapter, we summarize all the steps involved in obtaining the analytical solutions for pulsatile flow and pressure in a deformable cylindrical vessel.

1. Given the input pressure gradient $\partial p / \partial z = k(t)$, we decompose it into its *steady* part k_s and *oscillatory* part $k_\phi(t)$ (see Figure 2-5).

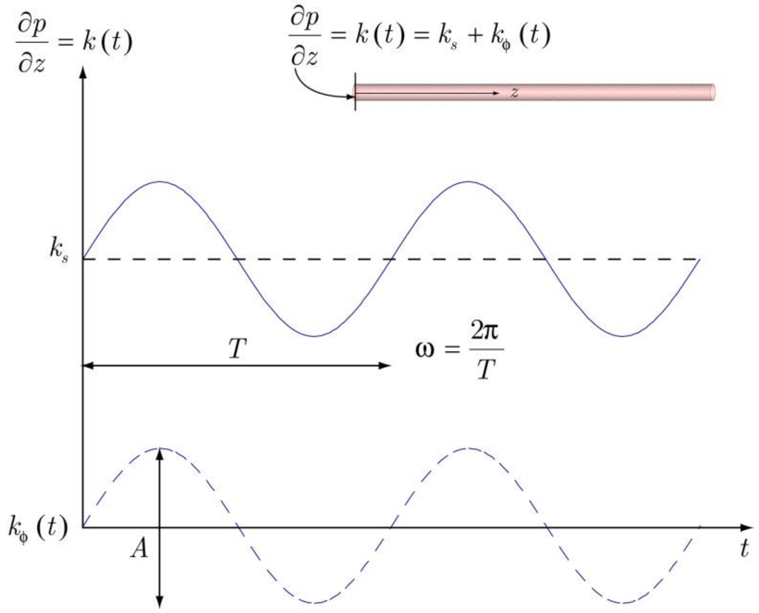

Figure 2-5: Decomposition of the input pressure gradient into its steady and oscillatory components.

2. The steady part of the pressure gradient defines the steady component of the flow, given by Poiseulle's solution

$$w_s(r) = \frac{k_s}{4\mu}\left(r^2 - R^2\right) \tag{2.126}$$

3. For the oscillatory part of the pressure gradient, we do a Fourier decomposition of the wave, and for each mode we obtain its frequency ω and amplitude A (see Figure 2-5).

4. We then proceed to obtain the oscillatory components of the pressure and velocity fields. Since Womersley's deformable wall solution is obtained in terms of an input oscillatory pressure (not an input oscillatory pressure *gradient*), we relate the amplitude of the input oscillatory pressure gradient A (see Figure 2-5 and equations (2.7), (2.120)) with the parameter H defining the amplitude of the input oscillatory pressure:

$$H = \frac{ic}{\omega} A \tag{2.127}$$

5. For each frequency ω and amplitude of the input oscillatory pressure H, we solve the frequency equation to obtain the wave speed c associated with the frequency ω :

$$\begin{gathered}
\left[(g-1)\left(\sigma^2-1\right)\right]\upsilon^2 + \left[\frac{\rho^s h}{\rho R}(g-1) + \left(2\sigma - \frac{1}{2}\right)g - 2\right]\upsilon + \frac{2\rho^s h}{\rho R} + g = 0 \\
\Downarrow \\
\text{get } \upsilon \\
\Downarrow \\
c = \sqrt{\frac{2}{\left(1-\sigma^2\right)\upsilon}}c_0
\end{gathered} \tag{2.128}$$

6. Once c, ω and H are known, the expressions for the oscillatory pressure and velocity components are given by the **real part** of:

$$p_\phi(r,z,t) = He^{i\omega\left(t-\frac{z}{c}\right)} \tag{2.129}$$

$$w_\phi(r,z,t) = \frac{H}{\rho c}\left[1 - M\frac{J_0\left(\frac{\Lambda r}{R}\right)}{J_0(\Lambda)}\right]e^{i\omega\left(t-\frac{z}{c}\right)} \tag{2.130}$$

$$u_\phi(r,z,t) = \frac{Hi\omega R}{2\rho c^2}\left[\frac{r}{R} - M\frac{2J_1\left(\frac{\Lambda r}{R}\right)}{\Lambda J_0(\Lambda)}\right]e^{i\omega\left(t-\frac{z}{c}\right)} \tag{2.131}$$

7. The final expressions for the velocity and pressure field are obtained via superposition of the steady and oscillatory components:

$$p(r,z,t) = He^{i\omega\left(t-\frac{z}{c}\right)} + p_0 + k_s(z-z_0) \tag{2.132}$$

$$w(r,z,t) = \frac{k_s}{4\mu}\left(r^2 - R^2\right) + \frac{H}{\rho c}\left[1 - M\frac{J_0\left(\frac{\Lambda r}{R}\right)}{J_0(\Lambda)}\right]e^{i\omega\left(t-\frac{z}{c}\right)} \tag{2.133}$$

$$u(r,z,t) = \frac{Hi\omega R}{2\rho c^2}\left[\frac{r}{R} - M\frac{2J_1\left(\frac{\Lambda r}{R}\right)}{\Lambda J_0(\Lambda)}\right]e^{i\omega\left(t-\frac{z}{c}\right)} \tag{2.134}$$

2.3 Coupled Fluid-Solid Interaction Equations (3D)

Womersley's theory is inapplicable in patient-specific models of the vasculature, due to the arbitrariness of the geometry, which usually features bifurcations, tapering of vessels, etc. For studying the coupled problem of blood flow and vessel wall deformation in such models, one must resort to numerical formulations to solve the partial differential equations describing the three-dimensional flow. When the deformation of the domain is small, the vessel walls are assumed to be rigid and therefore the fluid equations can be written in the *Eulerian* formulation and solved accordingly. This has been the strategy usually adopted to compute blood flow in large, patient-specific models [6,16,17,18,19,20]. The rigid wall approximation is made in large part because of the difficulty of solving the coupled blood flow / vessel deformation problem. However, this observation was made for arteries where wall motion is small and may not be valid for arteries where deformations are larger (e.g., the thoracic aorta). Furthermore, as we explained in the introduction, the assumption of rigid vessel walls precludes wave propagation phenomena, fundamentally changes the character of the resultant solutions, and results in difficulties in coupling three-dimensional domains with domains described using one-dimensional wave propagation methods [23,24].

When the vessel wall deformation is considered, the fluid domain is no longer constant. In this case, an *Eulerian* description for the blood flow equations is not appropriate and instead a mixed *Lagrangian-Eulerian* formulation is commonly used, where the concept of *grid velocity* is introduced. The grid velocity is usually defined in such a way that that it matches the physical velocity of the fluid-solid interface, and then in the rest of the domain it varies according to an arbitrary mapping $\mathbf{\Phi}$ between the *current* and some *reference configuration* for the fluid-solid system, (see Figure 2-6). Writing the fluid equations in this *Lagrangian-Eulerian* frame, together with the definition of this *arbitrary* mapping are the key features of a widely used formulation to solve flows in moving domains: the *Arbitrary Lagrangian-Eulerian* (ALE) formulation. Excellent work on this formulation can be found in [33,34,39,52] and [38]. In this Section, we briefly describe the basic "ingredients" of this formulation, which involve the solution of three coupled problems:

1. The blood flow problem on a moving grid (ALE formulation).
2. The wall deformation problem (Lagrangian formulation).
3. The time evolution of the grid of the domains (through the arbitrary mapping $\mathbf{\Phi}$).

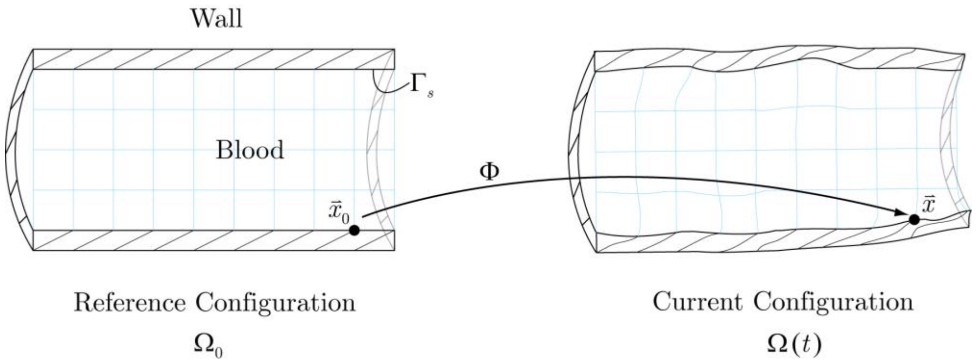

Figure 2-6: Reference and Current configurations of the blood and vessel wall domains and the mapping Φ that relates them.

The mapping Φ is a continuous function that relates the position of a point $\vec{x}_0$ in the Reference Configuration $\Omega_0 = \Omega_0^f \bigcup \Omega_0^s$ with its position $\vec{x}$ in the Current configuration $\Omega(t) = \Omega^f(t) \bigcup \Omega^s(t)$ for all times $t \in I$:

$$\begin{gathered} \Phi : \Omega_0 \times I \to \Omega(t) \\ \left(\vec{x}_0, t\right) \to \vec{x} = \Phi\left(\vec{x}_0, t\right) \end{gathered} \tag{2.135}$$

The grid velocity $\vec{v}_G$ is defined such that is equal to the real velocity of the structure. The fluid domain grid velocity is usually determined through a lifting [53] of the velocity of the structure at the interface Γ_s into the interior of the fluid domain $\Omega^s(t)$.

The flow mass and momentum balance equations in the ALE formulation are:

$$\left.\frac{\partial \rho_0}{\partial t}\right|_{\vec{x}_0} + \nabla_0 \cdot \left(\rho_0 \left(\vec{v} - \vec{v}_G\right) \underset{\sim}{F}^{-T}\right) = 0, \qquad \text{in } \Omega_0^f \tag{2.136}$$

$$\left.\frac{\partial \rho_0 \vec{v}}{\partial t}\right|_{\vec{x}_0} + \nabla_0 \cdot \left(\rho_0 \vec{v} \otimes \left(\vec{v} - \vec{v}_G\right) \underset{\sim}{F}^{-T}\right) = \nabla_0 \cdot \left(J \underset{\sim}{\sigma} \cdot \underset{\sim}{F}^{-T}\right) + \vec{f}, \quad \text{in } \Omega_0^f \tag{2.137}$$

The equations are written in the fixed Reference configuration Ω_0^f, but include the grid velocity $\vec{v}_G$ and the deformation gradient $\underset{\sim}{F}$ defined as:

$$\underset{\sim}{F} = \frac{\partial \vec{x}}{\partial \vec{x}_0} \tag{2.138}$$

with $J = \det \underset{\sim}{F}$ and $\rho_0 = J\rho$.

The wall deformation problem in Lagrangian formulation can be written as

$$\frac{\partial}{\partial t}\rho_0^s = 0, \qquad \text{in } \Omega_0^s \tag{2.139}$$

$$\rho_0^s \frac{D\vec{v}}{Dt} = \nabla_0 \cdot \left(J \underset{\sim}{\sigma}^s \underset{\sim}{F}^{-T} \right) + \vec{f}^s \qquad \text{in } \Omega_0^s \tag{2.140}$$

The coupling of the fluid and solid problems at the interface Γ_s is done via two *Transmission* or *Interface Conditions*:

- Kinematic condition (continuity of velocities):

$$\vec{v}^{fluid} = \vec{v}^{solid}, \qquad \text{on } \Gamma_s \tag{2.141}$$

- Dynamic condition or action-reaction principle (continuity of tractions):

$$\vec{t}^{fluid} = \vec{t}^{solid}, \qquad \text{on } \Gamma_s \tag{2.142}$$

Obtaining the solution of the coupled problems and the evolution of the computational grid can be computationally intensive, especially if the deformations are large. Significant effort has resulted in faster iterative algorithms for the solution of these problems [38,42,54]. However, as a consequence of the computational expense of this method, the cardiovascular models solved using the ALE formulation have usually considered reduced and significantly simplified geometries [21,22,40,41,55,56].

The main goal of this thesis was to develop a new formulation to circumvent the problems related to the computational expense of the ALE formulation and therefore enable modeling of blood flow and vessel wall deformation in large scale patient-specific models of the vasculature in a clinically-relevant time frame. The formulation proposed in this thesis represents a simpler approach to the coupled problem of blood flow and vessel wall deformation than the ALE approach, but offers substantial advantages over rigid wall formulations commonly used for large patient-specific cardiovascular simulations. In the following chapter, we present the details of this new mathematical formulation.

Chapter 3

Chapter 3. Coupled Momentum Method for Fluid-Solid Interaction (CMM-FSI)

In this chapter, we present the mathematical formulation of the Coupled-Momentum Method and discuss issues related to the fluid-solid coupling, membrane formulation, time integration algorithm, and boundary and initial conditions. We also describe how to obtain the wall shear stress field using a variationally consistent approach.

3.1 Introduction

In this chapter we present a new formulation for modeling blood flow in deformable arteries called the Coupled Momentum Method for Fluid-Solid Interaction problems (CMM-FSI). This formulation starts from a conventional stabilized finite element formulation for the Navier-Stokes equations in a rigid domain and modifies it in such a way that the deformability of the wall domain surrounding the fluid is taken into account. The main features of this formulation can be summarized as follows:

1. The z*ero-velocity condition (Dirichlet) is removed* from the lateral surface of the fluid domain and replaced with a traction condition (Neumann) which is to be determined using the elastodynamics equations that describe the motion of the vessel wall.

2. Using a *thin wall approximation*, this unknown interface traction can be related to a body force for the vessel wall. This approach is analogous to that used by J.R. Womersley in his derivation of an analytical solution of pulsatile flow in a deformable cylindrical domain [57].

3. This body force can be related through the elastodynamics equations with the mass and stiffness terms of the vessel wall.

4. A *membrane formulation* is used to describe the mass and stiffness terms of the solid. This is justified because the cardiac pulse has a long wavelength (meters) compared with the diameters of arteries (centimeters or millimeters). Consequently, arteries tend to respond primarily in membrane mode rather than in bending mode. The advantage of this approach is that no additional degrees-of-freedom beyond the membrane wall velocities are needed.

5. A *strong coupling* approach is used whereby the degrees-of-freedom of the vessel wall and the fluid boundary are the same. This results in a monolithic algorithm where the solid momentum contributions are embedded into the fluid equations using the same degrees-of-freedom. The membrane displacements are obtained by consistent time integration of the fluid velocities and accelerations.

6. A *linearized kinematics* approach is adopted for the coupled problem. This enables a representation of the solid equations using the same Eulerian frame as in the fluid equations. Furthermore, the fluid mesh is kept fixed and therefore the computational time compared to ALE formulations is greatly reduced. As a result of this, we have a fluid-solid interface mesh that is kept fixed, but where the nodes will have nonzero velocities in general. This is a feature also present in transpiration condition formulations [47,48] but in the work presented here is obtained by adopting a linearized kinematics formulation for the solid domain following the approach described by J.R. Womersley [36].

7. A linear membrane *enhanced with transverse shear modes* is used due to the inherent lack of stability of the linear membrane under transverse loading. These additional stresses provide stiffness to the structure without using additional degrees-of-freedom other than the membrane nodal displacements.

With this approach, the effects of the vessel wall motion are embedded in the weak form representing the blood flow resulting in a single weak form for the combined problem. As a result of this, only minimal changes in the stiffness matrices and residuals of the rigid wall finite element model are required to incorporate the effects of the wall motion. The approach delineated here results in a tractable, efficient and robust procedure to simulate fluid-structure interactions in three-dimensional models of the cardiovascular system. The computational effort is comparable to that of rigid wall formulations while at the same time it respects the essential physics and enables realistic simulation of wave-propagation phenomena in the arterial system as well as a linearized description of wall deformation. While the method as presented here (i.e., formulated in fixed grids) will not produce results equivalent to those given by ALE formulations in problems where the deformations are large (10% and above), the algorithmic simplicity will enable the solution of larger cardiovascular models in a clinically-relevant time frame, as is often required in surgical planning applications. The method accomplishes all this avoiding the above-mentioned drawbacks of the ALE formulation.

3.2 Governing Equations (Strong and Weak Forms)

3.2.1 Blood Flow Equations (Strong Form)

Blood flow in the large vessels of the cardiovascular system can be approximated as the flow of an incompressible Newtonian fluid in a domain $\Omega \in \Re^{n_{sd}}$ (see Figure 3-1), where n_{sd} is the number of spatial dimensions. The boundary Γ of this domain Ω can be conceptually divided in three different partitions such that $\Gamma = \partial\Omega = \Gamma_g \bigcup \Gamma_h \bigcup \Gamma_s$; $\Gamma_g \bigcap \Gamma_h \bigcap \Gamma_s = \varnothing$.

The strong form of the continuity and momentum balance equations governing such flow, written in advective form ([16,58,59]) is as follows:

Given $\vec{f}{:}\Omega \times (0,T) \to \Re^{n_{sd}}$, $\vec{g}{:}\Gamma_g \times (0,T) \to \Re^{n_{sd}}$, $\vec{h}{:}\Gamma_h \times (0,T) \to \Re^{n_{sd}}$, $\vec{v}^0{:}\Omega \to \Re^{n_{sd}}$; find $\vec{v}(\vec{x},t)$ and $p(\vec{x},t)$ $\forall \vec{x} \in \Omega$, $\forall t \in [0,T]$ such that

$$\nabla \cdot \vec{v} = 0\,, \quad (\vec{x},t) \in \Omega \times (0,T) \tag{3.1}$$

$$\rho\vec{v}_{,t} + \rho\vec{v} \cdot \nabla\vec{v} = -\nabla p + \nabla \cdot \underset{\sim}{\tau} + \vec{f}\,, \quad (\vec{x},t) \in \Omega \times (0,T) \tag{3.2}$$

$$\vec{v} = \vec{g}\,, \quad (\vec{x},t) \in \Gamma_g \times (0,T) \tag{3.3}$$

$$\vec{t}_{\vec{n}} = \underset{\sim}{\sigma}\vec{n} = \left[-p\underset{\sim}{I} + \underset{\sim}{\tau}\right]\vec{n} = \vec{h}\,, \quad (\vec{x},t) \in \Gamma_h \times (0,T) \tag{3.4}$$

$$\vec{t}_{\vec{n}} = \vec{t}^{\,f}\,, \quad (\vec{x},t) \in \Gamma_s \times (0,T) \tag{3.5}$$

$$\vec{v}(\vec{x},0) = \vec{v}^0(\vec{x})\,, \quad \vec{x} \in \Omega \tag{3.6}$$

Here, $\bar{v}$ represents the blood velocity, p is the pressure, ρ is the blood density, $\bar{f}$ is the prescribed body force per unit volume and $\underset{\sim}{\tau}$ is the viscous stress tensor defined by

$$\underset{\sim}{\tau} = \mu\left(\nabla\bar{v} + (\nabla\bar{v})^{T}\right) \tag{3.7}$$

where μ is the dynamic viscosity.

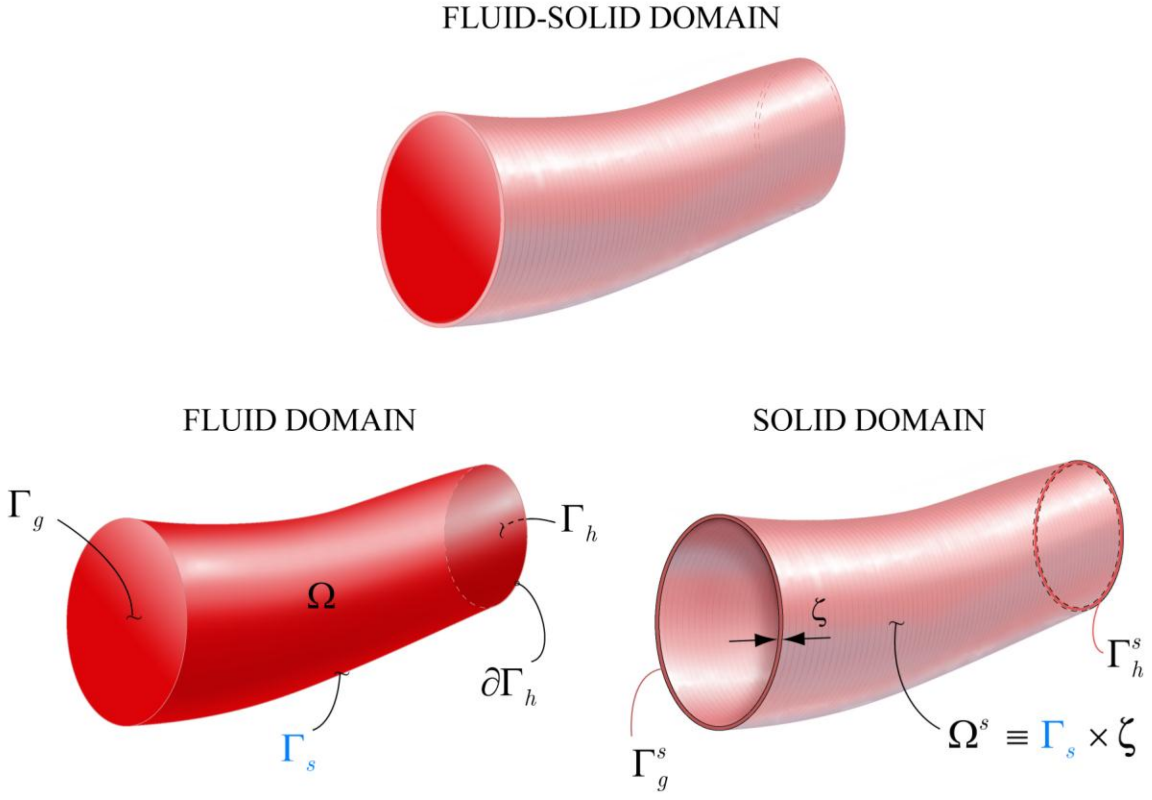

Figure 3-1: Schematic representation of the Fluid and Solid Domains and their boundaries.

The initial velocity field $\bar{v}^0$ is assumed to be divergence-free. Γ_g represents the fraction of the boundary where the given velocity field represented by $\vec{g}$ is prescribed. Γ_h and Γ_s represent Neumann boundaries where the tractions $\vec{h}$ and

$\vec{t}^{\,f}$ are prescribed. Γ_h refers typically to an outflow boundary, and the traction $\vec{h}$ can be calculated using a constant traction, resistance or impedance boundary condition [24]. The lateral boundary of the fluid domain is depicted by Γ_s. This part represents the interface with the vessel wall. While a no-slip boundary condition would be prescribed on Γ_s in the case of a rigid wall approximation, this constraint is removed here to enable non-zero wall velocity and replaced by a traction $\vec{t}^{\,f}$. This traction is due to the interaction of blood and the vessel wall. At this point $\vec{t}^{\,f}$ is unknown but it will ultimately be related to the stiffness and mass of the vessel wall using the elastodynamics equations of the solid.

3.2.2 Blood Flow Equations (Weak Form)

We define the trial solution and weighting function spaces for the semi-discrete formulation of the problem described by (3.1)-(3.7) as

$$\vec{\mathcal{S}}_h^k = \left\{ \vec{v} \,|\, \vec{v}(\cdot,t) \in H^1(\Omega)^{n_{sd}}, t \in [0,T], \vec{v}|_{\vec{x}\in\bar{\Omega}_e} \in P_k(\bar{\Omega}_e)^{n_{sd}}, \vec{v}(\cdot,t) = \hat{\vec{g}} \text{ on } \Gamma_g \right\} \quad (3.8)$$

$$\vec{\mathcal{W}}_h^k = \left\{ \vec{w} \,|\, \vec{w}(\cdot,t) \in H^1(\Omega)^{n_{sd}}, t \in [0,T], \vec{w}|_{\vec{x}\in\bar{\Omega}_e} \in P_k(\bar{\Omega}_e)^{n_{sd}}, \vec{w}(\cdot,t) = \vec{0} \text{ on } \Gamma_g \right\} \quad (3.9)$$

$$\mathcal{P}_h^k = \left\{ p \,|\, p(\cdot,t) \in H^1(\Omega), t \in [0,T], p|_{\vec{x}\in\bar{\Omega}_e} \in P_k(\bar{\Omega}_e) \right\} \quad (3.10)$$

where $\bar{\Omega} \subset \Re^{n_{sd}}$ represents the closure of the spatial domain $(\Omega \cup \Gamma)$ in $n_{sd} = 3$ dimensions. In addition, $H^1(\Omega)$ represents the usual Sobolev space of functions with square-integrable values and first derivatives in Ω, which is discretized into

n_{el} finite elements, $\bar{\Omega}_e$. $P_k(\bar{\Omega}_e)$ is the local polynomial approximation space in $\bar{\Omega}_e$ and $\hat{\vec{g}}$ represents an approximation to the prescribed Dirichlet boundary condition in the finite element basis. It is important to note that, because stabilized methods are used, the local approximation space $P_k\left(\bar{\Omega}_e\right)$ is the same for both the velocity and pressure variables [60].

The stabilized formulation used in the present work is based on the methods proposed by Hughes and colleagues and is described in Taylor *et al.* [16] and Whiting and Jansen [58]. The diffusive term, pressure term and continuity equation are all integrated by parts. Considering the spaces defined above, the semi-discrete Galerkin finite element formulation results in the following weak form of (3.1)-(3.7):

Find $\vec{v} \in \vec{\mathcal{S}}_h^k$ and $p \in \mathcal{P}_h^k$ such that

$$\begin{aligned} B_G(\vec{w},q;\vec{v},p) = &\int_\Omega \left\{\vec{w}\cdot\left(\rho\vec{v}_{,t} + \rho\vec{v}\cdot\nabla\vec{v} - \vec{f}\right) + \nabla\vec{w}:\left(-p\underset{\sim}{I} + \underset{\sim}{\tau}\right) - \nabla q\cdot\vec{v}\right\} d\vec{x} \\ &+\int_{\Gamma_h}\left\{-\vec{w}\cdot\vec{h} + qv_n\right\} ds + \int_{\Gamma_s}\left\{-\vec{w}\cdot\vec{t}^{\,f} + qv_n\right\} ds + \int_{\Gamma_g} qv_n ds = 0 \end{aligned} \tag{3.11}$$

for all $\vec{w} \in \vec{\mathcal{W}}_h^k$ and $q \in \mathcal{P}_h^k$. In this equation, the superscripts *h, k* of the discrete approximation of the continuous variables $\vec{v}^{(h,k)}$ have been omitted for simplicity. Again, the integral containing the traction $\vec{t}^{\,f}$ in the previous equation is not specified yet. It will be determined from the equations governing the motion of the surrounding vessel wall, after a number of assumptions are made. Before describing the treatment of the solid domain, it is important to recall that the standard Galerkin method is unstable for advection-dominated flows and in the diffusion dominated limit for equal-order interpolation of velocity and pressure. A stabilized method is utilized to address these deficiencies of Galerkin's method. The formulation becomes:

Find $\vec{v} \in \vec{\mathcal{S}}_h^k$ and $p \in \mathcal{P}_h^k$ such that

$$\begin{aligned} B(\vec{w},q;\vec{v},p) &= B_G(\vec{w},q;\vec{v},p) \\ &+\sum_{e=1}^{n_{el}} \int_{\bar{\Omega}_e} \left\{ (\vec{v}\cdot\nabla)\,\vec{w}\cdot\tau_M \vec{\mathcal{L}}\,(\vec{v},p) + \nabla\cdot\vec{w}\tau_C\nabla\cdot\vec{v} \right\} d\vec{x} \\ &+\sum_{e=1}^{n_{el}} \int_{\bar{\Omega}_e} \left\{ \vec{w}\cdot\left(\rho\,\overset{\Delta}{\vec{v}}\cdot\nabla\vec{v}\right) + \left(\vec{\mathcal{L}}\,(\vec{v},p)\cdot\nabla\vec{w}\right)\left(\bar{\tau}\,\vec{\mathcal{L}}\,(\vec{v},p)\cdot\vec{v}\right) \right\} d\vec{x} \\ &+\sum_{e=1}^{n_{el}} \int_{\bar{\Omega}_e} \nabla q\cdot\frac{\tau_M}{\rho}\vec{\mathcal{L}}\,(\vec{v},p)\,d\vec{x} = 0 \end{aligned} \tag{3.12}$$

for all $\vec{w} \in \vec{\mathcal{W}}_h^k$ and $q \in \mathcal{P}_h^k$. $\vec{\mathcal{L}}\,(\vec{v},p)$ is the residual vector of the momentum equation

$$\vec{\mathcal{L}}\,(\vec{v},p) = \rho\vec{v}_{,t} + \rho\vec{v}\cdot\nabla\vec{v} + \nabla p - \nabla\cdot\underset{\sim}{\tau} - \vec{f} \tag{3.13}$$

The additional integrals in equation (3.12) represent the different stabilization terms for the incompressible flow equations as discussed in [61], [16] and [58]. Here $\overset{\Delta}{\vec{v}}$ is a conservation-restoring advective velocity whose expression is given by:

$$\overset{\Delta}{\vec{v}} = -\frac{\tau_M}{\rho}\vec{\mathcal{L}}\,(\vec{v},p) \tag{3.14}$$

The stabilization parameters for continuity, momentum and the advective term are given by the following expressions:

$$\tau_M = \frac{1}{\sqrt{\left(2c_1/\Delta t\right)^2 + \vec{v} \cdot \underset{\sim}{g}\vec{v} + c_2 \nu^2 \left(\underset{\sim}{g} : \underset{\sim}{g} + \omega^2\right)}} \tag{3.15}$$

$$\tau_C = \frac{\rho}{8\tau_M \operatorname{tr}\left(\underset{\sim}{g}\right)} \frac{C_{\tau_C}}{c_1} \tag{3.16}$$

$$\overline{\tau} = \frac{\tau_M}{\sqrt{\vec{\mathcal{L}}\left(\vec{v}, p\right) \cdot \underset{\sim}{g}\vec{\mathcal{L}}\left(\vec{v}, p\right)}} \tag{3.17}$$

where c_1 and c_2 are constants defined from the one-dimensional scalar model problem of the advection-diffusion equation. The default value for c_1 is one, and c_2 depends on the order of the basis functions used according to the following table:

Order of Basis Functions	c_2
1	36.0
2	60.0
3	128.0

Table 3-1: Values of c_2 for different basis functions orders.

ω is the angular velocity of the reference frame, C_{τ_C} is a scale factor for τ_C which for the default tau matrix used in the present formulation takes the value of one, and $\underset{\sim}{g}$ is the covariant metric tensor:

$$\underset{\sim}{g} = \left(\vec{\xi}_{,\vec{x}}\right)^T \vec{\xi}_{,\vec{x}} \tag{3.18}$$

These stabilization terms are based on those defined by Shakib [62] and have been used by Taylor *et al.* [16] and Whiting and Jansen [58].

3.2.3 Vessel Wall Equations (Strong Form)

The classic elastodynamics equations are used to describe the motion of the vessel wall in a domain $\boldsymbol{\Omega}^s \in \Re^{n_{sd}}$ (see Figure 3-1). The vessel wall mechanics are herein approximated using a thin-walled structure assumption, and therefore the solid domain $\boldsymbol{\Omega}^s$ can be topologically related to the surface defining the lateral boundary of the fluid domain Γ_s. The solid's weak form defined in the domain $\boldsymbol{\Omega}^s$ will be related to the fluid traction integral on the lateral boundary of the fluid domain. This assumption together with the consideration of a membrane model for the vessel wall nodes will enable a strong coupling of degrees-of-freedom of the fluid and solid domains and will result in an expression for the unknown integral traction

$$-\int_{\Gamma_s} \vec{w} \cdot \vec{t}^{\,f} ds \tag{3.19}$$

of equation (3.11).

The strong form of the vessel wall problem can be described as follows:

Given $\vec{b}^s:\Omega^s \times (0,T) \to \Re^{n_{sd}}$, $\vec{g}^s:\Gamma^s_g \times (0,T) \to \Re^{n_{sd}}$, $\vec{h}^s:\Gamma^s_h \times (0,T) \to \Re^{n_{sd}}$, $\vec{u}^0:\Omega^s \to \Re^{n_{sd}}$ and $\vec{u}^0_{,t}:\Omega^s \to \Re^{n_{sd}}$;

find $\vec{u}(\vec{x},t), \forall \vec{x} \in \Omega^s$, $\forall t \in [0,T]$ such that

$$\rho^s \vec{u}_{,tt} = \nabla \cdot \underset{\sim}{\sigma}^s + \vec{b}^s, \quad (\vec{x},t) \in \Omega^s \times (0,T) \tag{3.20}$$

$$\vec{u} = \vec{g}^s, \quad (\vec{x},t) \in \Gamma^s_g \times (0,T) \tag{3.21}$$

$$\vec{t}_{\vec{n}} = \underset{\sim}{\sigma}^s \vec{n} = \vec{h}^s, \quad (\vec{x},t) \in \Gamma^s_h \times (0,T) \tag{3.22}$$

$$\left.\begin{array}{l} \vec{u}(\vec{x},0) = \vec{u}^0(\vec{x}) \\ \vec{u}_{,t}(\vec{x},0) = \vec{u}^0_{,t}(\vec{x}) \end{array}\right., \quad \vec{x} \in \Omega^s \tag{3.23}$$

where $\vec{u}$ is the displacement field, ρ^s is the density of the vessel wall, $\vec{b}^s$ is the prescribed body force per unit volume, $\underset{\sim}{\sigma}^s$ is the vessel wall stress tensor, and $\vec{u}^0(\vec{x})$ and $\vec{u}^0_{,t}(\vec{x})$ are the given initial conditions for displacement and velocity, respectively. Furthermore, Γ^s_g and Γ^s_h represent the parts of the boundary of Ω^s where the essential ($\vec{g}^s$) and natural ($\vec{h}^s$) boundary conditions are prescribed.

3.2.4 Vessel Wall Equations (Weak Form)

In order to relate the solid problem stated in equations (3.20)-(3.23) with the lateral boundary of the fluid domain, Ω^s needs to be mapped on Γ_s. Assuming a thin-walled structure, integrals defined on Γ^s_h and Ω^s can be related with integrals on the lateral boundary of the fluid domain Γ_s according to the following expressions

$$\int_{\Omega^s} (\bullet)\, dx = \zeta \int_{\Gamma_s} (\bullet)\, ds \tag{3.24}$$

$$\int_{\Gamma_h^s} (\bullet)\, ds = \zeta \int_{\partial\Gamma_h} (\bullet)\, dl \tag{3.25}$$

where ζ represents the vessel wall thickness.

The surface traction $\vec{t}^{\,f}$ acting on the fluid lateral boundary due to the interaction with the solid is equal and opposite to the surface traction $\vec{t}^{\,s}$ acting on the vessel wall due to the fluid:

$$\vec{t}^{\,f} = -\vec{t}^{\,s} \tag{3.26}$$

Invoking once again the thin wall approximation, this surface traction $\vec{t}^{\,s}$ can be related to a body force $\vec{b}^{\,s}$ acting on the solid domain since for a thin-enough structure the internal surface traction $\vec{t}^{\,s}$ will be felt uniformly through the wall thickness ζ. Therefore, it follows that

$$\vec{b}^{\,s} = -\frac{\vec{t}^{\,f}}{\zeta} \tag{3.27}$$

and thus it is possible to relate the unknown integral term given by equation (3.19) with the weak form for the vessel wall problem. This approach to the coupling of the fluid and solid momentum equations is analogous to Womersley's

[57] derivation of an analytical solution for axisymmetric pulsatile blood flow in a cylindrical elastic vessel. There, Womersley considered just two components of the stress due to the fluid motion being applied to the vessel wall: a longitudinal component (related to the viscous stress) and a radial component (related to the pressure). Here, the full stress vector $\vec{t}^{\,f} = -\vec{t}^{\,s}$ is considered and the motion is, in general, three-dimensional.

We now derive the finite element counterpart of equations (3.20)-(3.23). Since a strong coupling of the degrees-of-freedom of the fluid and solid domains is considered, the displacement, velocity and acceleration fields on the fluid-solid interface are identical. Furthermore, since the weak form of the elastodynamics equations has the same differentiability requirements on the functional spaces as the fluid weak form, we can adopt for the vessel wall problem the same type of functional spaces as in the fluid domain:

$$\vec{\mathcal{S}}_h^{sk} = \left\{ \vec{u} \,|\, \vec{u}(\cdot,t) \in H^1(\Omega^s)^{n_{sd}}, t \in [0,T], \vec{u}|_{\vec{x} \in \bar{\Omega}_e^s} \in P_k(\bar{\Omega}_e^s)^{n_{sd}}, \vec{u}(\cdot,t) = \hat{\vec{g}}^s \text{ on } \Gamma_g^s \right\} \quad (3.28)$$

$$\vec{\mathcal{W}}_h^{sk} = \left\{ \vec{w} \,|\, \vec{w}(\cdot,t) \in H^1(\Omega^s)^{n_{sd}}, t \in [0,T], \vec{w}|_{\vec{x} \in \bar{\Omega}_e^s} \in P_k(\bar{\Omega}_e^s)^{n_{sd}}, \vec{w}(\cdot,t) = \vec{0} \text{ on } \Gamma_g^s \right\} \quad (3.29)$$

Considering this, the semi-discrete Galerkin finite element formulation produces the following weak form:

Find $\vec{v} \in \vec{\mathcal{S}}_h^{sk}$ such that

$$\int_{\Omega^s} \rho^s \vec{w} \cdot \vec{v}_{,t} d\vec{x} + \int_{\Omega^s} \nabla \vec{w} : \underset{\sim}{\sigma}^s d\vec{x} = \int_{\Omega^s} \vec{w} \cdot \vec{b}^s d\vec{x} + \int_{\Gamma_h^s} \vec{w} \cdot \vec{h}^s ds \tag{3.30}$$

for all $\vec{w} \in \vec{\mathcal{W}}_h^{sk}$. The acceleration term has been written as the time derivative of the velocity rather than as the second time derivative of the displacement field, since the goal is to express the vessel wall equations in terms of the fluid unknowns.

Now, equations (3.24) and (3.25) are utilized to map equation (3.30) into the lateral boundary of the fluid domain Γ_s:

$$\zeta \int_{\Gamma_s} \rho^s \vec{w} \cdot \vec{v}_{,t} ds + \zeta \int_{\Gamma_s} \nabla \vec{w} : \underset{\sim}{\sigma}^s ds = \zeta \int_{\Gamma_s} \vec{w} \cdot \vec{b}^s ds + \zeta \int_{\partial\Gamma_h} \vec{w} \cdot \vec{h}^s dl \tag{3.31}$$

Considering the expression for the body force $\vec{b}^s$ given by equation (3.27), the final expression of the weak form for the solid domain is

$$-\int_{\Gamma_s} \vec{w} \cdot \vec{t}^f ds = \zeta \int_{\Gamma_s} \rho^s \vec{w} \cdot \vec{v}_{,t} ds + \zeta \int_{\Gamma_s} \nabla \vec{w} : \underset{\sim}{\sigma}^s ds - \zeta \int_{\partial\Gamma_h} \vec{w} \cdot \vec{h}^s dl \tag{3.32}$$

3.2.5 Combined Formulation: the CMM-FSI Weak Form

Equation (3.32) provides an expression for the unknown term in equation (3.11) as a function of the solid internal stresses and inertial forces. Combining these two equations together results in the following weak Galerkin form for the CMM-FSI method:

$$
\begin{aligned}
B_G(\vec{w},q;\vec{v},p) = {} & \int_\Omega \left\{ \vec{w} \cdot \left(\rho \vec{v}_{,t} + \rho \vec{v} \cdot \nabla \vec{v} - \vec{f} \right) + \nabla \vec{w} \colon \left(-p \underset{\sim}{I} + \underset{\sim}{\tau} \right) - \nabla q \cdot \vec{v} \right\} d\vec{x} \\
& - \int_{\Gamma_h} \vec{w} \cdot \vec{h} ds + \int_{\Gamma_h} q v_n ds + \int_{\Gamma_g} q v_n ds \\
& \boxed{+ \zeta \int_{\Gamma_s} \left\{ \vec{w} \cdot \rho^s \vec{v}_{,t} + \nabla \vec{w} \colon \underset{\sim}{\sigma}^s (\vec{u}) \right\} ds - \zeta \int_{\partial \Gamma_h} \vec{w} \cdot \vec{h}^s dl + \int_{\Gamma_s} q v_n ds}
\end{aligned}
\tag{3.33}
$$

The boxed integrals in equation (3.33) define the new terms added to the rigid wall theory. The stabilized form of equation (3.33) does not change with respect to the one given by equation (3.12) since the stabilization terms affect only the interior fluid elements. Therefore, the final expression for the weak form of the CMM-FSI method is:

$$
\begin{aligned}
B(\vec{w},q;\vec{v},p) = {} & \int_\Omega \left\{ \vec{w} \cdot \left(\rho \vec{v}_{,t} + \rho \vec{v} \cdot \nabla \vec{v} - \vec{f} \right) + \nabla \vec{w} \colon \left(-p \underset{\sim}{I} + \underset{\sim}{\tau} \right) - \nabla q \cdot \vec{v} \right\} d\vec{x} \\
& - \int_{\Gamma_h} \vec{w} \cdot \vec{h} ds + \int_{\Gamma_h} q v_n ds + \int_{\Gamma_g} q v_n ds \\
& + \sum_{e=1}^{n_{el}} \int_{\bar{\Omega}_e} \nabla q \cdot \frac{\tau_M}{\rho} \vec{\mathcal{L}}(\vec{v},p) d\vec{x} + \sum_{e=1}^{n_{el}} \int_{\bar{\Omega}_e} \left\{ (\vec{v} \cdot \nabla) \vec{w} \cdot \tau_M \vec{\mathcal{L}}(\vec{v},p) + \nabla \cdot \vec{w} \tau_C \nabla \cdot \vec{v} \right\} d\vec{x} \\
& + \sum_{e=1}^{n_{el}} \int_{\bar{\Omega}_e} \left\{ \vec{w} \cdot \left(\rho \overset{\Delta}{\vec{v}} \cdot \nabla \vec{v} \right) + \left(\vec{\mathcal{L}}(\vec{v},p) \cdot \nabla \vec{w} \right) \left(\bar{\tau} \vec{\mathcal{L}}(\vec{v},p) \cdot \vec{v} \right) \right\} d\vec{x} \\
& \boxed{+ \zeta \int_{\Gamma_s} \left\{ \vec{w} \cdot \rho^s \vec{v}_{,t} + \nabla \vec{w} \colon \underset{\sim}{\sigma}^s (\vec{u}) \right\} ds - \zeta \int_{\partial \Gamma_h} \vec{w} \cdot \vec{h}^s dl + \int_{\Gamma_s} q v_n ds} = 0
\end{aligned}
\tag{3.34}
$$

There are other more general formulations that consider a single weak form for the combined fluid-structure problem (see [39]), where the fluid and the structure and the structure are considered as a unique continuous medium in an ALE frame. However, in the work presented here (as mentioned in the introduction and to be shown in detail in section 3.3), we consider the same degrees-of-freedom for the fluid and the structure.

In order to complete the formulation of the method, we need to discuss the details of the mechanical model for the vessel wall, as well as the linearization and time integration schemes used to discretize equation (3.34).

3.3 Finite Element Model for the Vessel Wall

The choice of infinitesimal elasticity theory for the constitutive model of the wall represents an appropriate first approximation justified by experimental evidence showing that the vessel wall constitutive behavior can be reasonably assumed as linear within the physiological range of pressures [63]. Furthermore, from a numerical standpoint, the adopted fixed-mesh strategy to describe the fluid-solid interface is consistent with utilizing infinitesimal elasticity theory for the wall. The combination of a linearized kinematics approach and a fixed mesh is essential in ensuring a minimal increment in computational effort as compared to rigid wall models. Furthermore, to enforce the identity of the degrees-of-freedom of the lateral boundary of the fluid domain and the vessel wall, a membrane element with only translational degrees-of-freedom represents the simplest and most convenient choice.

In this section, we derive expressions for the vessel wall stress tensor $\underset{\sim}{\sigma}^{s}(\bar{u})$ and mass integrals of equation (3.34), particularized for a membrane-like behavior.

3.3.1 Mass Matrix Derivation

The integral representing the mass of the vessel wall in equation (3.34)

$$\zeta \int_{\Gamma_s} \bar{w} \cdot \rho^s \bar{v}_{,t} ds \tag{3.35}$$

does not require special treatment due to the strong coupling of the degrees-of-freedom of the solid and the fluid. It can be regarded as providing additional mass (not to be confused with the "added mass effect" typical of fluid-solid interaction problems [64]) to the fluid nodes at the interface with the solid. In other words, these nodes receive mass contributions from both the fluid and the solid domains. The implementation of this integral is therefore achieved by mimicking the structure of the fluid mass integral term

$$\int_{\Omega} \bar{w} \cdot \rho \bar{v}_{,t} d\bar{x} \tag{3.36}$$

3.3.2 Stiffness Matrix Derivation

In this section, we derive the expression of the integral describing the stiffness of the vessel wall in equation (3.34), viz.

$$\zeta \int_{\Gamma_s} \nabla \bar{w} : \underset{\sim}{\sigma}^{s}(\bar{u}) ds \tag{3.37}$$

We start by recalling the constitutive equation for a linear, elastic material. This expression is given by:

$$\underset{\sim}{\sigma}^{s} = \underset{\sim}{C} : \underset{\sim}{\varepsilon} \tag{3.38}$$

where $\underset{\sim}{C}$ is a fourth-order tensor of material constants and

$$\underset{\sim}{\varepsilon} = \frac{1}{2}\left(\nabla\vec{u} + (\nabla\vec{u})^{T}\right) = \mathrm{sym}(\nabla\vec{u}) \tag{3.39}$$

is the infinitesimal strain tensor. By virtue of the symmetry of the tensor $\underset{\sim}{\sigma}^{s}$, the inner product defined in equation (3.37) can be rewritten as:

$$\zeta\int_{\Gamma_s} \mathrm{sym}(\nabla\vec{w}) : \underset{\sim}{\sigma}^{s} ds = \zeta\int_{\Gamma_s} \mathrm{sym}(\nabla\vec{w}) : \underset{\sim}{C} : \mathrm{sym}(\nabla\vec{u})\, ds \tag{3.40}$$

The mesh of the vessel wall will be defined by linear triangles when the internal fluid mesh consists of linear tetrahedral elements. However, it is well known that linear, constant strain triangles (CST) representing only membrane modes are inappropriate when used in three-dimensional geometries with transverse loads (see [65,66]). Therefore, to stabilize the linear triangle, we augment the stiffness of the linear membrane element with a transverse shear as illustrated in Figure 3-2. Note that using this approach, only translational degrees-of-freedom are needed to describe the dynamics of the vessel wall.

In order to correctly represent the plane stress behavior (enhanced with the transverse shear modes mentioned previously) for the linear surface triangles, one must calculate the tensors given by equation (3.40) in a local reference system, coplanar with the triangle.

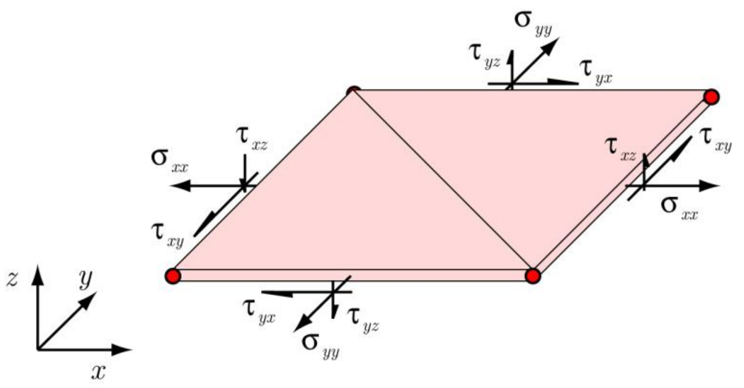

Figure 3-2: Stresses of a typical membrane patch with transverse shear.

The coordinate transformation between the global and local reference frames is given by the orthogonal matrix $\underset{\sim}{\theta}$ whose components are (see Figure 3-3):

$$\underset{\sim}{\theta} = \left[\theta_{ij}\right] = \left[\vec{e}_i \cdot \vec{e}^{\,l}_j\right] \tag{3.41}$$

where $\vec{e}_i$ and $\vec{e}^{\,l}_j$ are the unit basis vectors of the global and local reference frames, respectively.

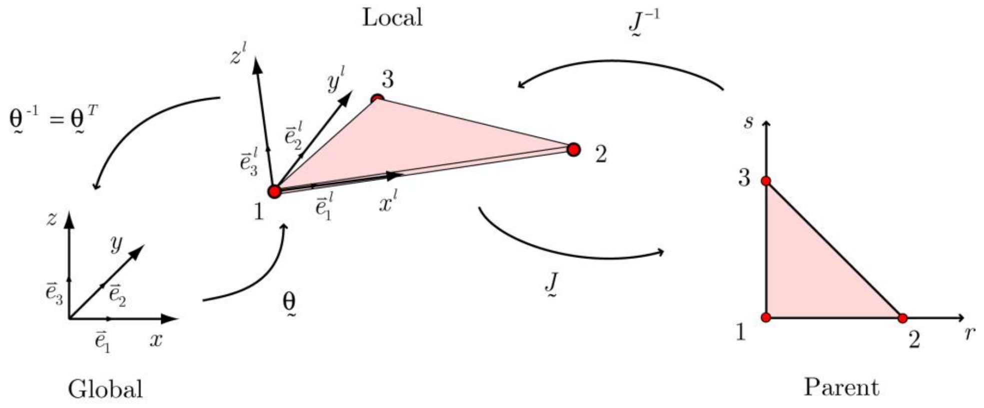

Figure 3-3: Coordinate transformations between the Global, Local and Parent reference frames.

The rotated coordinates of the vessel wall nodes are:

$$\vec{x}_a^l = \underset{\sim}{\theta}\vec{x}_a \quad , \quad a = 1,2,3; \qquad \left\{\vec{x}_a^l\right\} = \begin{Bmatrix} x_a^l \\ y_a^l \\ z_a^l \end{Bmatrix} \tag{3.42}$$

A similar operation must be performed to obtain the nodal displacements in the local reference frame $\vec{u}_a^l$. Furthermore, the (local) strains $\vec{\varepsilon}^l$ are related to the nodal displacements by a matrix operator $\underset{\sim}{B}$

$$\vec{\varepsilon}^l = \underset{\sim}{B}\vec{u}^l \tag{3.43}$$

whose expression will be derived shortly.

For isoparametric linear elements, the displacement field $\vec{u}^l$ is given by:

$$\vec{u}^l = \sum_{a=1}^{3} N_a(r,s)\ \vec{u}_a^l \tag{3.44}$$

Where $N_a(r,s)$ are the triangular shape functions given by

$$\begin{cases} N_1 = 1 - r - s \\ N_2 = r \\ N_3 = s \end{cases} \tag{3.45}$$

Recalling that for a thin membrane we can neglect variations across the thickness (and therefore $\sigma_{zz}^l = 0$), and using the symmetries of $\underset{\sim}{C}$, $\underset{\sim}{\varepsilon}$ and $\underset{\sim}{\sigma}^s$, it is possible to work with a reduced vector (i.e., index-collapsed) form of these tensors and a second-order tensor of material constants $\underset{\sim}{D}$ which relates the following *local* stress and strain *vectors*,

$$\left\{\vec{\sigma}^{s,l}\right\} = \left\{\begin{matrix} \sigma_{xx}^{l} \\ \sigma_{yy}^{l} \\ \tau_{xy}^{l} \\ \tau_{xz}^{l} \\ \tau_{yz}^{l} \end{matrix}\right\}, \qquad \left\{\vec{\varepsilon}^{l}\right\} = \left\{\begin{matrix} \dfrac{\partial u^{l}}{\partial x^{l}} \\ \dfrac{\partial v^{l}}{\partial y^{l}} \\ \dfrac{\partial u^{l}}{\partial y^{l}} + \dfrac{\partial v^{l}}{\partial x^{l}} \\ \dfrac{\partial w^{l}}{\partial x^{l}} \\ \dfrac{\partial w^{l}}{\partial y^{l}} \end{matrix}\right\} \tag{3.46}$$

Here u^{l}, v^{l}, and w^{l} are the three components of the displacement vector $\vec{u}^{l}$ and x^{l}, y^{l} are the local nodal coordinates. We now define the material stiffness tensor for a plane stress state of an incompressible, isotropic solid augmented by the transverse shear stresses τ_{xz}^{l} and τ_{yz}^{l}. This tensor can be written as follows:

$$\underset{\sim}{D} = \frac{E}{\left(1-\nu^{2}\right)} \begin{bmatrix} 1 & \nu & 0 & 0 & 0 \\ \nu & 1 & 0 & 0 & 0 \\ 0 & 0 & 0.5(1-\nu) & 0 & 0 \\ 0 & 0 & 0 & 0.5k(1-\nu) & 0 \\ 0 & 0 & 0 & 0 & 0.5k(1-\nu) \end{bmatrix} \tag{3.47}$$

where E and ν are the Young's modulus and Poisson ratio coefficients respectively, and the parameter k accounts for a parabolic variation of transverse shear stress through the membrane. For a solid, homogeneous plate this parameter takes the value of $5/6$ ([65,66]).

Using a convenient finite element interpolation, and the index-collapsed tensors defined by equations (3.46)-(3.47), equation (3.40) will produce a *local* elemental stiffness matrix $\underset{\sim}{K}_e^{s,l}$ for the vessel wall triangles of the form:

$$\underset{\sim}{K}_e^{s,l} = \zeta \int_{\Gamma_s^e} \underset{\sim}{B}^T \underset{\sim}{D} \underset{\sim}{B} ds \tag{3.48}$$

We need to find expressions for the gradient of nodal displacements with respect to the local reference system $\vec{e}_i^{\,l}$, as expressed in equation (3.46). Considering the interpolation given by equations (3.44)-(3.45), we can calculate the gradient of any component of the displacement field by using the following vector operator:

$$\begin{Bmatrix} \dfrac{\partial}{\partial x^l} \\ \dfrac{\partial}{\partial y^l} \end{Bmatrix} = \underset{\sim}{J}^{-1} \begin{Bmatrix} \dfrac{\partial}{\partial r} \\ \dfrac{\partial}{\partial s} \end{Bmatrix} = \underset{\sim}{J}^{-1} \begin{bmatrix} -1 & 1 & 0 \\ -1 & 0 & 1 \end{bmatrix} \tag{3.49}$$

where $\underset{\sim}{J}^{-1}$ is the inverse of the jacobian matrix relating the local and parent reference frames (see Figure 3-3). For a linear triangle, these matrices are:

$$\underset{\sim}{J} = \begin{bmatrix} x_2^l - x_1^l & y_2^l - y_1^l \\ x_3^l - x_1^l & y_3^l - y_1^l \end{bmatrix} \tag{3.50}$$

$$\underset{\sim}{J}^{-1} = \frac{1}{2A_e} \begin{bmatrix} y_3^l - y_1^l & y_1^l - y_2^l \\ x_1^l - x_3^l & x_2^l - x_1^l \end{bmatrix} \tag{3.51}$$

where A_e is the surface area of the triangular element under consideration. The final expression for the gradient operator is as follows:

$$\left\{\begin{matrix}\dfrac{\partial}{\partial x^l}\\ \dfrac{\partial}{\partial y^l}\end{matrix}\right\}=\frac{1}{2A_e}\begin{bmatrix}y_3^l-y_1^l & y_1^l-y_2^l\\ x_1^l-x_3^l & x_2^l-x_1^l\end{bmatrix}\begin{bmatrix}-1 & 1 & 0\\ -1 & 0 & 1\end{bmatrix}=\frac{1}{2A_e}\begin{bmatrix}y_2^l-y_3^l & y_3^l-y_1^l & y_1^l-y_2^l\\ x_3^l-x_2^l & x_1^l-x_3^l & x_2^l-x_1^l\end{bmatrix} \tag{3.52}$$

We need to combine this expression for the spatial gradient with the right nodal values in order to generate the right components of the (local) strain vector $\vec{\varepsilon}^{\,l}$, viz.

$$\left\{\vec{\varepsilon}^{\,l}\right\}=\frac{1}{2A_e}\begin{bmatrix}y_{23}^l & 0 & 0 & y_{31}^l & 0 & 0 & y_{12}^l & 0 & 0\\ 0 & x_{32}^l & 0 & 0 & x_{13}^l & 0 & 0 & x_{21}^l & 0\\ x_{32}^l & y_{23}^l & 0 & x_{13}^l & y_{31}^l & 0 & x_{21}^l & y_{12}^l & 0\\ 0 & 0 & y_{23}^l & 0 & 0 & y_{31}^l & 0 & 0 & y_{12}^l\\ 0 & 0 & x_{32}^l & 0 & 0 & x_{13}^l & 0 & 0 & x_{21}^l\end{bmatrix}\left\{\begin{matrix}u_1^l\\ v_1^l\\ w_1^l\\ u_2^l\\ v_2^l\\ w_2^l\\ u_3^l\\ v_3^l\\ w_3^l\end{matrix}\right\} \tag{3.53}$$

where $x_{ij}^l=x_i^l-x_j^l$ (similarly for y_{ij}^l). Using equations (3.43) and (3.53), it follows that:

$$\utilde{B} = \frac{1}{2A_e}\begin{bmatrix} y_{23}^l & 0 & 0 & y_{31}^l & 0 & 0 & y_{12}^l & 0 & 0 \\ 0 & x_{32}^l & 0 & 0 & x_{13}^l & 0 & 0 & x_{21}^l & 0 \\ x_{32}^l & y_{23}^l & 0 & x_{13}^l & y_{31}^l & 0 & x_{21}^l & y_{12}^l & 0 \\ 0 & 0 & y_{23}^l & 0 & 0 & y_{31}^l & 0 & 0 & y_{12}^l \\ 0 & 0 & x_{32}^l & 0 & 0 & x_{13}^l & 0 & 0 & x_{21}^l \end{bmatrix} \tag{3.54}$$

and therefore the local elemental vessel wall stiffness matrix $\utilde{K}_e^{s,l}$ can be expressed as the 9×9 matrix given by:

$$\left(\utilde{K}_e^s\right)^l = \zeta \utilde{B}^T \utilde{D} \utilde{B} \int_{\Gamma_s^e} ds = \zeta \utilde{B}^T \utilde{D} \utilde{B} A_e \tag{3.55}$$

This local stiffness matrix must then be rotated back into the global reference frame using the 9×9 rotation tensor

$$\utilde{\Theta} = \begin{bmatrix} \utilde{\theta} & \utilde{0} & \utilde{0} \\ \utilde{0} & \utilde{\theta} & \utilde{0} \\ \utilde{0} & \utilde{0} & \utilde{\theta} \end{bmatrix} \tag{3.56}$$

where $\utilde{\theta}$ is the tensor given by equation (3.41). Therefore, the expression for *global* vessel wall stiffness $\utilde{K}_e^s$ results in

$$\utilde{K}_e^s = \utilde{\Theta}^T \utilde{K}_e^{s,l} \utilde{\Theta} = \utilde{\Theta}^T \left(\zeta \utilde{B}^T \utilde{D} \utilde{B} A_e\right) \utilde{\Theta} \tag{3.57}$$

This matrix represents, under the assumptions described in this section, a convenient discretization for the integral term containing the vessel wall stress tensor $\utilde{\sigma}^s(\vec{u})$ in equation (3.34).

We proceed now with the description of the time integration and linearization schemes utilized in the formulation.

3.4 Time Integration and Linearization Algorithms

The weak form given by equation (3.34) can be written as a semi-discrete system of nonlinear first-order ordinary differential equations in time:

$$\left.\begin{aligned} &\vec{R}(\vec{u},\vec{v},\vec{v}_{,t},p) = \vec{0} &&\text{in } \Omega \\ &\vec{v} = \vec{u}_{,t} &&\text{on } \Gamma_s \end{aligned}\right\} \tag{3.58}$$

The vector $\vec{R}$ represents the set of nodal nonlinear residuals defined for each point of the finite element mesh.

In order to describe the time evolution of the solution to this system, we need to introduce a suitable time integration strategy. Since the problem defined by equation (3.58) is nonlinear, a linearization algorithm is needed. Both operations –time stepping and linearization- are intimately related.

In this section, we describe these two algorithms as they have been implemented in the finite-element code PHASTA©[49]. The section is organized as follows: we first provide a basic description of the time stepping/linearization algorithms as implemented in PHASTA©[49]. We then proceed to characterize the generalized-α method applied to a simple linear model problem. We then describe the generalized-α method applied to the CMM-FSI equations. Lastly, for the sake of completeness, we provide the expressions of the left-hand-side matrices obtained from the linearization scheme.

3.4.1 Basic Steps of the Time Integration/Linearization Algorithms as Implemented in PHASTA©

Figure 3-4 shows the basic steps involved in the time integration/linearization algorithm.

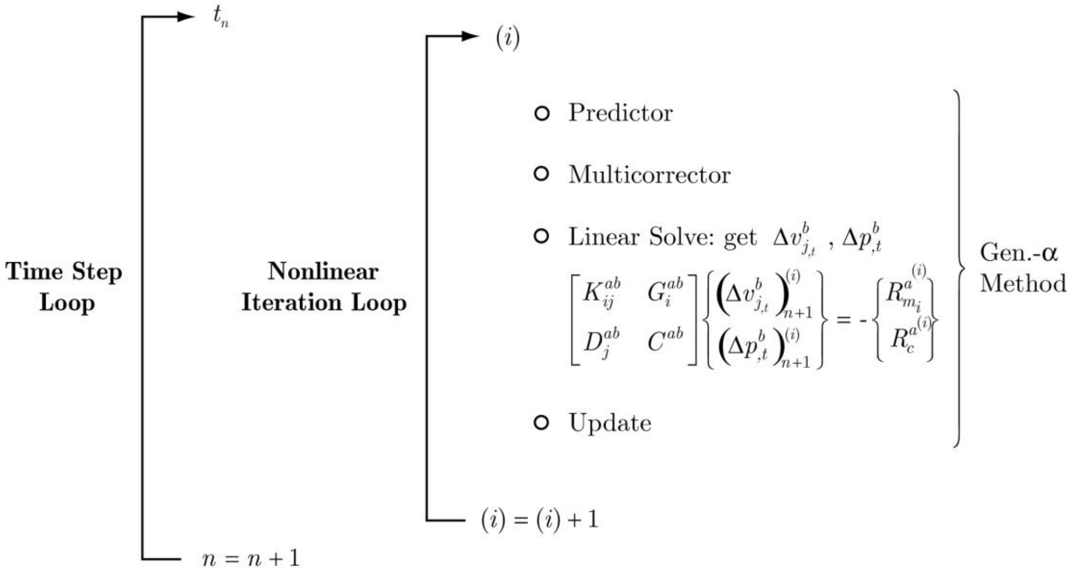

Figure 3-4: Time stepping and nonlinear iteration loops in the solution strategy.

Here, the index n refers to the time step number, whereas the superscript (i) represents the nonlinear iteration counter. The superscripts a,b represent the local node numbers and the subscripts i,j the spatial dimensions.

Within each time step, there is a nonlinear iteration loop to obtain the solution at time t_n to the nonlinear system defined in equation (3.58) using a Newton-Raphson strategy. It is important to define the way this equation is linearized to obtain a linear system of the type shown in Figure 3-4. We will provide the specific details of this linearization in section 3.4.3.

The system (3.58) can also be written as

$$\begin{Bmatrix} \vec{R}_m \\ R_c \end{Bmatrix}_A = \begin{Bmatrix} \vec{0} \\ 0 \end{Bmatrix}_A \quad , \; A = 1,\ldots,n_{\text{nodes}} \tag{3.59}$$

where $\vec{R}_m$ and R_c represent the residuals of the momentum and continuity equations, respectively:

$$\begin{aligned} \vec{R}_m = & \int_{\Omega} \left\{ \vec{w} \cdot \left(\rho \vec{v}_{,t} + \rho \vec{v} \cdot \nabla \vec{v} - \vec{f} \right) + \nabla \vec{w} : \left(-p \underset{\sim}{I} + \underset{\sim}{\tau} \right) \right\} d\vec{x} \\ & + \zeta \int_{\Gamma_s} \left\{ \vec{w} \cdot \rho^s \vec{v}_{,t} + \nabla \vec{w} : \underset{\sim}{\sigma}^s \left(\vec{u} \right) \right\} ds - \zeta \int_{\partial \Gamma_h} \vec{w} \cdot \vec{h}^s dl - \int_{\Gamma_h} \vec{w} \cdot \vec{h} ds \\ & + \sum_{e=1}^{n_{el}} \int_{\bar{\Omega}_e} \left\{ \left(\vec{v} \cdot \nabla \right) \vec{w} \cdot \tau_M \vec{\mathcal{L}} \left(\vec{v}, p \right) + \nabla \cdot \vec{w} \tau_C \nabla \cdot \vec{v} \right\} d\vec{x} \\ & + \sum_{e=1}^{n_{el}} \int_{\bar{\Omega}_e} \left\{ \vec{w} \cdot \left(\rho \overset{\Delta}{\vec{v}} \cdot \nabla \vec{v} \right) + \left(\vec{\mathcal{L}} \left(\vec{v}, p \right) \cdot \nabla \vec{w} \right) \left(\bar{\tau} \vec{\mathcal{L}} \left(\vec{v}, p \right) \cdot \vec{v} \right) \right\} d\vec{x} = \vec{0} \end{aligned} \tag{3.60}$$

$$\begin{aligned} R_c = & -\int_{\Omega} \nabla q \cdot \vec{v} d\vec{x} + \sum_{e=1}^{n_{el}} \int_{\bar{\Omega}_e} \nabla q \cdot \frac{\tau_M}{\rho} \vec{\mathcal{L}} \left(\vec{v}, p \right) d\vec{x} \\ & + \int_{\Gamma_s} q v_n ds + \int_{\Gamma_h} q v_n ds + \int_{\Gamma_g} q v_n ds \end{aligned} \tag{3.61}$$

Applying the Newton-Raphson method to equation (3.59) using the acceleration $v_{j,t}$ and time derivative of pressure $p_{,t}$ as linearization variables produces a system of the form:

$$\begin{bmatrix} \dfrac{\partial\left(R_i\right)_m^a}{\partial\left(v_{j,t}\right)_{n+1}^b} & \dfrac{\partial\left(R_i\right)_m^a}{\partial\left(p_{,t}\right)_{n+1}^b} \\ \dfrac{\partial\left(R_c\right)^a}{\partial\left(v_{j,t}\right)_{n+1}^b} & \dfrac{\partial\left(R_c\right)^a}{\partial\left(p_{,t}\right)_{n+1}^b} \end{bmatrix} \begin{Bmatrix} \left(\Delta v_{j,t}\right)_{n+1}^b \\ \left(\Delta p_{,t}\right)_{n+1}^b \end{Bmatrix} = -\begin{Bmatrix} \left(R_i\right)_m^a \\ R_c^a \end{Bmatrix} \tag{3.62}$$

The left-hand-side matrices shown in Figure 3-4 correspond to the partial derivatives of the momentum and continuity residual with respect to the linearization variables, as seen in the previous equation. Therefore, we have:

$$\begin{aligned} K_{ij}^{ab} &= \frac{\partial R_{m_i}^a}{\partial\left(v_{j,t}\right)_{n+1}^b}, & G_i^{ab} &= \frac{\partial R_{m_i}^a}{\partial\left(p_{,t}\right)_{n+1}^b} \\ D_j^{ab} &= \frac{\partial R_c^a}{\partial\left(v_{j,t}\right)_{n+1}^b}, & C^{ab} &= \frac{\partial R_c^a}{\partial\left(p_{,t}\right)_{n+1}^b} \end{aligned} \tag{3.63}$$

However, due to considerations in the linear algebra package used (AcuSolve© [67]), it is highly desirable to have an anti-symmetric left-hand-side matrix (i.e., $D_j^{ab} = -G_i^{ba}$). Gresho and Sani [59] provide additional details pertaining to this anti-symmetry. In order to make these two matrices anti-symmetric, a different definition of the continuity equation residual for the left-hand-side linearization is utilized in PHASTA©. The *Alternative Left-Hand-Side continuity residual* is referred to as R_c^{ALHS} and its expression is given by:

$$R_c^{ALHS} = \int_{\Omega} q\nabla \cdot \vec{v} d\vec{x} + \sum_{e=1}^{n_{el}} \int_{\bar{\Omega}_e} \nabla q \cdot \frac{\tau_M}{\rho} \vec{\mathcal{L}}(\vec{v}, p) d\vec{x} \tag{3.64}$$

which differs from equation (3.61) in the fact that the continuity term has not been integrated by parts, and therefore it does not have any boundary integrals. Considering this, we re-define the system given by equation (3.62) as follows:

$$\begin{bmatrix} \dfrac{\partial (R_i)_m^a}{\partial \left(v_{j,t}\right)_{n+1}^b} & \dfrac{\partial (R_i)_m^a}{\partial \left(p_{,t}\right)_{n+1}^b} \\ \dfrac{\partial \left(R_c^{ALHS}\right)^a}{\partial \left(v_{j,t}\right)_{n+1}^b} & \dfrac{\partial \left(R_c^{ALHS}\right)^a}{\partial \left(p_{,t}\right)_{n+1}^b} \end{bmatrix} \begin{Bmatrix} \left(\Delta v_{j,t}\right)_{n+1}^b \\ \left(\Delta p_{,t}\right)_{n+1}^b \end{Bmatrix} = -\begin{Bmatrix} (R_i)_m^a \\ R_c^a \end{Bmatrix}$$

$$\Downarrow \tag{3.65}$$

$$\begin{bmatrix} K_{ij}^{ab} & G_i^{ab} \\ D_j^{ab} & C^{ab} \end{bmatrix} \begin{Bmatrix} \left(\Delta v_{j,t}\right)_{n+1}^b \\ \left(\Delta p_{,t}\right)_{n+1}^b \end{Bmatrix} = -\begin{Bmatrix} (R_i)_m^a \\ R_c^a \end{Bmatrix}$$

where $(R_i)_m^a$, R_c^a and $\left(R_c^{ALHS}\right)^a$ are given by equations (3.60), (3.61) and (3.64), respectively.

To better understand the different steps of this time stepping algorithm, we review briefly the basic features of the generalized-α method applied to a first order ODE, as described in [68].

3.4.2 Generalized-α Method for a Simple ODE

The Generalized-α Method was first introduced by Chung and Hulbert [69]. It has been widely used in both structural and fluid mechanics problems, since it has a number of desirable properties. For a linear problem, it can be proven to be second-order accurate and unconditionally stable. It also enables the specification of user-defined numerical dissipation. We proceed to briefly describe the main features of this algorithm.

We consider a linear model problem representative of the system given by equation (3.58):

$$y_{,t} = \lambda y \tag{3.66}$$

The generalized-α method for integrating (3.66) from t_n to t_{n+1} (with $\Delta t = t_{n+1} - t_n$) reads as follows:

Residual equation

$$y_{,t_{n+\alpha_m}} = \lambda y_{n+\alpha_f} \tag{3.67}$$

Kinematic equation

$$y_{n+1} = y_n + \Delta t\left\{(1-\gamma)\, y_{,t_n} + \gamma y_{,t_{n+1}}\right\} \tag{3.68}$$

Interpolation equations

$$y_{,t_{n+\alpha_m}} = y_{,t_n} + \alpha_m\left(y_{,t_{n+1}} - y_{,t_n}\right) \tag{3.69}$$

$$y_{n+\alpha_f} = y_n + \alpha_f \left(y_{n+1} - y_n \right) \tag{3.70}$$

The generalized-α method uses different time interpolations for the main variable y and its time derivative $y_{,t}$. The main variable y is interpolated in time using the parameter α_f, see equation (3.70), whereas its time derivative $y_{,t}$ is interpolated in time using a parameter -α_m (see equation (3.69)). The two interpolated variables are related by the *residual* equation (3.67). Finally, equation (3.68) relates the values of the variables at times t_{n+1} and t_n using a third parameter γ. We can refer to this equation as the *kinematic* equation.

It can be proven (see [68]) that second-order accuracy can be obtained so long as

$$\gamma = \frac{1}{2} + \alpha_m - \alpha_f \tag{3.71}$$

Unconditionally stability requires that

$$\alpha_m \geq \alpha_f \geq \frac{1}{2} \tag{3.72}$$

If we refer to the spectral radius (obtained in the limit of an increasing time step) of the system defined by equations (3.67)-(3.70) as ρ_∞, then it is possible to express the parameters α_f and α_m as a function of this spectral radius ρ_∞ and therefore get the desired amount of numerical dissipation. The expressions for α_f and α_m as a function of ρ_∞ are:

$$\alpha_m = \frac{1}{2}\left(\frac{3-\rho_\infty}{1+\rho_\infty}\right) \tag{3.73}$$

$$\alpha_f = \frac{1}{1+\rho_\infty} \tag{3.74}$$

By specifying ρ_∞, we can set the level of damping of the frequencies that are high relative to the resolution of the time discretization. If ρ_∞ is set to zero, then the algorithm annihilates the highest frequency in one time step (in a linear problem). The method has the same spectral stability as Gear's two-step backward difference method [70]. On the other hand, if ρ_∞ is set to one, then the highest frequency, as well as the other frequencies, is preserved (again, in a linear case). This can compromise stability of the solution if the time discretization is not fine enough to resolve all the frequencies of the problem. In this case (ρ_∞=1), the method corresponds to the midpoint rule.

3.4.3 Generalized-α Method Applied to the CMM-FSI

As we have shown previously (see equation (3.62)), we have chosen to linearize the system given by equations (3.58)-(3.61) using Newton's method in two variables: one vector (the acceleration $\vec{v}_{,t}$), and one scalar (the pressure time-derivative $p_{,t}$).

When applying the generalized-α method presented in section 3.4.2 to the system defined by equations (3.58)-(3.61), we can define *residual*, *kinematic*, and *interpolation* expressions similar to those given for the simple ODE problem (equations (3.67)-(3.70)).

However, we must define the values of the generalized-α method parameters for each linearization variable: the velocity-acceleration parameters $\left(\alpha_{f_v}, \alpha_{m_v} \text{ and } \gamma_v\right)$ and the pressure parameters $\left(\alpha_{f_p}, \alpha_{m_p} \text{ and } \gamma_p\right)$.

Considering this, the *residual* equation for the CMM-FSI problem becomes

$$\vec{R}(\vec{u}_{n+\alpha_{f_v}}, \vec{v}_{n+\alpha_{f_v}}, \vec{v}_{,t_{n+\alpha_{m_v}}}, p_{n+\alpha_{f_p}}) = \vec{R}(\vec{u}_{n+\alpha_{f_v}}, \vec{v}_{n+\alpha_{f_v}}, \vec{v}_{,t_{n+\alpha_{m_v}}}, p_{n+1}) = \vec{0} \quad (3.75)$$

The *kinematic* and *interpolation* expressions are given by:

Velocity equations:

$$\vec{v}_{n+1} = \vec{v}_n + \Delta t\left\{\left(1-\gamma_v\right)\vec{v}_{,t_n} + \gamma_v \vec{v}_{,t_{n+1}}\right\} \quad (3.76)$$

$$\vec{v}_{,t_{n+\alpha_{m_v}}} = \vec{v}_{,t_n} + \alpha_{m_v}\left(\vec{v}_{,t_{n+1}} - \vec{v}_{,t_n}\right) \quad (3.77)$$

$$\vec{v}_{n+\alpha_{f_v}} = \vec{v}_n + \alpha_{f_v}\left(\vec{v}_{n+1} - \vec{v}_n\right) \quad (3.78)$$

Pressure equations:

The pressure time-derivative $p_{,t}$ does not appear explicitly in the incompressible fluid equations, but we can make the algorithm set the time-derivative to zero by choosing the pressure parameters corresponding to a Backward-Euler scheme:

$$\alpha_{f_p} = \alpha_{m_p} = \gamma_p = 1 \quad (3.79)$$

By doing this, we obtain:

$$p_{n+1} = p_n + \Delta t \left\{ \left(1 - \gamma_p\right) p_{,t_n} + \gamma_p p_{,t_{n+1}} \right\} = p_n + \Delta t p_{,t_{n+1}} \tag{3.80}$$

$$p_{,t_{n+\alpha_{m_p}}} = p_{,t_n} + \alpha_{m_p} \left(p_{,t_{n+1}} - p_{,t_n} \right) \tag{3.81}$$

$$p_{n+\alpha_{f_p}} = p_n + \alpha_{f_p} \left(p_{n+1} - p_n \right) \tag{3.82}$$

Note that this choice will make the pressure and velocity parameters different in general.

These equations are completed with Newmark's formula to relate the displacement field (defined only at the vessel wall-fluid boundary interface Γ_s) with the velocity and acceleration fields:

$$\vec{u}_{n+1} = \vec{u}_n + \Delta t \vec{v}_n + \frac{\Delta t^2}{2} \left\{ (1 - 2\beta) \vec{v}_{,t_n} + 2\beta \vec{v}_{,t_{n+1}} \right\} \tag{3.83}$$

and the corresponding interpolation formula for $\vec{u}_{n+\alpha_{f_v}}$

$$\vec{u}_{n+\alpha_{f_v}} = \vec{u}_n + \alpha_{f_v} \left(\vec{u}_{n+1} - \vec{u}_n \right) \tag{3.84}$$

For the examples presented in Chapter 5, we have adopted $\beta = 1$. A careful analysis of the influence of this parameter on the linear stability of the solution can be performed using methods described in [65]. We now provide the expression of the linearized Left-Hand-Side matrices. The terms that we have chosen to include are essentially formed from the "frozen coefficient" assumption while differentiating the equations:

$$
\begin{aligned}
K_{ij}^{ab} &= \frac{\partial \left(R_i\right)_m^a}{\partial \left(v_{j,t}\right)_{n+1}^b} = \frac{\partial \left(R_i\right)_m^a}{\partial \left(v_{j,t}\right)_{n+\alpha_m}^b} \alpha_{m_v} + \frac{\partial \left(R_i\right)_m^a}{\partial \left(v_j\right)_{n+\alpha_f}^b} \alpha_{f_v} \Delta t \gamma_v + \frac{\partial \left(R_i\right)_m^a}{\partial \left(u_j\right)_{n+\alpha_f}^b} \alpha_{f_v} \Delta t^2 \beta = \\
&\alpha_{m_v} \delta_{ij} \left[\int_{\bar{\Omega}_e} \rho N^a N^b d\vec{x} + \zeta \int_{\bar{\Gamma}_{s_e}} \rho^s N^a N^b ds \right] + \\
&\alpha_{f_v} \Delta t \gamma_v \delta_{ij} \int_{\bar{\Omega}_e} \left[N^a \rho \left(v_k - \frac{\tau_M}{\rho} \mathcal{L}_k \right) N_{,k}^b \right] dx + \\
&\alpha_{f_v} \Delta t \gamma_v \delta_{ij} \int_{\bar{\Omega}_e} \left[N_{,k}^a \left(\mu N_{,k}^b + v_k \tau_M \rho v_m N_{,m}^b + \mathcal{L}_k \bar{\tau} \mathcal{L}_m N_{,m}^b \right) \right] dx + \\
&\alpha_{f_v} \Delta t \gamma_v \int_{\bar{\Omega}_e} \left[N_{(i),(i)}^a \tau_C N_{(j),(j)}^b + N_{(i),(j)}^a \mu N_{(j),(i)}^b \right] dx + \\
&\alpha_{f_v} \Delta t^2 \beta \zeta \vec{e}_i^T \int_{\bar{\Gamma}_{s_e}} \left[\underset{\sim}{B}^T \underset{\sim}{D} \underset{\sim}{B} \right] ds \cdot \vec{e}_j
\end{aligned}
\tag{3.85}
$$

$$
\begin{aligned}
G_i^{ab} &= \frac{\partial \left(R_i\right)_m^a}{\partial \left(p_{,t}\right)_{n+1}^b} = \frac{\partial \left(R_i\right)_m^a}{\partial p_{n+\alpha_f}^b} \alpha_{f_p} \Delta t \gamma_p = \\
&- \alpha_{f_p} \Delta t \gamma_p \int_{\bar{\Omega}_e} N_{(i),(i)}^a N^b d\vec{x} = -\Delta t \int_{\bar{\Omega}_e} N_{(i),(i)}^a N^b d\vec{x}
\end{aligned}
\tag{3.86}
$$

$$
\begin{aligned}
D_j^{ab} &= \frac{\partial \left(R_c^{ALHS}\right)^a}{\partial \left(v_{j,t}\right)_{n+1}^b} = \frac{\partial \left(R_c^{ALHS}\right)^a}{\partial \left(v_j\right)_{n+\alpha_f}^b} \alpha_{f_v} \Delta t \gamma_v = \\
&\alpha_{f_v} \Delta t \gamma_v \int_{\bar{\Omega}_e} N^a N_{(j),(j)}^b d\vec{x}
\end{aligned}
\tag{3.87}
$$

$$
\begin{aligned}
C^{ab} &= \frac{\partial \left(R_c^{ALHS}\right)^a}{\partial \left(p_{,t}\right)_{n+1}^b} = \frac{\partial \left(R_c^{ALHS}\right)^a}{\partial p_{n+\alpha_f}^b} \alpha_{f_p} \Delta t \gamma_p = \\
&\alpha_{f_p} \Delta t \gamma_p \int_{\bar{\Omega}_e} N_{,i}^a \frac{\tau_M}{\rho} N_{,i}^b d\vec{x} = \Delta t \int_{\bar{\Omega}_e} N_{,i}^a \frac{\tau_M}{\rho} N_{,i}^b d\vec{x}
\end{aligned}
\tag{3.88}
$$

In the previous expressions, N^a and N^b refer to the shape functions of local nodes a and b, respectively, whereas $\vec{e}_i$ represents the ith Euclidean basis vector for $\Re^{n_{sd}}$. Indices between parentheses indicate that no summation over the index is carried out.

The matrices G_i^{ab} and D_j^{ab} are not anti-symmetric (see equations (3.86) and (3.87)), since the generalized-α method parameters for velocity and pressure are different. To make these matrices anti-symmetric, we can multiply G_i^{ab} (and C^{ab}) by the factor $\alpha_{f_v}\gamma_v$ and divide $\left(\Delta p_{,t}\right)_{n+1}^{b}$ by the same factor, viz.

$$\begin{bmatrix} K_{ij}^{ab} & \alpha_{f_v}\gamma_v G_i^{ab} \\ D_j^{ab} & \alpha_{f_v}\gamma_v C^{ab} \end{bmatrix} \begin{Bmatrix} \left(\Delta v_{j,t}\right)_{n+1}^{b} \\ \left(\Delta p_{,t}\right)_{n+1}^{b} \Big/ \left(\alpha_{f_v}\gamma_v\right) \end{Bmatrix} = -\begin{Bmatrix} \left(R_i\right)_m^a \\ R_c^a \end{Bmatrix} \tag{3.89}$$

We can also write this system as:

$$\begin{bmatrix} K_{ij}^{ab} & -D_i^{ba} \\ D_j^{ab} & \widehat{C}^{ab} \end{bmatrix} \begin{Bmatrix} \left(\Delta v_{j,t}\right)_{n+1}^{b} \\ \left(\Delta p_{,t}\right)_{n+1}^{b} \end{Bmatrix} = -\begin{Bmatrix} \left(R_i\right)_m^a \\ R_c^a \end{Bmatrix} \tag{3.90}$$

or, alternatively as:

$$\begin{bmatrix} K_{ij}^{ab} & G_i^{ab} \\ -G_j^{ba} & \widehat{C}^{ab} \end{bmatrix} \begin{Bmatrix} \left(\Delta v_{j,t}\right)_{n+1}^{b} \\ \left(\Delta p_{,t}\right)_{n+1}^{b} \end{Bmatrix} = -\begin{Bmatrix} \left(R_i\right)_m^a \\ R_c^a \end{Bmatrix} \tag{3.91}$$

where

$$\left(\Delta p_{,t}\right)_{n+1}^{b} = \frac{\left(\Delta p_{,t}\right)_{n+1}^{b}}{\alpha_{f_v}\gamma_v} \qquad , \qquad \widehat{C}^{ab} = \alpha_{f_v}\gamma_v C^{ab} \tag{3.92}$$

We now provide the expressions of the different parts of the time stepping and nonlinear iteration loops as seen in Figure 3-4 for the CMM-FSI.

Predictor Phase

$$p_{n+1}^{(0)} = p_n \qquad , \qquad \left(p_{,t}\right)_{n+1}^{(0)} = \frac{\gamma_p - 1}{\gamma_p}\left(p_{,t}\right)_n = 0 \tag{3.93}$$

$$\vec{v}_{n+1}^{(0)} = \vec{v}_n \qquad , \qquad \vec{v}_{,t_{n+1}}^{(0)} = \frac{\gamma_v - 1}{\gamma_v}\vec{v}_{,t_n} \tag{3.94}$$

$$\vec{u}_{n+1}^{(0)} = \vec{u}_n + \Delta t\vec{v}_n + \frac{\Delta t^2}{2}\frac{\gamma_v - 2\beta}{\gamma_v}\vec{v}_{,t_n} \tag{3.95}$$

Multi-corrector Phase

$$p_{n+\alpha_{f_p}}^{(i)} = p_n + \alpha_{f_p}\left(p_{n+1}^{(i-1)} - p_n\right) \quad \Rightarrow \quad p_{n+1}^{(i)} = p_{n+1}^{(i-1)} = p_n \tag{3.96}$$

$$\left(p_{,t}\right)_{n+\alpha_{m_p}}^{(i)} = \left(p_{,t}\right)_n + \alpha_{m_p}\left(\left(p_{,t}\right)_{n+1}^{(i-1)} - \left(p_{,t}\right)_n\right) \quad \Rightarrow \quad \left(p_{,t}\right)_{n+1}^{(i)} = \left(p_{,t}\right)_{n+1}^{(i-1)} = 0 \tag{3.97}$$

$$\vec{v}_{n+\alpha_{f_v}}^{(i)} = \vec{v}_n + \alpha_{f_v}\left(\vec{v}_{n+1}^{(i-1)} - \vec{v}_n\right) \tag{3.98}$$

$$\vec{v}_{,t_{n+\alpha_{m_v}}}^{(i)} = \vec{v}_{,t_n} + \alpha_{m_v}\left(\vec{v}_{,t_{n+1}}^{(i-1)} - \vec{v}_{,t_n}\right) \tag{3.99}$$

$$\vec{u}_{n+\alpha_{f_v}}^{(i)} = \vec{u}_n + \alpha_{f_v}\left(\vec{u}_{n+1}^{(i-1)} - \vec{u}_n\right) \tag{3.100}$$

Residual Evaluation/Linear Solve

$$\vec{R}^{(i)}(\vec{u}^{(i)}_{n+\alpha_{f_v}}, \vec{v}^{(i)}_{n+\alpha_{f_v}}, \vec{v}^{(i)}_{,t_{n+\alpha_{m_v}}}, p^{(i)}_{n+\alpha_{fp}}) = \vec{R}^{(i)}(\vec{u}^{(i)}_{n+\alpha_{f_v}}, \vec{v}^{(i)}_{n+\alpha_{f_v}}, \vec{v}^{(i)}_{,t_{n+\alpha_{m_v}}}, p^{(i)}_{n+1}) = \vec{0} \quad (3.101)$$

$$\begin{bmatrix} K_{ij}^{ab} & G_i^{ab} \\ -G_j^{ba} & \widehat{C}^{ab} \end{bmatrix} \begin{Bmatrix} \left(\Delta v_{j,t}\right)_{n+1}^{b} \\ \left(\Delta p_{,t}\right)_{n+1}^{b} \end{Bmatrix} = - \begin{Bmatrix} \left(R_i\right)_m^a \\ R_c^a \end{Bmatrix} \quad (3.102)$$

This linear system is solved with the AcuSolve© [67] iterative solver, which features a GMRES solver for the velocity equation and a Conjugate Gradient solver for the pressure equation.

Update Phase

$$\vec{v}^{(i+1)}_{,t_{n+1}} = \vec{v}^{(i)}_{,t_{n+1}} + \Delta\vec{v}^{(i)}_{,t_{n+1}} \quad (3.103)$$

$$\vec{v}^{(i+1)}_{n+1} = \vec{v}^{(i)}_{n+1} + \Delta t \gamma_v \Delta\vec{v}^{(i)}_{,t_{n+1}} \quad (3.104)$$

$$\vec{u}^{(i+1)}_{n+1} = \vec{u}^{(i)}_{n+1} + \Delta t^2 \beta \Delta\vec{v}^{(i)}_{,t_{n+1}} \quad (3.105)$$

$$p^{(i+1)}_{,t_{n+1}} = p^{(i)}_{,t_{n+1}} + \Delta p^{(i)}_{,t_{n+1}} = p^{(i)}_{,t_{n+1}} + \alpha_{f_v} \gamma_v \Delta p^{(i)}_{,t_{n+1}} \quad (3.106)$$

$$p^{(i+1)}_{n+1} = p^{(i)}_{n+1} + \Delta t \gamma_p \Delta p^{(i)}_{,t_{n+1}} = p^{(i)}_{n+1} + \Delta t \alpha_{f_v} \gamma_v \Delta p^{(i)}_{,t_{n+1}} \quad (3.107)$$

3.4.4 Summary of the CMM-FSI Additions to the LHS Matrices and RHS Vectors of Rigid Wall Formulations

To finalize the description of the CMM-FSI method, we present the list of additions to the left-hand-side matrices and right-hand-side vectors presented in equations (3.65) with respect to those present in rigid wall formulations:

Right-hand-side vectors:

$$\vec{R}_m = \vec{R}_m^{rigid} + \boxed{\zeta \int_{\Gamma_s} \left\{ \vec{w} \cdot \rho^s \vec{v}_{,t} + \nabla \vec{w} : \underset{\sim}{\sigma}^s \left(\vec{u} \right) \right\} ds - \zeta \int_{\partial \Gamma_h} \vec{w} \cdot \vec{h}^s dl} \tag{3.108}$$

$$R_c = R_c^{rigid} + \boxed{\int_{\Gamma_s} q v_n ds} \tag{3.109}$$

Left-hand-side matrices:

$$K_{ij}^{ab} = \left(K_{ij}^{ab} \right)^{rigid} + \boxed{\alpha_m \delta_{ij} \zeta \int_{\bar{\Gamma}_{s_e}} \rho^s N^a N^b ds + \alpha_f \beta \Delta t^2 \zeta \vec{e}_i^T \int_{\bar{\Gamma}_{s_e}} \left[\underset{\sim}{B}^T \underset{\sim}{D} \underset{\sim}{B} \right] ds \cdot \vec{e}_j} \tag{3.110}$$

$$G_i^{ab} = \left(G_i^{ab} \right)^{rigid} \tag{3.111}$$

$$D_j^{ab} = \left(D_j^{ab} \right)^{rigid} \tag{3.112}$$

$$C^{ab} = \left(C^{ab} \right)^{rigid} \tag{3.113}$$

As previously stated, the additional terms of the CMM-FSI method shown in equations (3.108)-(3.110) represent relatively minor changes to standard finite element formulations for solving the incompressible Navier-Stokes equations.

3.5 Initialization of the Algorithm

We conclude the description of the CMM-FSI by providing a few remarks on initialization of the different field variables.

For a rigid wall problem, only the velocity field requires initial conditions. However, for a deformable wall problem, initial values for the displacement and velocity fields at the fluid-solid interface are needed as well, as given by equation (3.23). It is important for the stability of the solution that the fluid-solid system departs from an initial state representing equilibrium. To accomplish this, the wall velocity is initially set to zero. As for the wall displacement field $\vec{u}^0(\vec{x})$, it is assigned such that its associated stress state $\vec{t}^s$ is in equilibrium with the fluid traction $\vec{t}^f$, as described by equation (3.26). This condition is prescribed using the following algorithm:

1. A (steady) rigid wall problem is solved first, using the same inlet and outlet boundary conditions as for the deformable wall problem. The velocity $\vec{v}^0(\vec{x})$ and pressure $p^0(\vec{x})$ fields obtained are then used as *initial conditions* for the deformable wall problem.

2. The vessel wall is loaded with a body force $\vec{b}^s$ normal to the wall with a magnitude obtained from the average value $\mathcal{P}$ of the rigid wall pressure field $p^0(\vec{x})$:

$$\vec{b}^s = \frac{\mathcal{P}\vec{n}}{\zeta} \tag{3.114}$$

This body force represents the exact load for the vessel wall in a hydrostatic case. This can be proven by particularizing the expression of the weak form of the CMM-FSI defined by equation (3.34) for a hydrostatic case (viz, $\vec{v} = \vec{v}_{,t} = \vec{0}$, $\underset{\sim}{\tau} = \underset{\sim}{0}$), considering that no body forces and external tractions act on the system. Under these assumptions, and using the divergence theorem, equation (3.34) reduces to:

$$\zeta \int_{\Gamma_s} \nabla \vec{w} : \underset{\sim}{\sigma}^s(\vec{u})\, ds = \int_{\Gamma_s} \vec{w}\mathcal{P} \cdot \vec{n}\, d\vec{x} \tag{3.115}$$

This equation shows that the stresses of the vessel wall $\underset{\sim}{\sigma}^s(\vec{u})$ balance the traction at the fluid-solid interface and provide the condition to find the initial displacement field $\vec{u}^0(\vec{x})$.

Once the values for $\vec{v}^0(\vec{x})$, $p^0(\vec{x})$ and $\vec{u}^0(\vec{x})$ have been obtained, the deformable wall problem is run under the same steady flow conditions used for the rigid wall initialization until the solution is sufficiently converged (typically, with residuals on the order of 10^{-5}) and then the pulsatile simulation is started.

3.6 Consistent Calculation of Boundary Fluxes

Traditionally, the boundary fluxes like the wall traction or wall shear stresses are evaluated by substituting the computed flow quantities and their derivatives into the definition of these fluxes. Thus, for the total wall traction, we would simply insert the computed velocity and pressure fields into the equation

$$\vec{t}_{\vec{n}} = \underset{\sim}{\sigma}\vec{n} = \left[-p\underset{\sim}{I} + \underset{\sim}{\tau}\right]\vec{n} \tag{3.116}$$

whereas for the wall shear stress we use the in-plane component of the viscous stress traction given by the equation:

$$\vec{\tau}_{\vec{n}} = \underset{\sim}{\tau}\vec{n} = \mu\left(\nabla\vec{v} + (\nabla\vec{v})^T\right)\vec{n} \tag{3.117}$$

Although this classical method may provide adequate results, it does not utilize all the information available in the variational form of the problem. It is possible to use the variational form and obtain a so-called *variationally consistent* boundary flux, as seen in [65] and [62]. In the references, a simple method to obtain these variationally consistent fluxes is described for the case of rigid wall flows, where the velocity on the lateral boundary of the fluid domain (which is part of the Γ_g boundary) is zero. A new space of weighting functions $\vec{W}_h^k$ is introduced such that

$$\vec{W}_h^k = \left\{\hat{\vec{w}} \middle| \hat{\vec{w}}(\cdot,t) \in H^1(\Omega)^{n_{sd}}, t \in [0,T], \hat{\vec{w}}\Big|_{\vec{x}\in\bar{\Gamma}_{g_e}} \in P_k(\bar{\Gamma}_{g_e})^{n_{sd}}\right\} \tag{3.118}$$

Note that $\vec{\mathcal{W}}_h^k$ defines a space of test functions $\hat{\vec{w}}$ that are different from zero only on Γ_g, where the wall shear stress is to be reconstructed. The variational form of the problem is re-written using this new weighting space and the known pressure, p and velocity, $\vec{v}$.

In the case of a deformable wall formulation, we have a space of non-zero functions defined exclusively on the lateral fluid boundary Γ_s: this space is basically the vessel wall weighting functional space given by equation (3.29). Therefore, we can write the CMM-FSI variational form using this space as:

Given $\vec{v} \in \vec{\mathcal{S}}_h^k$, $p, q \in \mathcal{P}_h^k$ and $\vec{w} \in \vec{\mathcal{W}}_h^{sk}$, find $\vec{t}^f \in \vec{\mathcal{W}}_h^{sk}$ such that

$$
\begin{aligned}
B(\vec{w}, q; \vec{v}, p) = {} & \int_\Omega \left\{ \vec{w} \cdot \left(\rho \vec{v}_{,t} + \rho \vec{v} \cdot \nabla \vec{v} - \vec{f} \right) + \nabla \vec{w} : \left(-p \underset{\sim}{I} + \underset{\sim}{\tau} \right) - \nabla q \cdot \vec{v} \right\} d\vec{x} \\
& + \int_{\Gamma_h} \left\{ -\vec{w} \cdot \vec{h} + q v_n \right\} ds + \int_{\Gamma_s} \left\{ -\vec{w} \cdot \vec{t}^f + q v_n \right\} ds + \int_{\Gamma_g} q v_n ds \\
& + \sum_{e=1}^{n_{el}} \int_{\bar{\Omega}_e} \left\{ (\vec{v} \cdot \nabla) \vec{w} \cdot \tau_M \vec{\mathcal{L}}(\vec{v}, p) + \nabla \cdot \vec{w} \tau_C \nabla \cdot \vec{v} \right\} d\vec{x} \\
& + \sum_{e=1}^{n_{el}} \int_{\bar{\Omega}_e} \left\{ \vec{w} \cdot \left(\rho \overset{\Delta}{\vec{v}} \cdot \nabla \vec{v} \right) + \left(\vec{\mathcal{L}}(\vec{v}, p) \cdot \nabla \vec{w} \right) \left(\bar{\tau} \vec{\mathcal{L}}(\vec{v}, p) \cdot \vec{v} \right) \right\} d\vec{x} \\
& + \sum_{e=1}^{n_{el}} \int_{\bar{\Omega}_e} \nabla q \cdot \frac{\tau_M}{\rho} \vec{\mathcal{L}}(\vec{v}, p) d\vec{x} = 0
\end{aligned}
\tag{3.119}
$$

This equation is of the same form as equation (3.34), with the wall traction $\vec{t}^f$ replacing the vessel wall terms as given by equation (3.32), which gives the vessel wall traction as a function of wall stiffness, mass, and boundary conditions. In equation (3.119), the only unknown term is the one containing the wall traction $\vec{t}^f$. Therefore, the equation can be re-written as follows:

$$\begin{aligned}\int_{\Gamma_s} \vec{w} \cdot \vec{t}^{\,f} ds = {} & \int_{\Omega} \left\{ \vec{w} \cdot \left(\rho \vec{v}_{,t} + \rho \vec{v} \cdot \nabla \vec{v} - \vec{f} \right) + \nabla \vec{w} \colon \left(-p \underset{\sim}{I} + \underset{\sim}{\tau} \right) - \nabla q \cdot \vec{v} \right\} d\vec{x} \\ & + \int_{\Gamma_h} \left\{ -\vec{w} \cdot \vec{h} + q v_n \right\} ds + \int_{\Gamma_s} q v_n ds + \int_{\Gamma_g} q v_n ds \\ & + \sum_{e=1}^{n_{el}} \int_{\bar{\Omega}_e} \left\{ \left(\vec{v} \cdot \nabla \right) \vec{w} \cdot \tau_M \vec{\mathcal{L}} \left(\vec{v}, p \right) + \nabla \cdot \vec{w} \tau_C \nabla \cdot \vec{v} \right\} d\vec{x} \\ & + \sum_{e=1}^{n_{el}} \int_{\bar{\Omega}_e} \left\{ \vec{w} \cdot \left(\rho \overset{\Delta}{\vec{v}} \cdot \nabla \vec{v} \right) + \left(\vec{\mathcal{L}} \left(\vec{v}, p \right) \cdot \nabla \vec{w} \right) \left(\bar{\tau} \vec{\mathcal{L}} \left(\vec{v}, p \right) \cdot \vec{v} \right) \right\} d\vec{x} \\ & + \sum_{e=1}^{n_{el}} \int_{\bar{\Omega}_e} \nabla q \cdot \frac{\tau_M}{\rho} \vec{\mathcal{L}} \left(\vec{v}, p \right) d\vec{x} \end{aligned} \tag{3.120}$$

The solution to equation (3.120), using the functional spaces defined previously provides the variationally consistent total traction $\vec{t}^{\,f}$. With this, the shear stress vector is obtained by subtracting the normal traction, viz:

$$\vec{\tau}_{\vec{n}} = \vec{t}^{\,f} - \left(\vec{t}^{\,f} \cdot \vec{n} \right) \vec{n} \tag{3.121}$$

Chapter 4

Chapter 4. Verification of the Method

4.1 Introduction

Verification and Validation (V&V) in computational science and engineering is the subject that deals with evaluating the reliability and accuracy of the results provided by computer models of physical processes [71]. More specifically, *Verification* is the science that addresses the quality of the numerical treatment of some mathematical model. This involves two different components:

- Code verification: the process of determining if a code faithfully implements a computational model.
- Solution verification: this is concerned with the numerical accuracy with which the mathematical model is approximated by the computer model.

On the other hand, *validation* of a computational model involves the comparison of the results predicted by the model with those observed in the physical world. It follows then that when developing a computational model, verification should precede validation as a necessary step to address the reliability of the model. Once this reliability is verified, the code can be *validated* by solving real-world problems, and comparing the quality of the solutions provided by it with experimental measurements.

In this chapter, we address the verification of the CMM-FSI as a computational model of Womersley's deformable wall mathematical model.

4.2 CMM-FSI as a Computational Model of Womersley's Analytical Solution for Pulsatile Flow in a Cylindrical Deformable Vessel

Choosing the parameters defining Womersley's deformable analytical solution is a task that must be performed carefully. On the one hand, we must choose the set of parameters such that the main approximation of the theory (i.e., the long wave assumption) holds in the numerical solution as well. This implies:

$$\frac{R}{L}, \frac{\bar{w}}{c} \ll 1 \tag{4.1}$$

On the other hand, we would like to minimize the computational cost of the numerical solution, by keeping the length of the vessel as small as possible.

For clarity, we consider just one single frequency ω in the oscillatory part of the analytical solution. We proceed now to describe the set of values that define this solution:

- We first choose the radius, wall thickness, Young's modulus and Poisson's ratio corresponding to the common carotid artery. We have: $R = 0.3$ cm, $h = 0.03$ cm, $E = 2 \cdot 10^6$ dyn/cm^2 and $\sigma = 0.5$. We consider a value of $\mu = 0.04$ poise for the kinematic viscosity of the blood. The densities of the blood and the wall are both set to 1.

- Inviscid wave speed. Given the material parameters presented above, the inviscid wave speed is given by the Moens-Korteweg equation:

$$c_0 = \sqrt{\frac{Eh}{2\rho R}} = 316.2278 \text{ cm/s} \tag{4.2}$$

- Period of the oscillatory component of the solution: $T = \pi/2$ s. This generates an angular frequency of $\omega = 4$ rad/s and a Womersley number of $\alpha = 3$, which is in the moderate range for human arterial flows.
- Input steady pressure gradient ($k_s = -53.33$ dyn/cm^3).
- Input oscillatory pressure gradient ($k_\phi = A = -50.0$ dyn/cm^3). Considering this, the resulting input pressure gradient is shown in Figure 4-1.
- The inlet pressure gradient depicted in Figure 4-1 is the boundary condition prescribed to obtain the analytical solution, which is defined in a *semi-infinite* domain (from z=0 to z=∞). With the inputs specified above, we can obtain the basic parameters governing the analytical solution:
    - Complex wave speed $c = 270.68 + 67.45i$ cm/s
    - Input oscillatory pressure amplitude $H = 842.82 - 3{,}383.5i$ dyn/cm^2
    - Characteristic length of the vessel (it represents a complete spatial wave for the frequency ω considered above) $L = c_R \cdot T = 451.6\,\text{cm}$

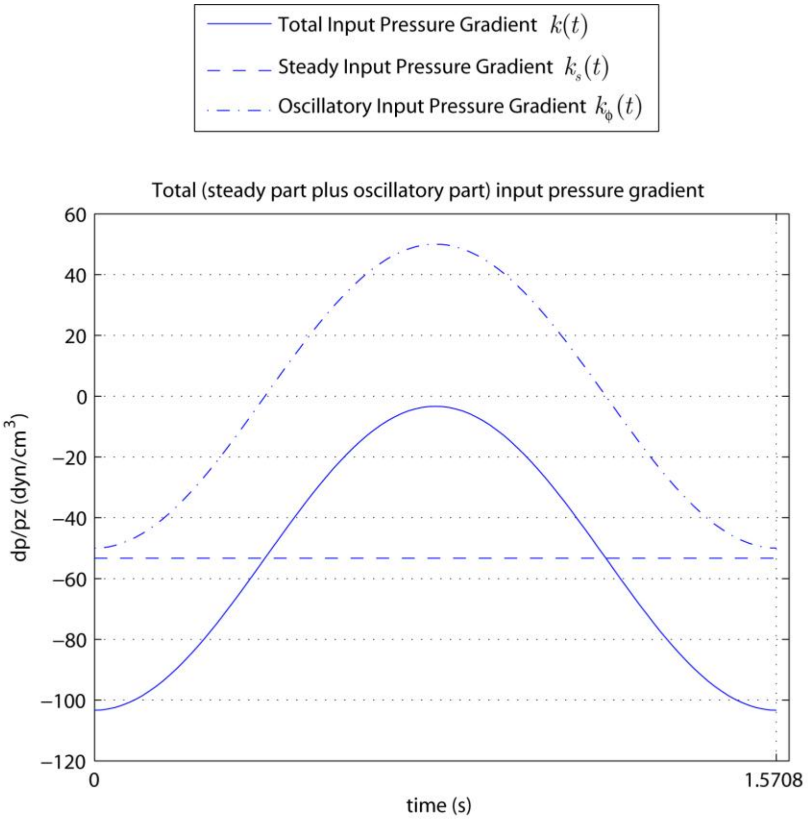

Figure 4-1: Total input pressure gradient over the cardiac cycle.

We proceed to provide the plots of the velocity and pressure solutions obtained with the parameters given above, for a vessel of length $L = 451.6$ cm.

Figure 4-2 shows the longitudinal velocity profiles along the length of the vessel, at different times of the cardiac cycle. We can observe the periodicity of the solution in space (with period L) and time (with period T). In both cases, the frequency of the oscillation is given by ω.

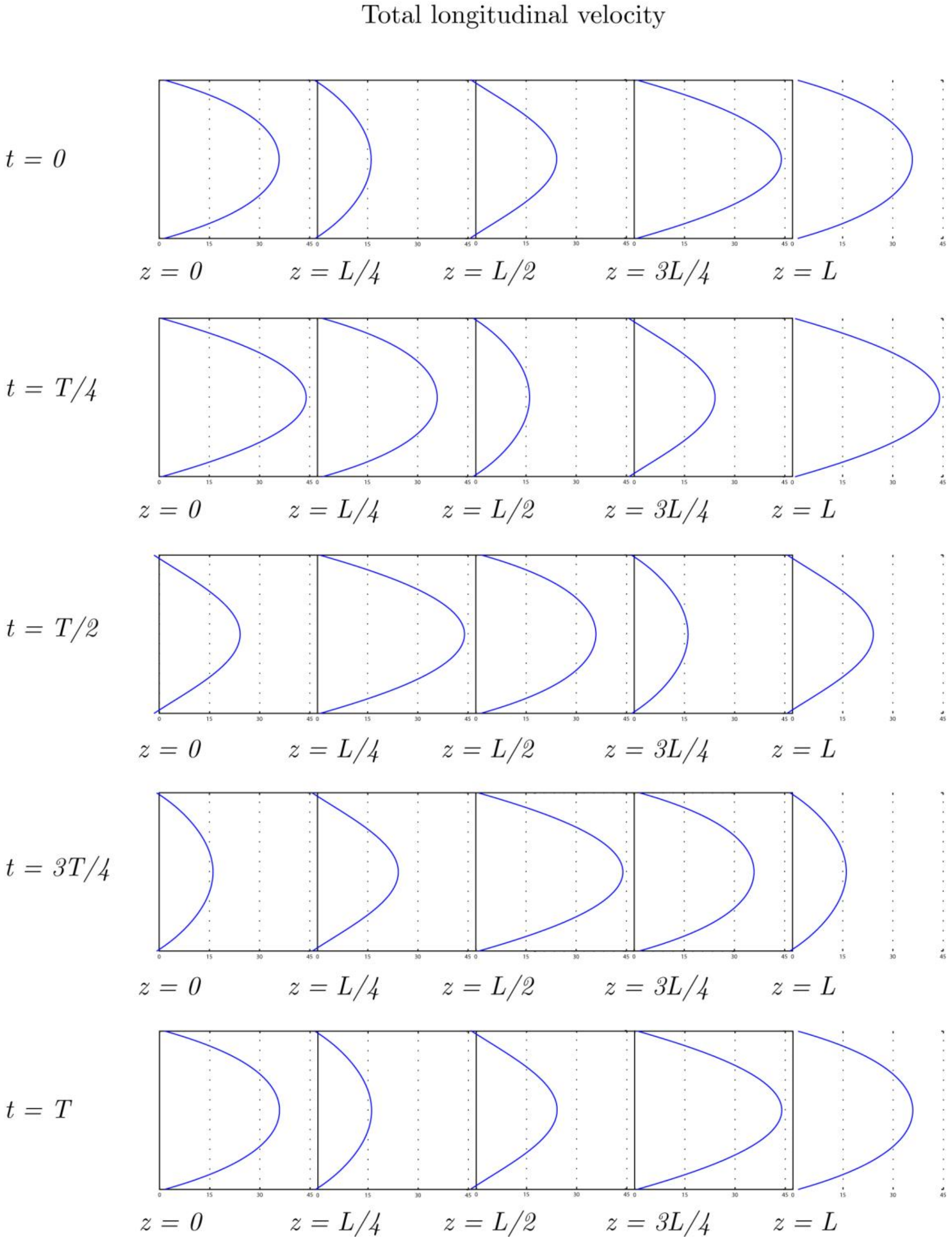

Figure 4-2: Longitudinal velocity profiles showing the periodicity of the velocity waves in space and time.

Figure 4-3 shows the radial velocity profiles at the vessel wall (r=R), along the length of the vessel, at different times of the cardiac cycle. The same periodic behavior in space and time is observed as well. Note that the maximum magnitude of the radial component of the wall velocity (0.02 cm/s) is much smaller than its longitudinal counterpart (on the order of 1.75 cm/s, as we will see later).

As for the pressure solution, Figure 4-4 represents the time evolution of the total pressure at different sections along the length of the vessel (considering a mean inlet pressure of 100 mmHg = 133,333 dyn/cm^2). We can observe that the pressure field is also periodic in time, and the oscillatory component of the pressure shows the same phase at z=0 and z=L. Furthermore, the total mean pressure decreases for larger values of z, according to the prescribed input steady pressure gradient.

Figure 4-5 shows the pressure variation along the length of the vessel at different points of the cardiac cycle (t=0, $T/4$, $T/2$ and $3T/4$). We again observe the linear variation of the steady component of the pressure, as well as the changes in phase of the oscillatory component over the cycle.

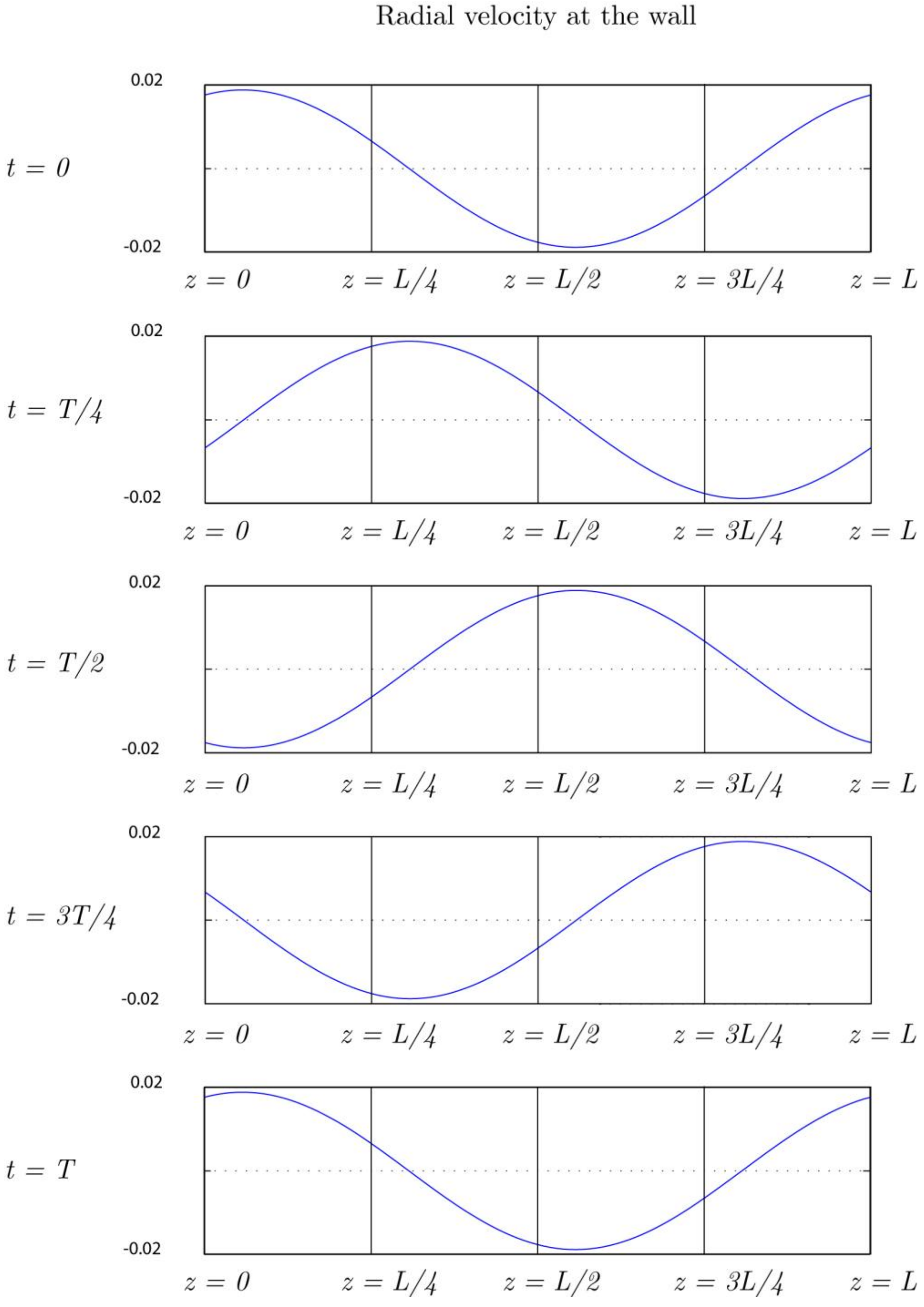

Figure 4-3: Radial velocity profiles at the vessel wall (r=R).

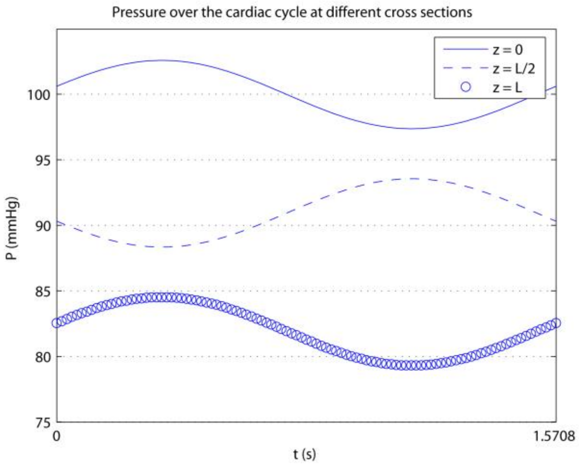

Figure 4-4: Total pressure at different cross sections of the vessel as a function of time.

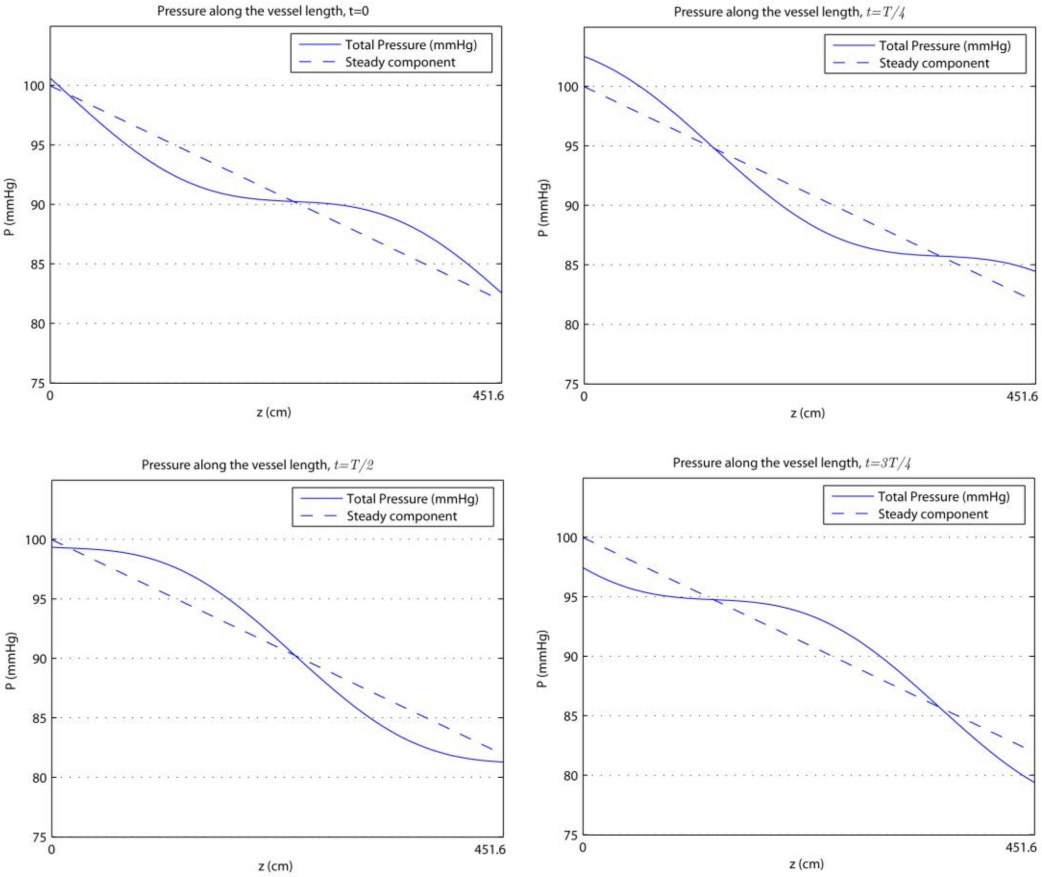

Figure 4-5: Total pressure along the length of the vessel at different points of the cardiac cycle.

4.2.1 Boundary Conditions for the Numerical Solution

When comparing the results obtained with the CMM-FSI formulation and Womersley's elastic wall solution, one must put considerable care into the specification of the boundary conditions for the numerical test, since by definition the numerical domain is of *finite* length, and the analytical solution is defined in a *semi-infinite* domain. Furthermore, and as pointed out before, one wants to minimize the length of the numerical domain, since it will directly impact the cost of the simulation. Therefore, we have adopted a vessel much shorter than the one given by the characteristic spatial wavelength $L \simeq 452$ cm. The considered length of the vessel for the numerical domain is $l = 4$ cm.

The most delicate point is the specification of the outflow boundary condition ($z = l$). We need to replicate the behavior of the waves traveling forward in the semi-infinite analytical domain, without experiencing any reflections. To accomplish this, we prescribe the analytical expression of the flow impedance function $Z(t)$ (see [24,72]) for the lumen nodes, and the velocity vectors (with both radial and longitudinal components) for the wall nodes. For the inlet condition ($z = 0$), we prescribed the three components of the velocity vectors given by equations (2.133)-(2.134). Figure 4-6 shows schematically the set of boundary conditions applied to the numerical domain:

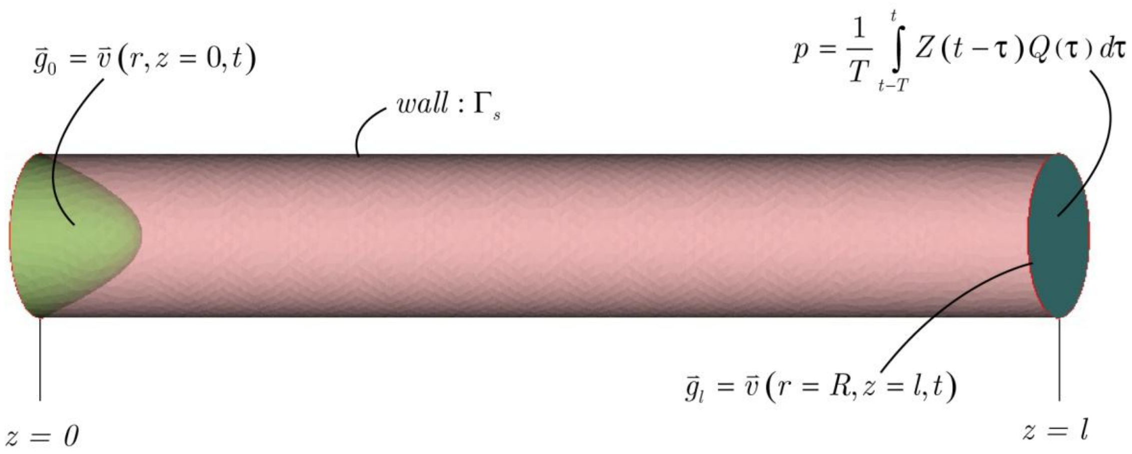

Figure 4-6: Inlet and outflow boundary conditions prescribed in the numerical domain.

The outlet impedance function $Z(t)$ is obtained as follows:

- First, we obtain the outlet total pressure $p(t)$.
- Second, we derive the expression for the flow at the outlet face. This expression is given by

$$Q(t)_{|z=l} = \int_{r=0}^{r=R} 2\pi r w(r, z = l, t) = -\frac{k_s \pi R^4}{8\mu} + \frac{H\pi R^2}{\rho c}[1 - Mg]e^{i\omega\left(t-\frac{l}{c}\right)} \tag{4.3}$$

where g is given by equation (2.109). The pressure and flow rate waves at $z=l$ are depicted in Figure 4-7. As can be observed, these two waves are not in phase: the pressure lags the flow wave, as often observed physiologically.

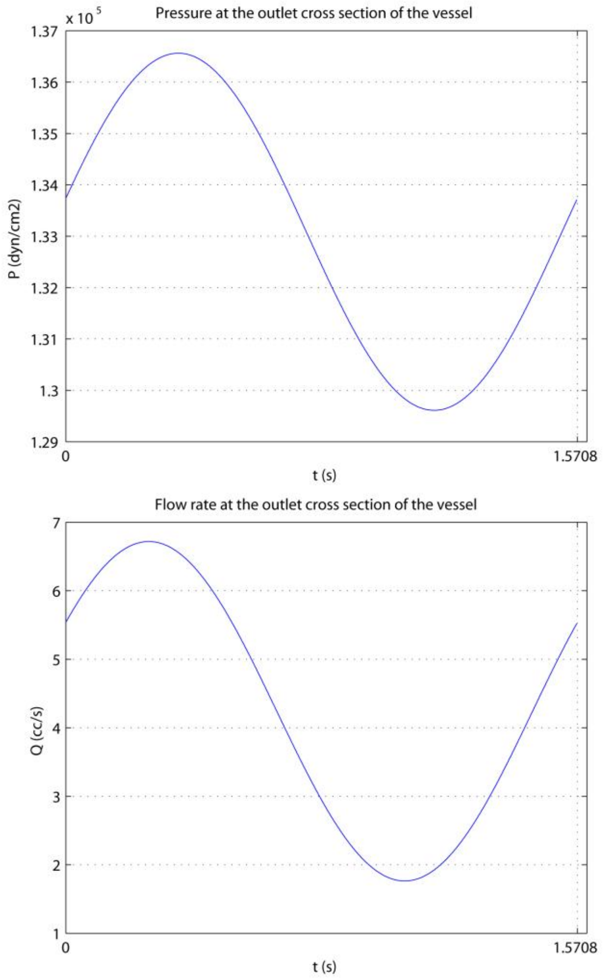

Figure 4-7: Pressure and flow waves at $z = l$.

- We then proceed to obtain the Fourier decomposition of the pressure and flow waves: p_k and Q_k.
- The impedance function can be obtained in the Fourier domain as the ratio of the pressure and flow modes for each frequency:

$$Z_k = \frac{p_k}{Q_k}, \quad \text{k=0,1,...} \tag{4.4}$$

- In this problem, the pressure and flow (and therefore the impedance) waves only have two modes (corresponding to the steady state mode and to the frequency ω). Therefore, we have to truncate the modes of the impedance for $k>2$, since Q_k is zero and therefore equation (4.4) is not defined. The Fourier decomposition of the pressure, flow and impedance can be seen in Figure 4-8.
- The impedance function in the time domain can then be obtained via the inverse Fourier transform of the impedance modes in the frequency domain Z_k (see Figure 4-9).

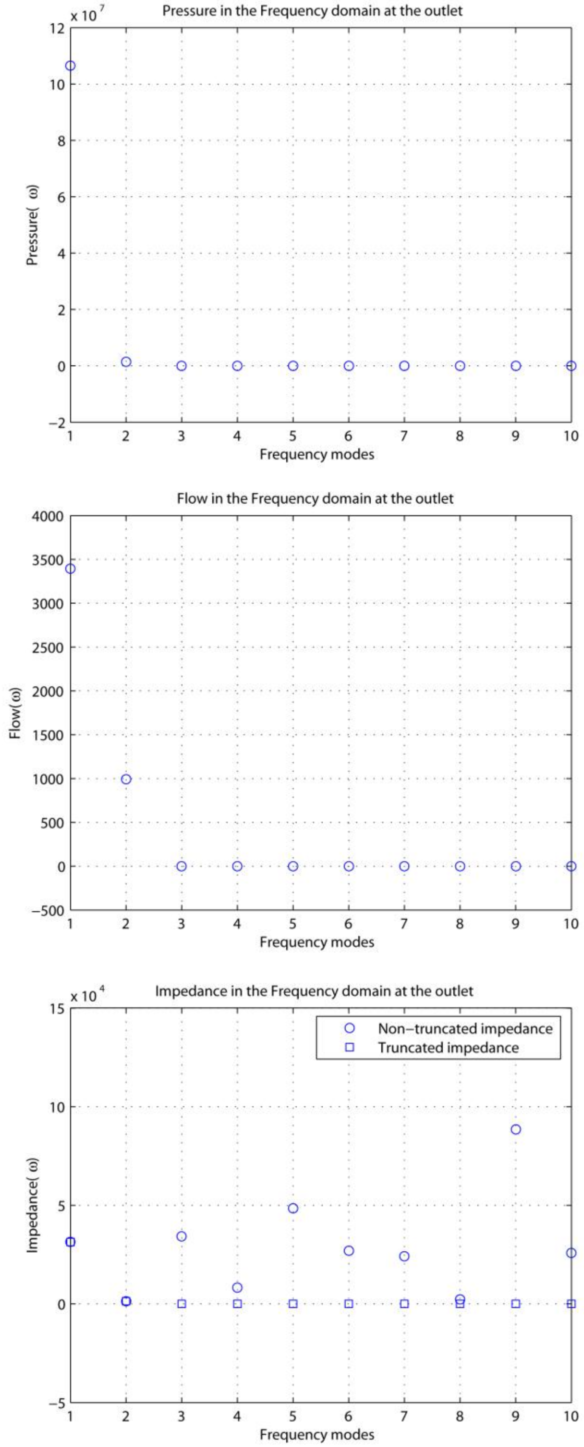

Figure 4-8: Fourier modes of pressure, flow and impedance at $z = l$.

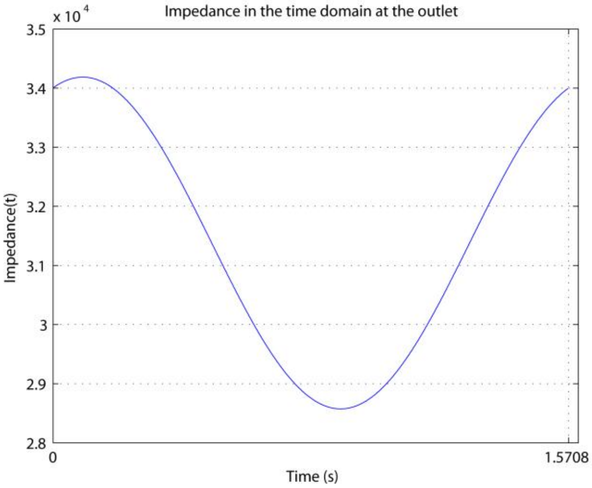

Figure 4-9: Impedance function at the end of the numerical domain ($z = l$).

4.2.2 Initial Conditions for the Numerical Solution

Initial conditions for the numerical analysis must be set with the same care used for the boundary condition specification in order to minimize the impact of initial transients in the system due to lack of equilibrium in the solid-fluid interface. This is particularly important when the wall is represented as an elastic solid, since in this case there is minimal physical dissipation in the system. To initialize the problem, we follow the steps sketched in Section 3.5:

1. Steady analysis with rigid walls. This step provides the steady pressure distribution.

2. Obtain the deformation of the structure under the steady pressure distribution. With this information, we compute the initial values for the wall stress/displacement fields.
3. Steady analysis with deformable walls.
4. Pulsatile analysis with deformable walls.

In order to eliminate transients in the numerical solution, we have prescribed the initial flow, pressure and wall inlet/outlet ring velocities at a physical time t such that the velocities of the inlet and outlet wall rings are as close to zero as possible. The reason for doing this is because in step 2 of the initialization the inlet and outlet nodes of the wall mesh are held fixed. Figure 4-10 shows the way we have obtained this initial time $t = 0.5184$ s. The flow and outlet pressure corresponding to this time are $Q = 5.449$ cm^3/s and $P = 135{,}746$ dyn/cm^2.

For the results provided in the following section, we have considered a change of variables for the time defined as $t^* = t - 0.5184$. By doing this, the solutions start at the physical time $t = 0.5184$ described above. In the discussion part of this section, we will provide an example that illustrates the impact of the choice of the initial time in the numerical simulation.

Lastly, we have also made use of the analytical theory to obtain the initial flow history required for the impedance boundary condition.

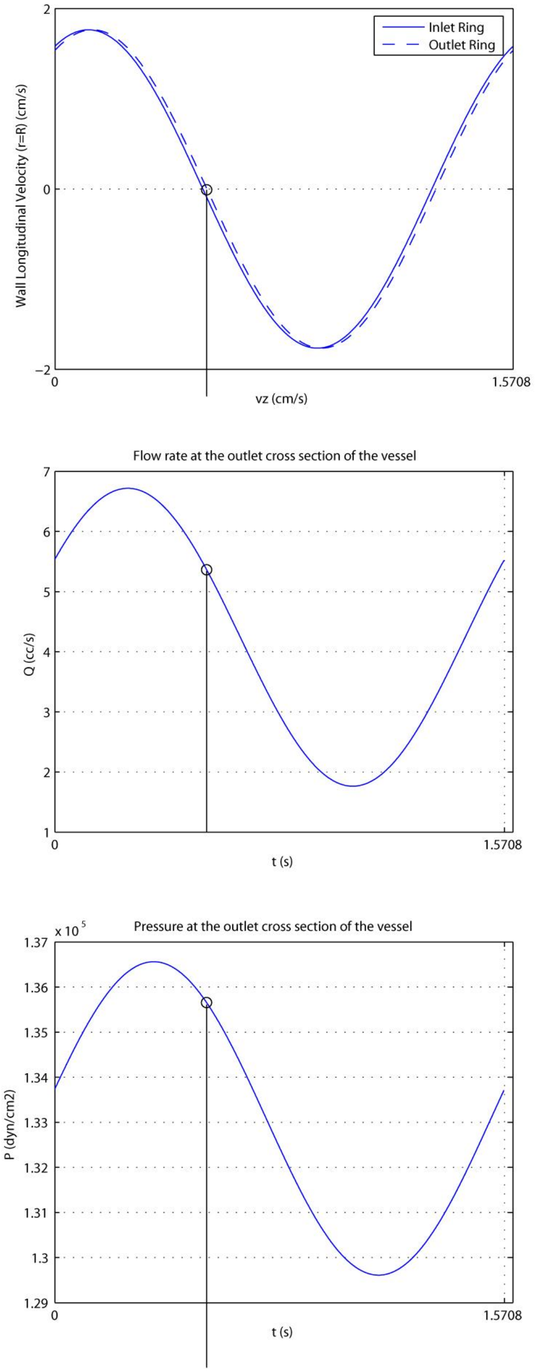

$t = 0.5184$ s

Figure 4-10: Initial time for the numerical solution obtained in such a way that the longitudinal velocities of the inlet and outlet wall rings are as small as possible.

4.2.3 Comparison of the Numerical and Analytical Solutions

We have run the numerical test for five cardiac cycles, using a time step size of $\Delta t = 7.854 \cdot 10^{-3}$ s. The solution was obtained using a 19,267-node, 97,030-element isotropic finite element mesh.

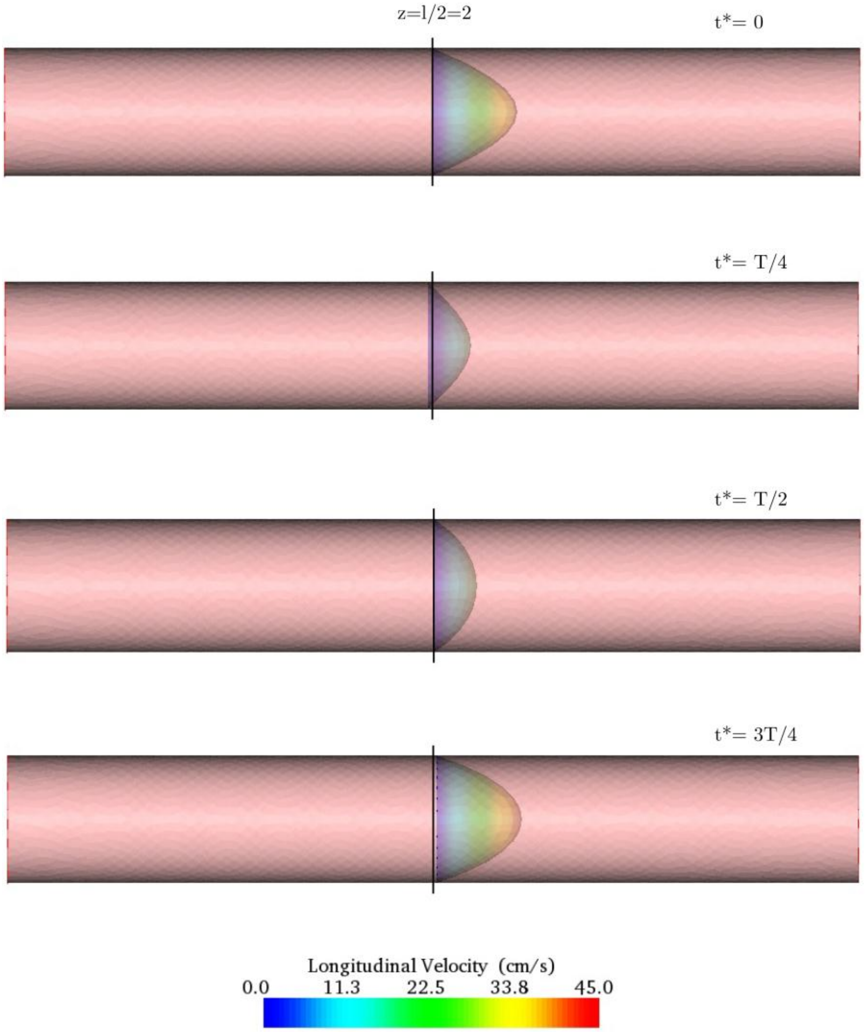

Figure 4-11: Longitudinal velocity profiles at the central cross section of the vessel at different times during the cardiac cycle.

Figure 4-11 shows the velocity profiles at the central cross section of the vessel ($z = 2$) at different points of the cardiac cycle. We have chosen this cross section since it is the farthest away from the boundaries, and therefore experiences the smallest impact coming from the boundary conditions. We can observe how the fluid velocity at the wall oscillates around a zero mean, showing negative values at $t^* = T/4$ and positive values at $t^* = 3T/4$.

Figure 4-12 shows the comparison between the analytical and numerical longitudinal velocity profiles at the central cross section at different points during the cardiac cycle. The two solutions compare extremely well, and demonstrate that the CMM-FSI can accurately reproduce the results of Womersley's deformable wall theory. This is expected, since both theories use the same thin-wall assumption to define the body force driving the motion of the wall from the fluid-wall interface traction field (see equation(3.27), and Section 3.2.4).

We can observe the time periodicity of the solution. During the first part of the cycle ($0<t^*<T/2$), the fluid velocity at the wall is negative, and the flow rate decreases. During the other half of the cycle, the fluid velocity at the wall is positive, and the flow rate increases.

Figure 4-13 shows the comparison between the analytical and numerical flow and pressure profiles at the outlet section of the vessel. We can observe that the

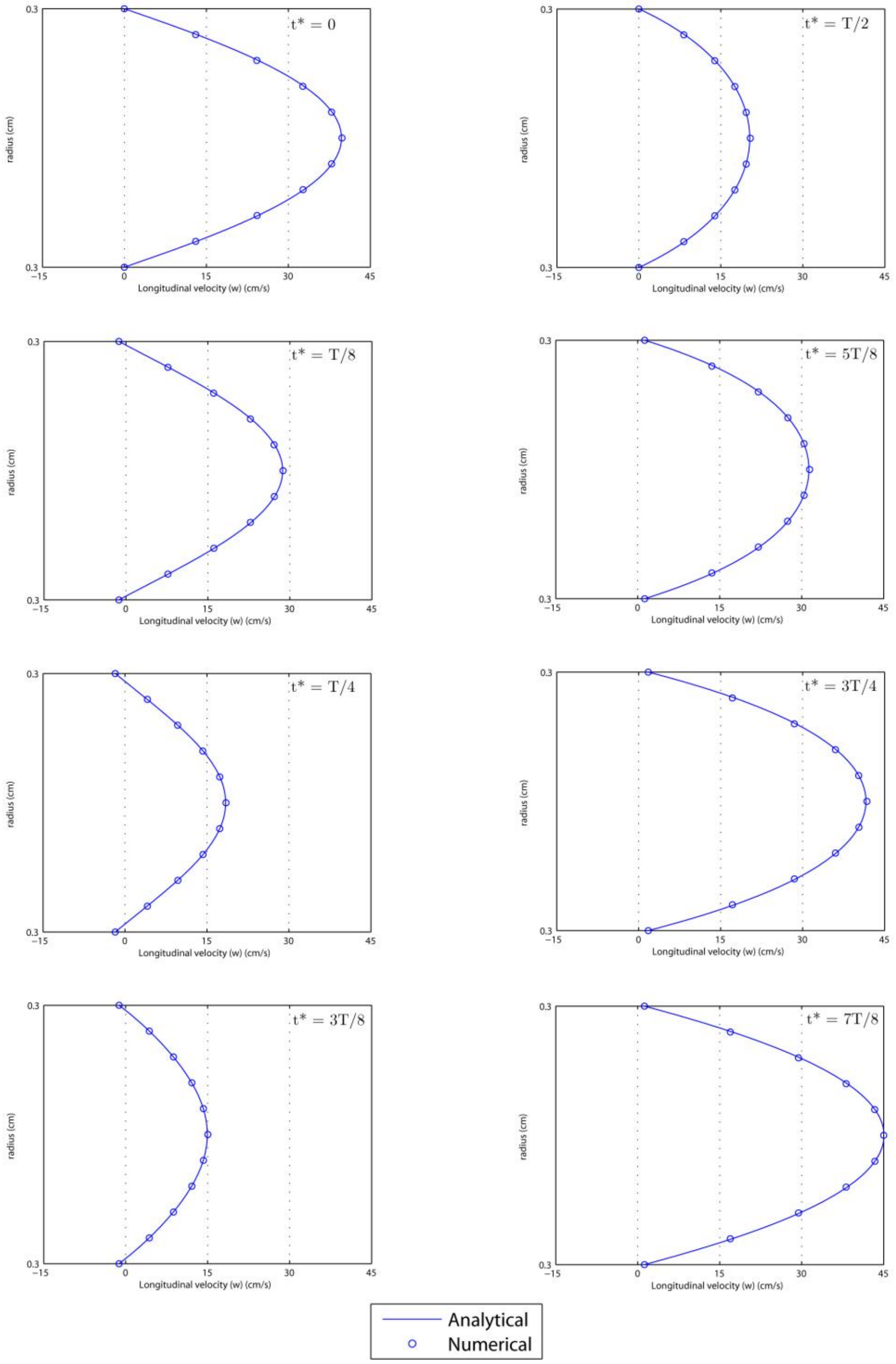

Figure 4-12: Comparison between the analytical and numerical longitudinal velocity profiles at the central section of the vessel (*z*=*l*) at different times during the cardiac cycle.

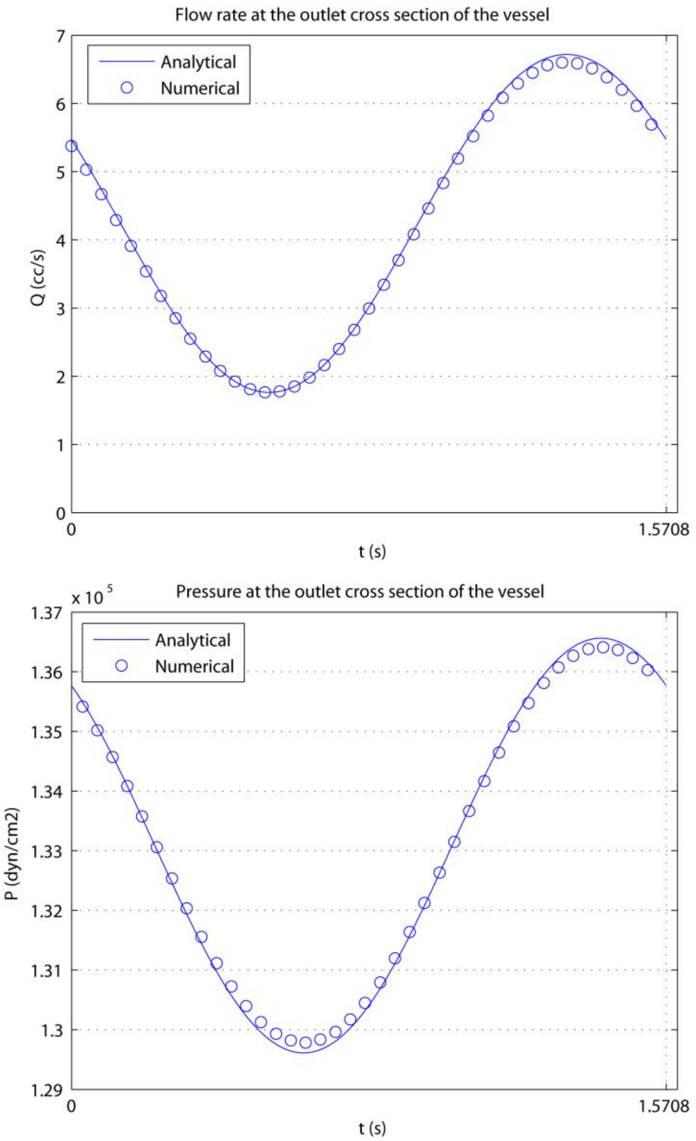

Figure 4-13: Comparison between the analytical and numerical flow and pressure at the outlet of the vessel.

agreement between the solutions is also excellent. The small differences come from errors in the post-processing of the solution when computing the flow rate in the areas close to the wall (these areas now have non-zero velocity values).

4.3 Discussion

In this chapter, we have verified the CMM-FSI, by comparing its results with those given by Womersley's mathematical model of pulsatile blood flow in a thin-walled deformable cylindrical vessel. We have seen that the level of agreement between the analytical and the numerical solutions is excellent.

As predicted by the analytical theory, we have observed elevated values for the longitudinal fluid velocity at the wall (approximately 1.5 cm/s). This longitudinal velocity is much larger than its radial counterpart (0.02 cm/s, Figure 4-3). This is certainly a non-physiologic behavior, since it generates vessel wall longitudinal motion patterns that have not been observed. Womersley tried to correct this response by modifying his basic theory, incorporating a number of improvements to represent the effects of the surrounding tissue on the vessel wall itself (added mass, stiffness, viscoelasticity, longitudinal elastic constraints, etc.)[73]. These additions try to account for the fact that vessel walls are not just elastic conducts surrounded by air, but on the contrary, they are attached to, and supported by, other tissues. With these modifications to his original mathematical model, Womersley improved the level of fidelity of the results provided by the theory. We expect the same behavior once these features are taken into account in our model. However, obtaining the values characterizing the mechanical properties of the tissues surrounding the vessels will require the utilization of either *ex-vivo* experimental techniques or noninvasive *elastography* techniques [74] based on medical images.

In the next chapter, we proceed to apply the method to a number of different problems, ranging from small, ideal geometries, to large, patient-specific models of the vasculature.

Chapter 5

Chapter 5. Applications of the Method

5.1 Introduction

In this chapter, we present a number of examples that illustrate different important characteristics of blood flow in deformable vessels. The first three examples correspond to idealized models of various arteries. The simplicity of the geometries will help to illustrate concepts like wave propagation, effect of boundary conditions, and basic patterns of flow, pressure and wall motion.

The next four examples correspond to large patient-specific models of the cardiovascular system. These examples illustrate the application of the Coupled-Momentum Method to the solution of clinically-relevant problems, both from surgical planning and disease-research perspectives.

For each example, we provide the characteristics of the finite element mesh and time discretization, as well as the material parameters and boundary conditions considered.

5.2 Blood Flow in an Idealized Model of a Carotid Artery-I: Differences between Rigid and Deformable Wall Solutions

We first study the application of the method to a simple cylindrical model of the common carotid artery. The nominal radius and vessel length chosen are 0.3 cm and 12.6 cm, respectively (see Figure 5-1)

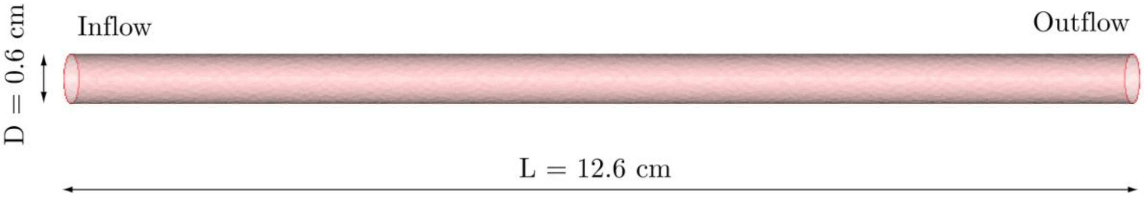

Figure 5-1: Geometry of the idealized model of the common carotid artery.

For the inlet, we prescribe a pulsatile periodic flow wave –with a period of T=1.1 seconds, mapped to a parabolic velocity profile ([25,75,76]). For the outlet, we prescribed an impedance boundary condition as described in [24,72]. The different parameters of the mesh, boundary conditions and material constants are given in the following table:

# of elements	# of nodes	T (s)	Outlet BC	Δt (ms)	E (dyn/cm^2)	ρ^s (g/cm^3)	ζ (cm)	ν	ρ (g/cm^3)	μ (dyn/cm^2)
45,849	9,878	1.1	Impedance	0.8	4.07E+06	1.0	0.03	0.5	1.06	0.04

Table 5-1: Mesh, boundary conditions and material constant parameters used for the idealized model of a common carotid artery.

The solutions were obtained after running the problem for a total of 3 cardiac cycles. The Young's modulus of the vessel wall was chosen such that a maximum deformation of 5 % was obtained with a physiologic range of pressures [77]. The values of the material parameters presented in Table 5-1 are all physiologically realistic.

The wall is fixed by constraining the degrees-of-freedom of the nodes located at the inlet and outlet rings. These are the only constraints applied on the structure. All the nodes of the wall are allowed to move in any direction, including longitudinally, due to the interaction with the internal blood flow.

In this problem, we compare the rigid and deformable solutions obtained using the same boundary conditions. The differences in both the pressure and flow waves between the rigid and deformable wall solutions are discernible, as can be observed in Figure 5-2.

For the pressure field, the pressures obtained with the rigid wall approximation present a higher pulse pressure value. This is a well-known phenomenon in the cardiovascular system, as stiffer vessels tend to experience higher pressure pulses [25], showing larger values in systole and lower in diastole. For the example shown here, the pressure pulse at the inlet face obtained with the rigid wall theory is $\Delta p_{rigid} = 107.51 - 81.95 = 25.56$ mmHg, whereas the pulse obtained with the deformable theory is $\Delta p_{deformable} = 104.81 - 84.85 = 19.96$ mmHg. This represents a difference of 5.60 mmHg (22%), quite significant in a vessel with a simple geometry.

As for the flow waves, the differences are also noticeable. First of all, for the rigid wall model, the inlet and outlet waves are identical as is expected for an incompressible fluid in a rigid domain. However, for the deformable model, while the prescribed inflow is identical to the flow of the rigid case, there is a noticeable phase lag between the inlet and outlet flow waves.

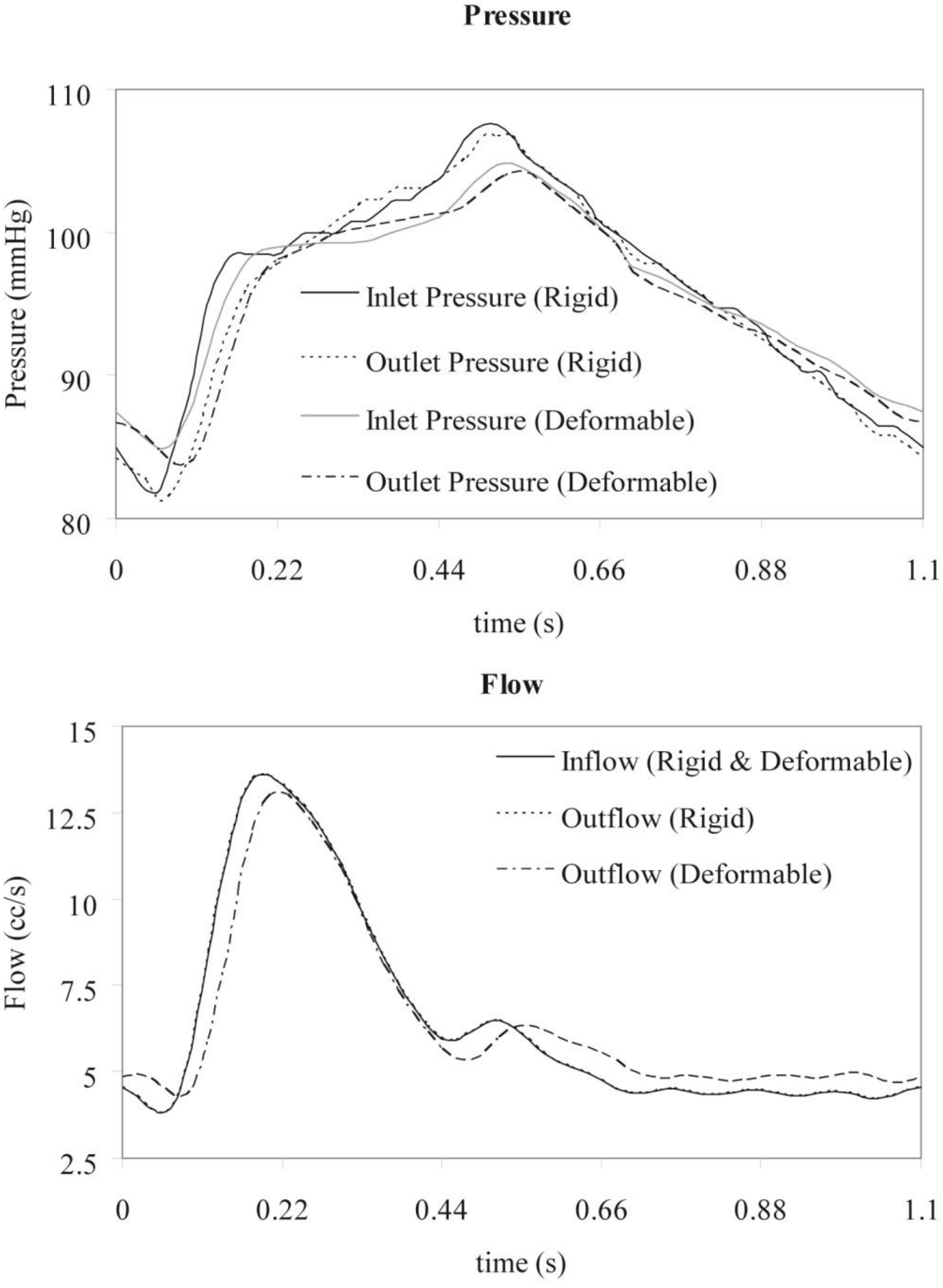

Figure 5-2: Pressure and flow waves at the inlet and outlet faces of the carotid artery model obtained with rigid wall and deformable wall approximations, prescribing the inlet flow and impedance outlet conditions.

This phase lag provides a means to estimate the pulse speed. The phase lag is approximately 0.024 seconds. Considering the vessel length ($L = 12.6$ cm), this produces a pulse speed of approximately 525 cm/s. This is in good agreement with the Moens-Korteweg estimate for pulse speed [77] in an inviscid system given by

$$c_0 = \sqrt{\frac{Eh}{2\rho R}} \tag{5.1}$$

which, for the parameters considered in this problem, produces a wave speed of approximately 451 cm/s.

The flow distribution is also different during systole and diastole. The outlet flow in the deformable case is larger in diastole, because it receives the extra flow that is 'stored' in the vessel during systole. This is a fundamental process in the cardiovascular system, since the deformability of the vessels enables them to store flow during the systolic stage of the cycle and then release it during diastole.

5.3 Blood Flow in an Idealized Model of a Carotid Artery-II: Impact of Different Boundary Conditions

In this problem, we compare the solutions obtained for the same geometry, mesh and material properties described in section 5.2 using three different types of outlet boundary conditions: constant pressure, resistance and impedance as described in [24,72]. In Figure 5-3, we present the results obtained for average pressure over the cross-section, flow and relative radial displacement at two sections, S1 and S2, placed a distance of 0.6 cm from the inlet and outlet faces, respectively. We have chosen these locations since they are far enough from the inlet and outlet (where the nodes on the wall are kept fixed) so the radial deformation is not affected by the presence of the boundary. We define the relative radial displacement as the radial displacement minus its value at the beginning of the cardiac cycle.

5.3.1 Impedance Outlet Boundary Condition

For the impedance boundary condition, we observe the same results as in the problem studied in section 5.2: the pressure and flow waves have realistic amplitudes and phase lag, due to the combined action of the outlet boundary condition and the deformability of the wall.

The relative radial displacement waveforms closely follow the shape of the pressure waveforms at both locations, as expected when using an elastic constitutive model. The maximum radial deformations due to the pulsation of the flow at S1 and S2 are $\Delta r^{S1} = 0.0140\,\text{cm}$ and $\Delta r^{S2} = 0.0145$ cm, and the maximum circumferential strains $\varepsilon_{\theta\theta}^{S1} = 4.67\%$ and $\varepsilon_{\theta\theta}^{S2} = 4.81\%$.

5.3.2 Resistance Outlet Boundary Condition

For the resistance boundary condition, the pressure and relative radial displacement waveforms, as well as the flow waveform at S2 look dramatically different. On the one hand, the pressure waveforms do not show either a physiologic amplitude or phase lag with the flow, since outlet pressure is prescribed simply by scaling the outflow wave by the resistance (20,500 $\text{dynes}\cdot\text{s}\cdot\text{cm}^{-5}$: this resistance corresponds to the zero-frequency component of the impedance function used in the previous case). This generates unrealistically high pressure pulses ($\Delta p_{resistance}^{S1} = 136.83 - 72.73 = 64.10\,\text{mmHg}$) and relative radial deformations ($\Delta r^{S1} = 0.0449$, $\varepsilon_{\theta\theta}^{S1} = 14.93\%$). Furthermore, the shape of the flow wave at S2 is drastically changed as well, since the much larger pressure pulse alters the flow distribution between systole (when more blood volume is ‘stored’ in the vessel) and diastole (where this volume is released through the outlet face). These results are similar to those obtained by Vignon and Taylor [72] using a one-dimensional nonlinear formulation for blood flow in deformable domains, and similar geometry and boundary conditions.

5.3.3 Constant Pressure Outlet Boundary Condition

The constant pressure case presents even more dramatic differences in the solution fields with respect to the impedance boundary condition, especially in the pressure and relative radial deformation. Since a constant pressure is imposed at the outlet (100 mmHg), the pressure field is fairly constant both spatially and temporally. The pressure pulse at S1 is $\Delta p_{constant\ P}^{S1} = 108.22 - 98.50 = 9.72$ mmHg. The corresponding maximum radial deformation is now only $\Delta r^{S1} = 0.0076$ cm and $\varepsilon_{\theta\theta}^{S1} = 2.55\%$. The flow wave at S2 is once again considerably changed by the effects of the pressure waves and the deformability of the vessel.

These examples illustrate the tremendous impact of different boundary conditions when considering wall deformability. The added fidelity in representing the different physical phenomena obtained by modeling wall deformation must be accompanied by a carefully chosen set of boundary conditions in order to obtain physiologically realistic solutions.

Impedance BC

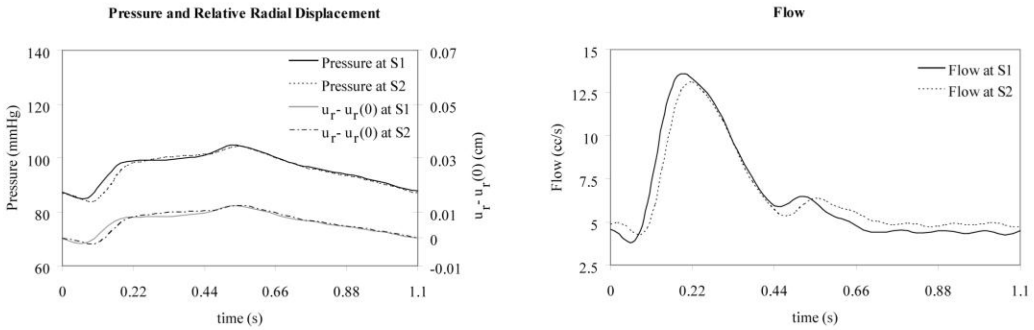

Resistance BC

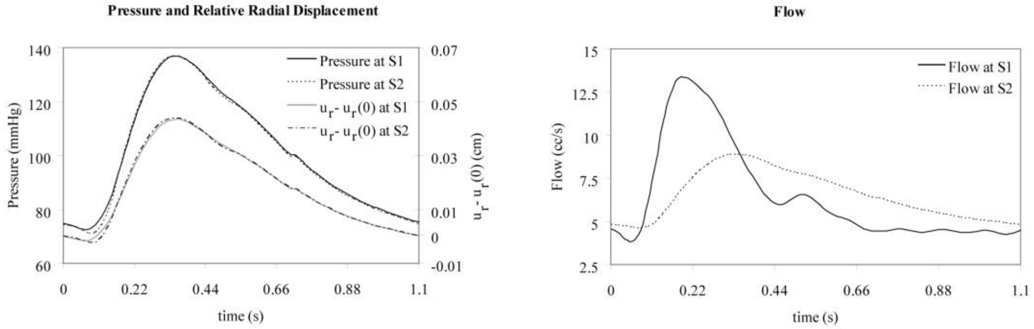

Constant P. BC

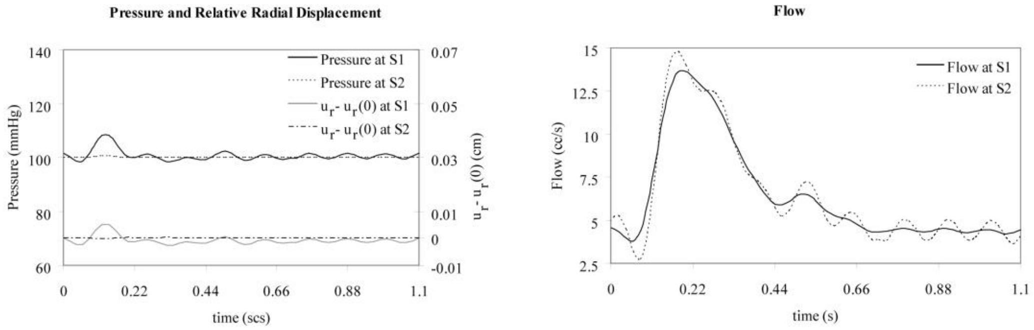

Figure 5-3: Pressure, relative radial displacement and flow waves in sections S1 and S2 of the carotid artery model, obtained using impedance, resistance and constant pressure outlet boundary conditions.
(1 mmHg = 133 Pa, 1 cc/s = 10^{-6} m^3/s).

5.4 Blood Flow through an Idealized Carotid Artery Stenosis Model

In this section, we consider an idealized model of a stenosed carotid artery with the same length and nominal radius as the example presented before. We consider two different scenarios: first, we study a model with a 75% area-reduction stenosis (stenosis diameter $D_s = 0.3\,\mathrm{cm}$) whose central section is 2.5 cm downstream from the inlet face (see Figure 5-4 for details). In the second case, we increase the level of stenosis to 88% area-reduction (stenosis diameter $D_s = 0.2\,\mathrm{cm}$).

The problem presented here may be useful to study a phenomenon called *post-stenotic dilation*. This phenomenon consists of the enlargement of the blood vessel downstream of the stenosed segment of the artery. Boughner and Roach hypothesized that this enlargement is due to the response of the vessel wall to induced oscillations in pressure and flow at frequencies higher than those observed ordinarily in healthy vessels [78].

5.4.1 Fluid-Solid Interaction in a 75% Area Reduction Stenosis

The geometry considered here is the lower-bound of a “critical stenosis”, which refers to area reduction levels of 75% and beyond. More severe levels of restriction are usually symptomatic and often require an intervention. We use the same outlet impedance boundary condition, and the same material properties for the blood and vessel wall as in the problems studied in sections 5.2 and 5.3. The geometry is relatively simple, but the challenging aspect of this problem is the fact that relatively high Reynolds numbers do occur during the cardiac cycle at the level of the stenosis (maximum Reynolds number at peak systole is 2100). The flow is *transitional* (e.g. during systole, the flow velocities increase enough to make the jet at the stenosis transition from laminar to turbulent flow) and non-axisymmetric, and it generates high-frequency loading on the vessel wall. It is beyond the scope of this work to explore the transitional turbulence produced in cases like this. No claims are therefore made regarding the resolution of this phenomenon.

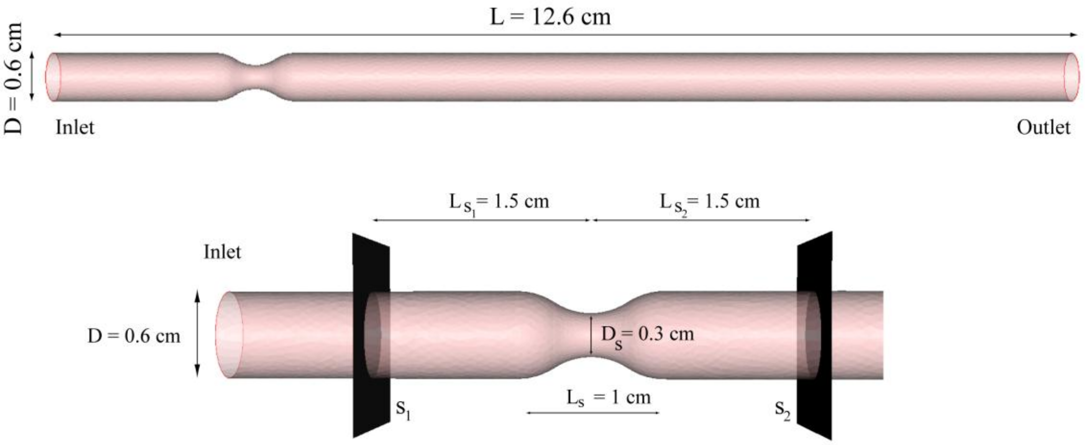

Figure 5-4: Geometric details of the idealized carotid artery stenosis model, and the sections proximal and distal to the stenosis where average pressure, radial wall displacement and flow are computed.

The solution was obtained using a 132,118 element and 26,536 node mesh with a time step of 0.25 ms, and six nonlinear iterations for a total of three cardiac cycles. Figure 5-5 shows the mean pressure and flow waves at the inlet and outlet faces of the model. The pressure waves are remarkably different from the un-stenosed model, especially the inlet pressure. The pressure drop along the vessel length is approximately 2 mmHg during most of diastole, but reaches a maximum value of 13.20 mmHg at peak systole. This is due to the losses occurring at peak systole in the stenosis section. The flow waves are similar to those of the healthy carotid model, as expected from a model of a single vessel with a prescribed inlet flow.

Figure 5-6 shows the results obtained for the pressure averaged over the cross-section, flow and relative averaged radial displacement at two sections, S1 and S2, placed a distance of 1.5 cm from the central section of the stenosis. The pressure waves show a maximum pressure drop of 15.72 mmHg at peak systole. This pressure drop is larger than the pressure drop between the inlet and outlet faces demonstrated previously: this is due to the adverse pressure gradient experienced by the blood flow in the stenosis.

The averaged relative radial displacement is obtained by averaging the radial component of the relative radial displacement for the wall nodes located at each section. These plots follow the shape of the average pressure curves at both sections. *On average*, the displacements are larger upstream of the stenosis, especially during systole due to the larger values of pressure. However, the largest *instantaneous* radial displacements occur downstream of the stenosis due to high-frequency oscillations in the velocity field at this location. This can be observed in Figure 5-7, where we present the spatial distribution for pressure, wall velocity and blood velocity at two points of the cardiac cycle: peak systole and mid-diastole. The maximum pressure drop occurs between the inlet face and the central section of the stenosis, with a value of approximately 30 mmHg at peak systole. The vessel wall velocity plots show the high-frequency effects of the flow

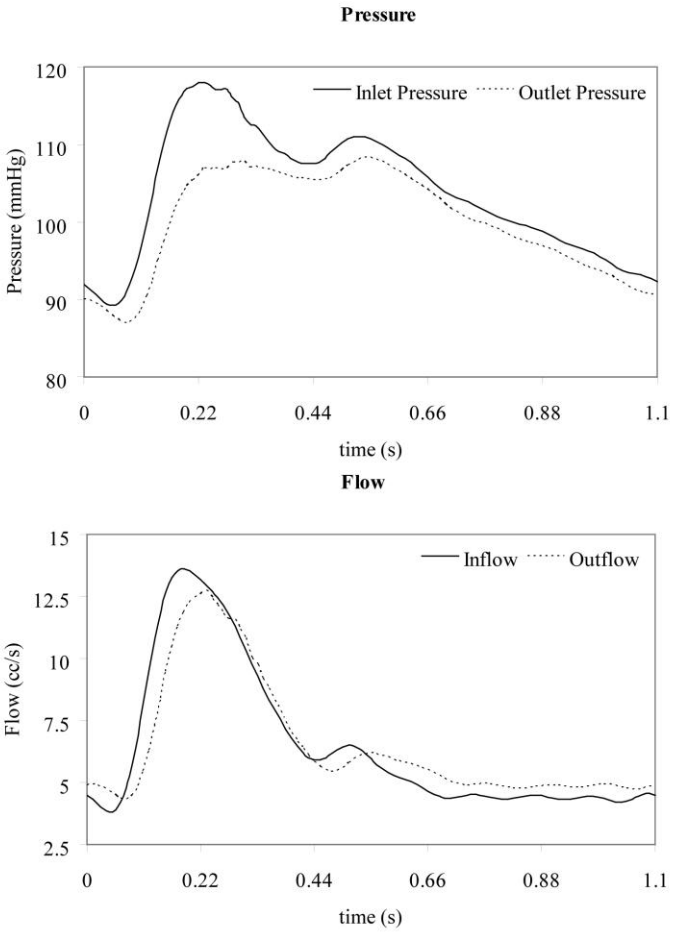

Figure 5-5: Pressure and flow waves at the inlet and outlet faces of the stenosed carotid artery model obtained using impedance outlet boundary conditions and a deformable wall.

field on the structure, especially downstream of the stenosis, where the highest wall velocities occur. These high-frequency velocity oscillations give rise to the largest instantaneous wall displacements mentioned earlier. Lastly, the blood velocity plots show the complex patterns occurring downstream of the stenosis, especially during systole, where the velocity in the stenosis reaches maximum values over 200 cm/s.

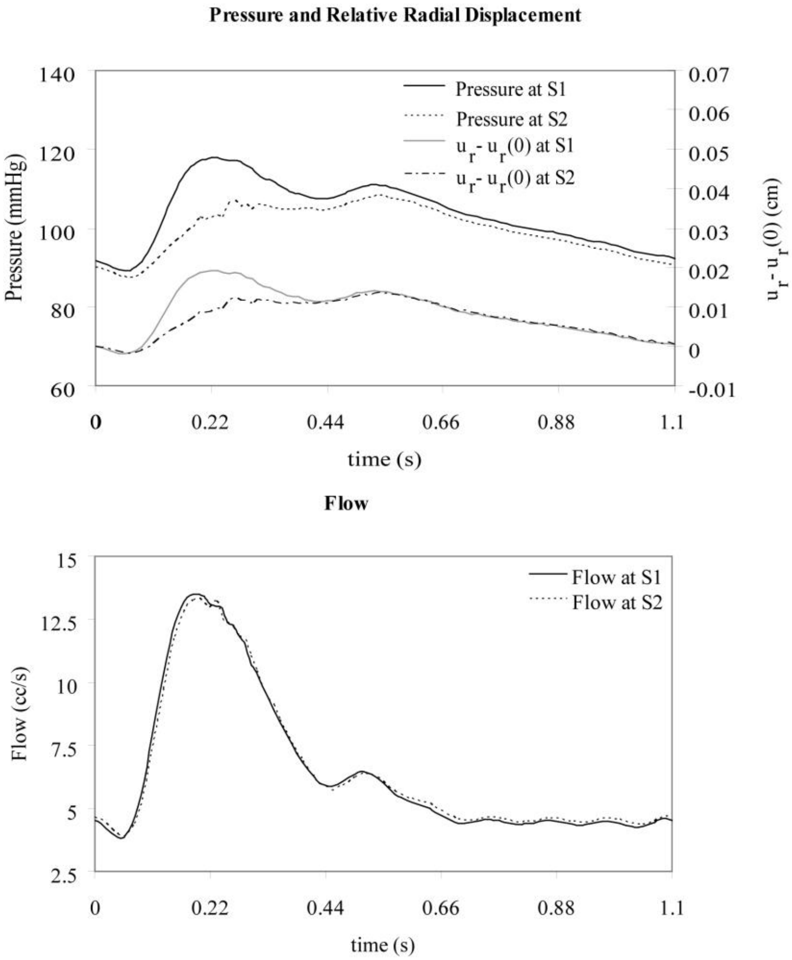

Figure 5-6: Pressure, relative radial displacement and flow waves in sections S1 and S2 of the stenosed carotid artery model, obtained using an impedance outlet boundary condition and a deformable wall.

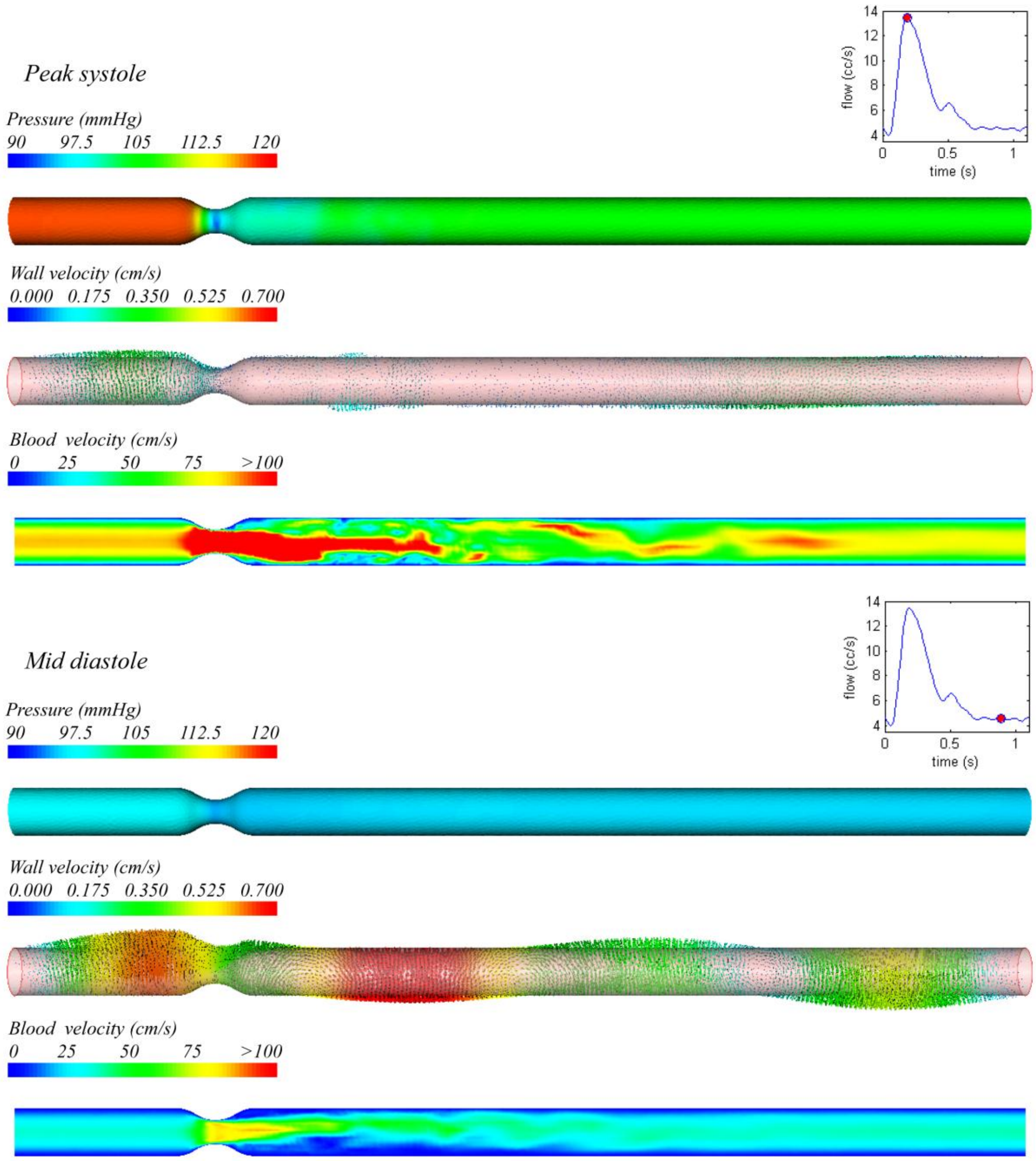

Figure 5-7: Pressure, wall velocity and blood velocity fields at peak systole (above) and mid-diastole (below) for the stenosed carotid artery model. 1 mmHg = 133.3 Pa, 1 cc/s = 10^{-6} m^3/s.

5.4.2 Fluid-Solid Interaction in a 88% Area Reduction Stenosis

In this problem, we can observe the dramatic impact that a tighter degree of stenosis has on both the flow and vessel wall deformation fields. These differences are related to the appearance of even higher frequency components and complex structures on the flow due to the very small luminal area at the stenosis.

The solution was obtained using a 728,340 element and 130,503 node mesh with a time step of 0.25 ms, and six nonlinear iterations for a total of three cardiac cycles. For this problem, the pressure drop along the vessel length is approximately 10 mmHg during most of diastole, but reaches a maximum value of almost 70 mmHg at peak systole. The Reynolds number at peak systole is now slightly over 3000, due to maximum velocities on the order of 650 cm/s.

We proceed to examine the changes in the flow and vessel wall deformation patterns, as well as the energy content of the different flow frequencies relative to the results obtained for the 75% area reduction stenosis model. This comparison is presented in Figure 5-8. In panel a), we compare the flow patterns at peak systole and mid diastole for both models. We can observe that, for the 88% stenosis models, the flow structures are significantly more complex through the entire cardiac cycle. Furthermore, the effects of the stenosis on the velocity field are felt upstream of the stenosis during systole. This is a direct consequence of the much higher pressure drop present in this case.

Panel b) shows the wall displacement history of four points in a cross section 1.5 cm downstream of the stenosis. The results of the two models are dramatically different. For the 75% stenosis model, the displacement history follows closely (with small perturbations) the pressure waves shown in Figure 5-6. On the other hand, in the 88% stenosis model, we observe high frequency fluctuations in the displacement history of all nodes. These vibrations are induced by the oscillations in the flow patterns due to the high degree of stenosis and support the hypothesis of Boughner and Roach on the mechanism behind post-stenotic dilation [78]. The results presented here provide data on the role that the degree of stenosis plays in exciting higher frequencies in the pressure, velocity and displacement fields. Post-stenotic dilation can be observed in the patient-specific aortic coarctation model studied in section 5.6, where we can see a enlargement in the descending thoracic aorta downstream of a 90% area reduction stenosis (see Figure 5-14).

Finally, panel c) shows the differences in the flow power spectra of both models at different cross sections (inlet, outlet and post-stenotic section). We can see that in the 88% reduction model high frequencies (on the order of 20 Hz) not present in the inlet flow wave are excited at the level of the stenosis, and slowly dissipate downstream of the model.

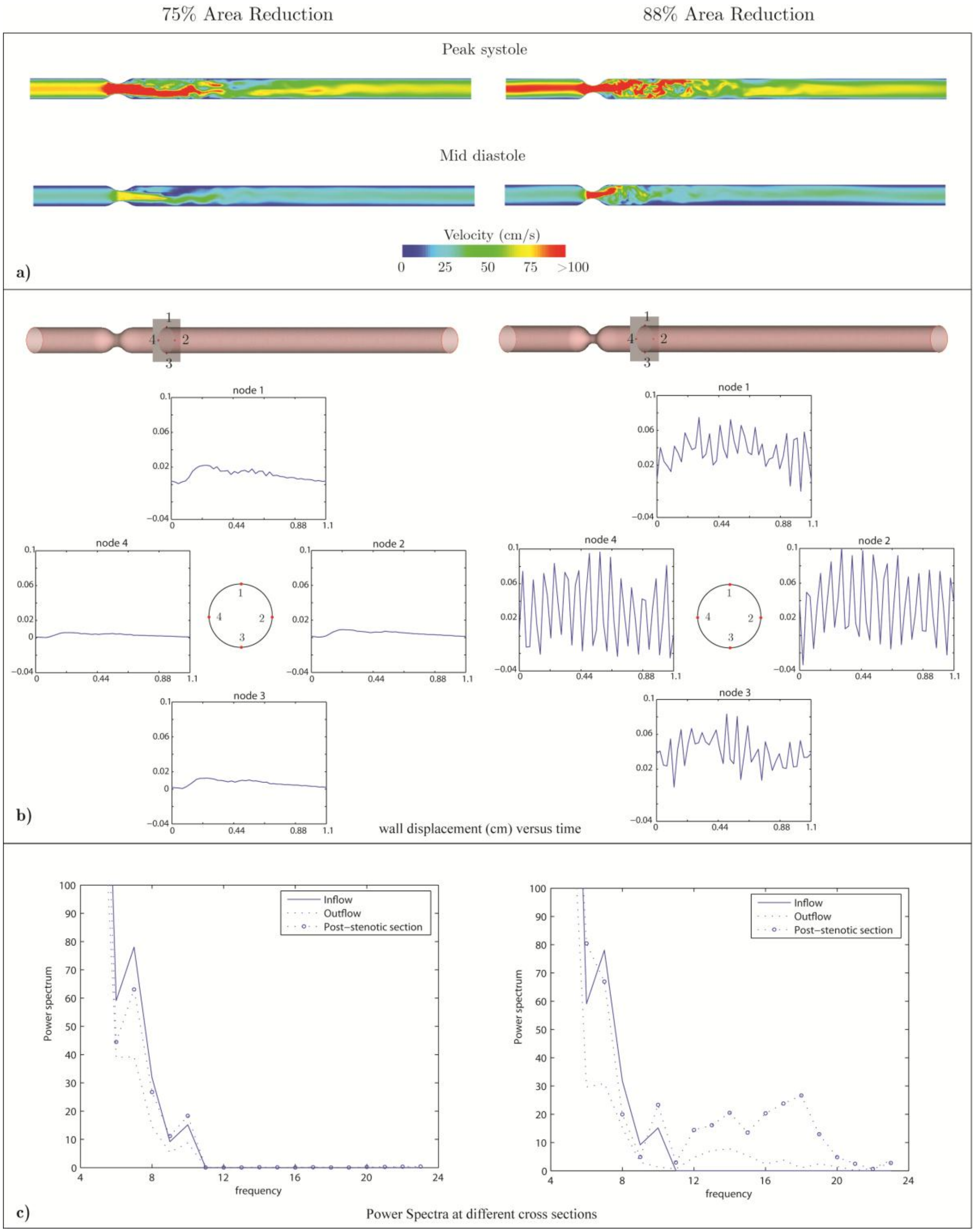

Figure 5-8: a) Blood velocity at peak systole and mid diastole, b) wall displacement history, c) Power spectra of flow at different cross sections. Results corresponding to the 75% area reduction stenosis (left) and 88% area reduction stenosis (right).

5.5 Blood Flow in a Patient-Specific Model of a Healthy Adult Abdominal Aorta

In this problem we consider a patient-specific model of a healthy abdominal aorta, including the renal arteries, the celiac, superior and inferior mesenteric arteries, and the common, external and internal iliac arteries (see Figure 5-9). The geometry and volumetric flow rates were obtained from magnetic resonance imaging data [79]. The measured flow rate at the level of the diaphragm was specified on the inlet face of the model, mapped to a Womersley velocity profile. The cardiac cycle is T=1.05 s. We utilized resistance boundary conditions for all nine outlet faces of the model based on the flow distribution acquired with MRI and completed with literature data [80,81] . The resistance values imposed at each of the nine outlet faces are shown in Figure 5-9.

We have used a constant outlet pressure offset $p_0 = 113{,}330.5\,\text{dyn/cm}^2$ (85 mmHg) in order to obtain a physiologically realistic range of pressures in the solution. The different parameters of the mesh, boundary conditions and material constants are given in Table 5-2:

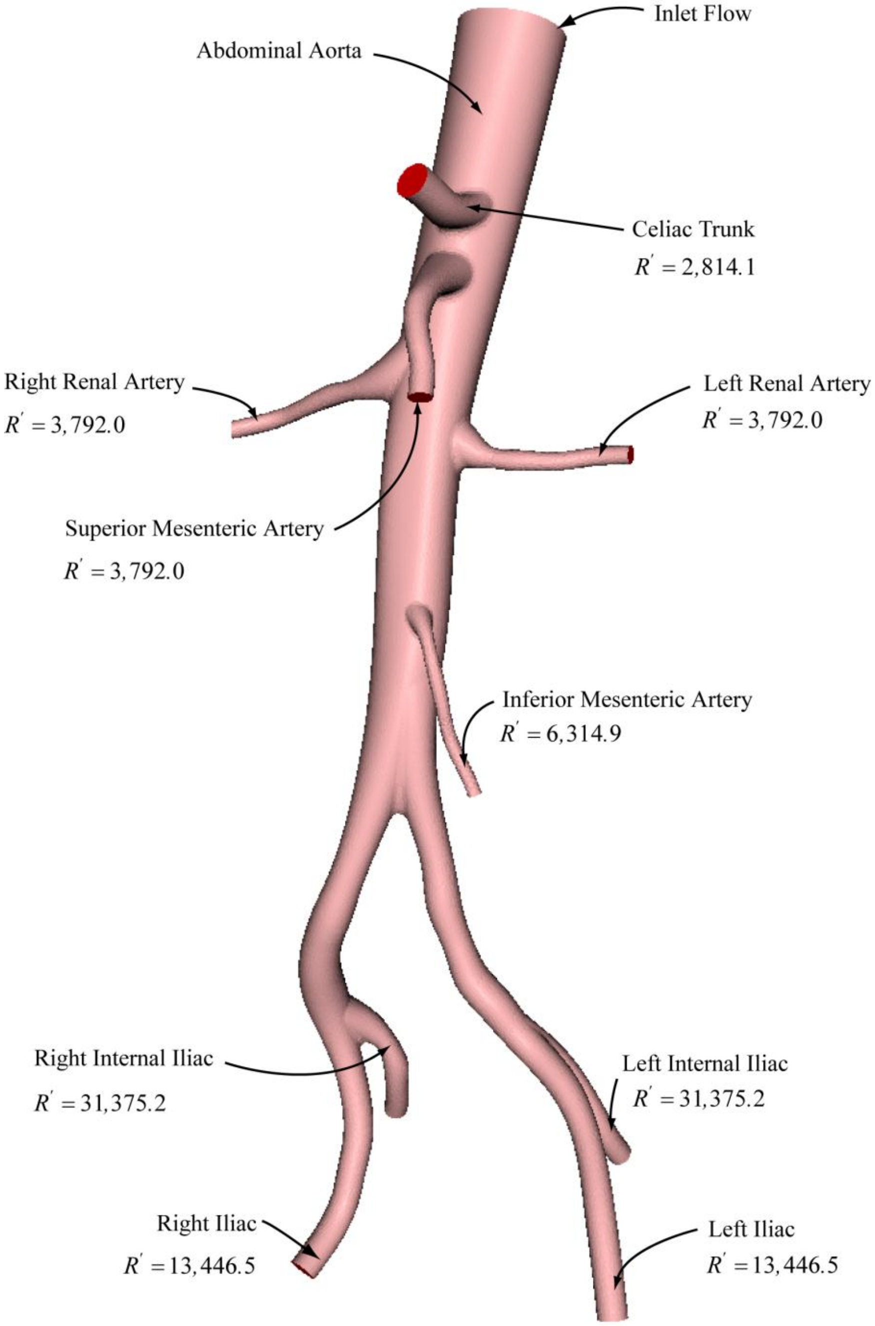

Figure 5-9: Patient-specific model of a healthy abdominal aorta including the renal, celiac, mesenteric and iliac arteries. Each outlet shows the resistance value R' used for the boundary condition $p = p_0 + Q \cdot R'$. p_0 = 113330.5 dyn/cm^2 (85 mmHg). Resistances are given in cgs units (dynes · s · cm^{-5}).

# of elements	# of nodes	T (s)	Outlet BC	Δt (ms)	E (dyn/cm^2)	ρ^s (g/cm^3)	ζ (cm)	ν	ρ (g/cm^3)	μ (dyn/cm^2)
854,151	167,850	1.05	Resistance w/ offset	0.4	4.144E+06	1.0	0.1	0.5	1.06	0.04

Table 5-2: Mesh, boundary conditions and material constant parameters used for the patient-specific model of a healthy abdominal aorta.

The value of the Young's modulus of the vessel wall was chosen so that the maximum radial deformation at the level of the aorta for the physiologic range of pressure is approximately 10%. The wall is fixed by constraining the degrees-of-freedom of the nodes located at the inlet and outlet rings. The solution was obtained using 4 nonlinear iterations per time step, for a total of three cardiac cycles.

Figure 5-10 represents the volumetric flow rate and pressure at the inlet and representative outlets of the patient-specific model obtained using both rigid and deformable wall formulations.

Blood flows into the different branches of the model according to the prescribed resistances representing the demands of the downstream vasculature. The differences between the pressure and flow waves obtained with rigid and deformable wall formulations are very noticeable.

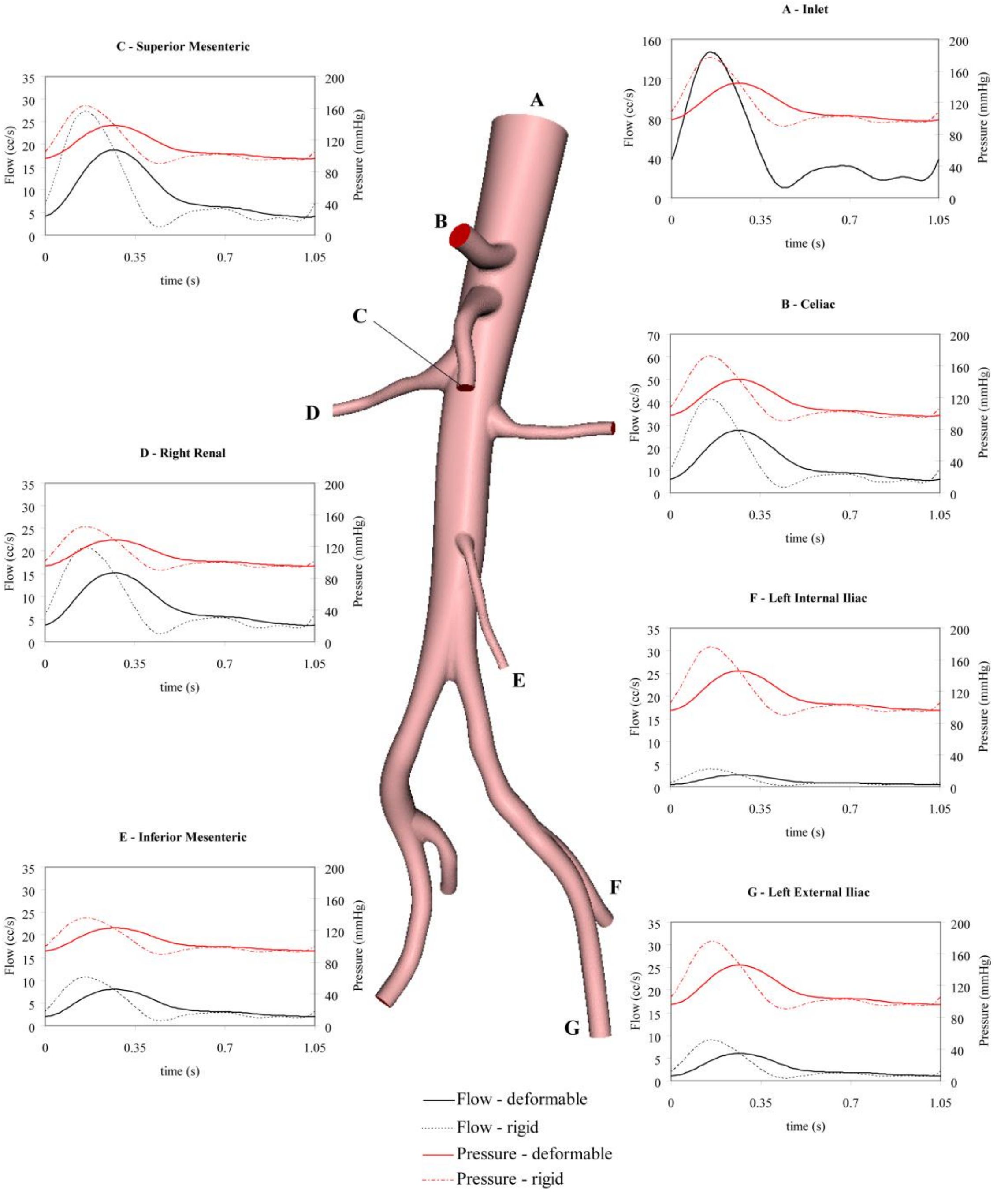

Figure 5-10: Pressure and flow wave forms in a patient-specific model of the human abdominal aorta obtained for both rigid and deformable wall formulations, using a measured periodic inlet flow and resistance outlet boundary conditions. 1 mmHg = 133.3 Pa, 1 cc/s = 10^{-6} m^3/s.

The rigid wall solutions show a much larger pressure pulse both at the inlet and all outlet faces. For example, the pressure pulse at the inlet face of the model is Δp_{rigid}=176.94 - 90.03 = 86.91 mmHg for the rigid wall theory, and only $\Delta p_{deformable}$=144.67-96.69=47.98 mmHg for the deformable wall theory. This is consistent with the results previously shown in section 5.2, and is also in agreement with experimental evidence [25]. Furthermore, the flow distribution between systole and diastole varies significantly between the rigid and deformable wall solutions. Rigid wall profiles show a much higher flow during systole, and smaller in diastole. This is due to the inability of rigid wall models to represent the flow 'storage' occurring at the walls at systole. The stored flow is later on released during diastole, resulting in the observed larger diastolic flows of the deformable theory. It is important to note that the flow through the vessel wall averaged over the cardiac cycle is zero in the periodic state (see Figure 5-11).

Figure 5-12 shows the vessel wall velocity vectors at two points of the cardiac cycle (peak systole and early diastole) and illustrates the mechanism of flow 'storage' at the walls. Lastly, Figure 5-13 shows the blood velocity contours obtained at the same two points of the cardiac cycle.

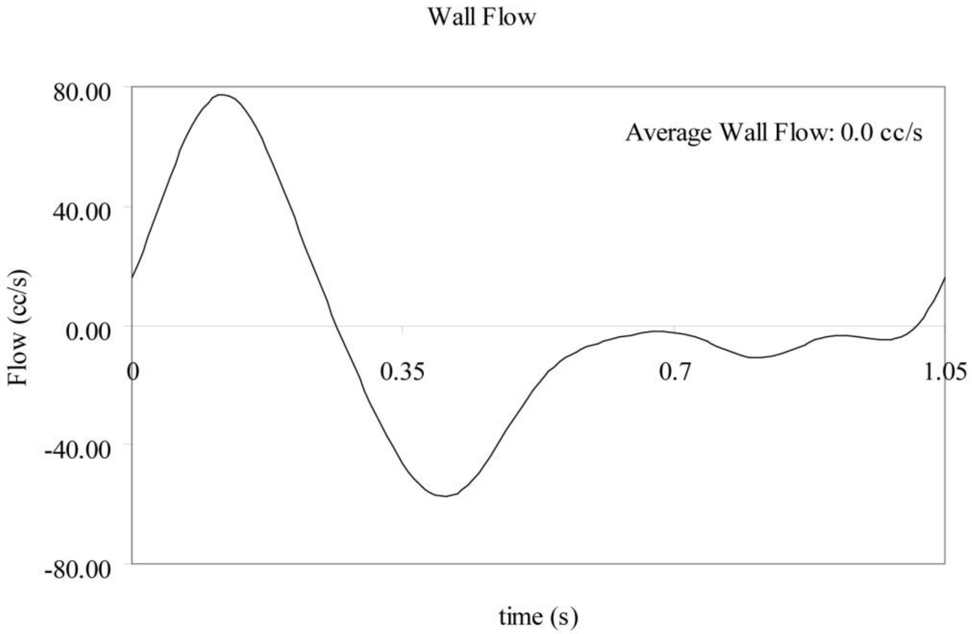

Figure 5-11: Total flow through the wall for the last cardiac cycle of the simulation. Note that the average value of the flow is zero, and therefore the total flow through the outlet faces equals the prescribed inflow over the cardiac cycle.

With this problem, we demonstrate that the Coupled Momentum Method can be applied to large models of the cardiovascular system and that solutions can be obtained in a reasonable time frame: the computational cost of the deformable wall problem was just slightly over two times larger than that of the rigid wall problem, due to the reduction in time step size adopted for the deformable wall formulation.

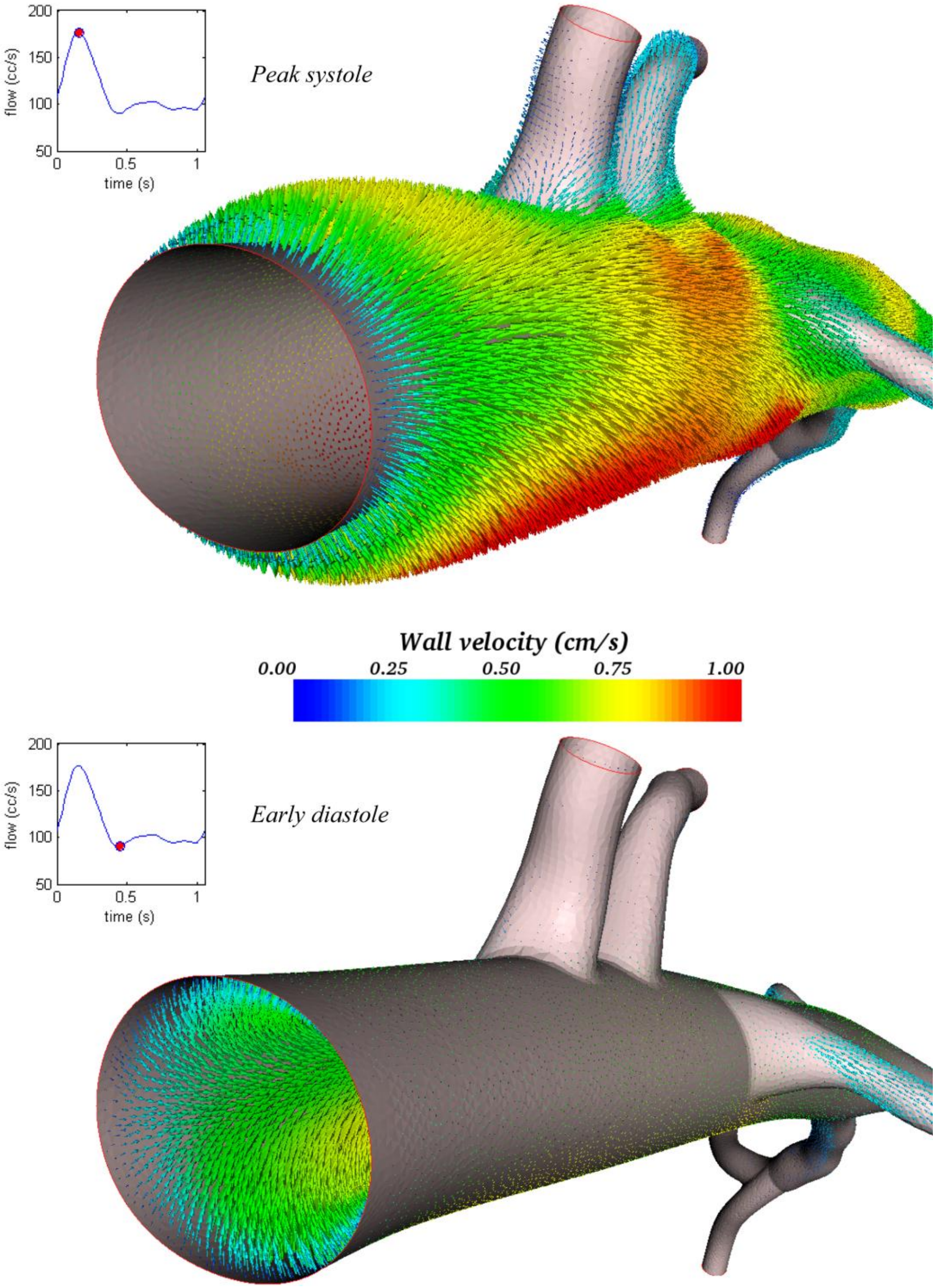

Figure 5-12: Vessel wall velocity vectors obtained for the patient-specific model of the human aorta at two points of the cardiac cycle: peak systole (above), and early diastole (below).

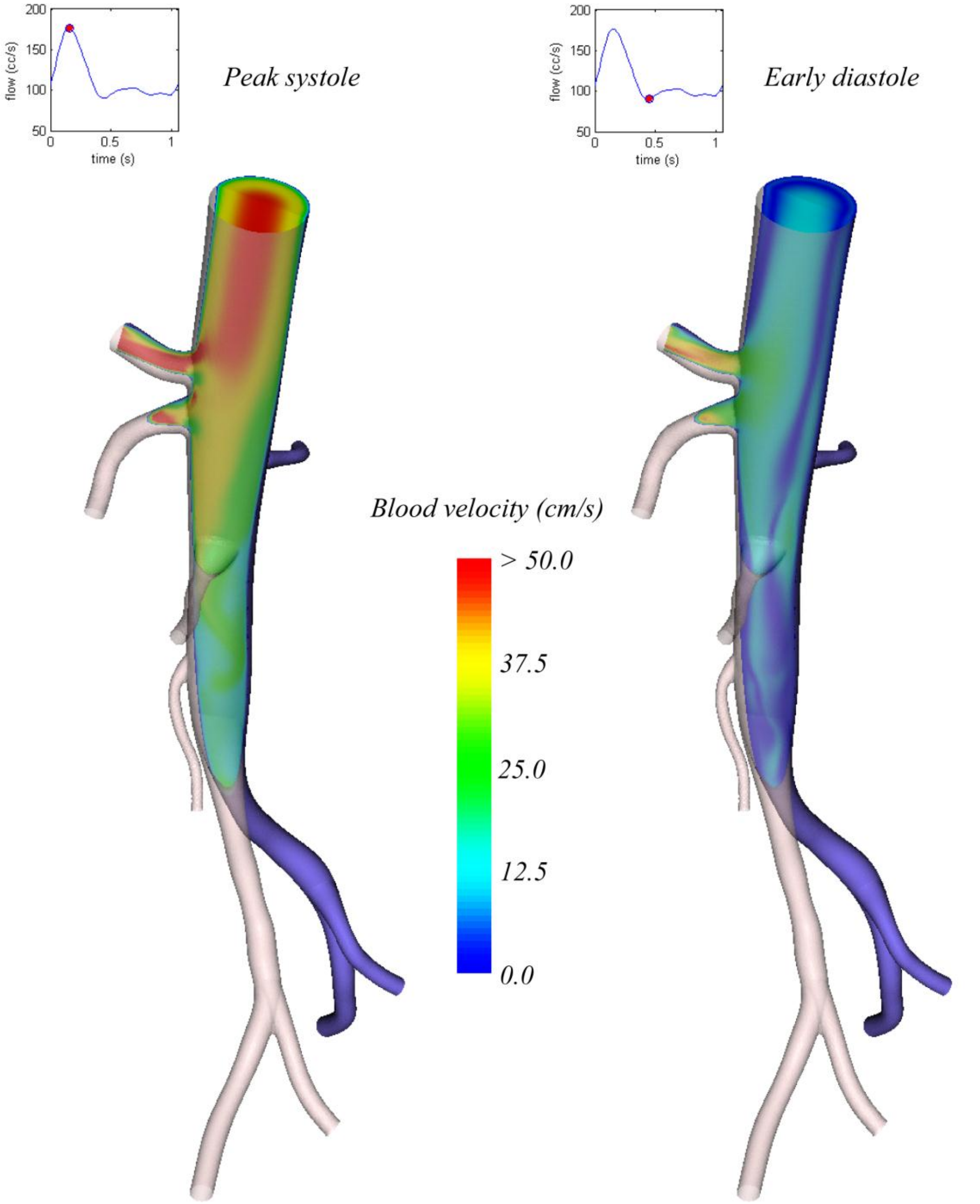

Figure 5-13: Blood velocity contours obtained for the patient-specific model of the human abdominal aorta at two points of the cardiac cycle: peak systole (left) and early diastole (right). The maximum velocities are on the order of 250 cm/s.

5.6 Blood Flow in a Thoracic Aorta Coarctation Model: Application to Surgical Planning

In this section, we demonstrate the applicability of the Coupled-Momentum Method to surgical planning problems. Here, we study the blood flow and wall motion in a patient-specific model of the thoracic aorta of a 13 year old patient with severe aortic coarctation before and after stent placement. A patient-specific model was created from MRI data and preoperative boundary conditions assigned based on measured flow and pressure data. Prior to the intervention, proximal blood pressure was high and wall motion above the coarctation accentuated. Distal blood flow was turbulent and resulted in high-frequency vibrations of the downstream wall. Subsequent to treatment, wall motion normalized, proximal pressures were reduced and fluid turbulence decreased. We describe these results in detail below.

5.6.1 Patient-specific Pre-operative Model of an Aortic Coarctation

In this problem we consider a patient-specific model of a thirteen-year-old patient with a thoracic aortic coarctation. This model includes the left common carotid artery, the brachiocephalic trunk, the vertebral artery and the left subclavian artery outflow branches (see Figure 5-14). The narrowing of the descending aorta represents a 90% reduction in cross-sectional area. The model shows remarkable anatomic abnormalities in the form of two collateral vessels branching from the brachiocephalic trunk and the subclavian arteries, respectively, and connecting back to the descending aorta, in a location distal to the stenosis. These naturally-enlarged collateral vessels serve to reduce the severe pressure gradients arising from the aortic coarctation and supply flow to the distal aorta. The geometry and volumetric flow rates were obtained from magnetic resonance imaging data. The measured flow rate at the level of the ascending thoracic aorta was specified on the inlet face of the model, mapped to a time-varying parabolic velocity profile.

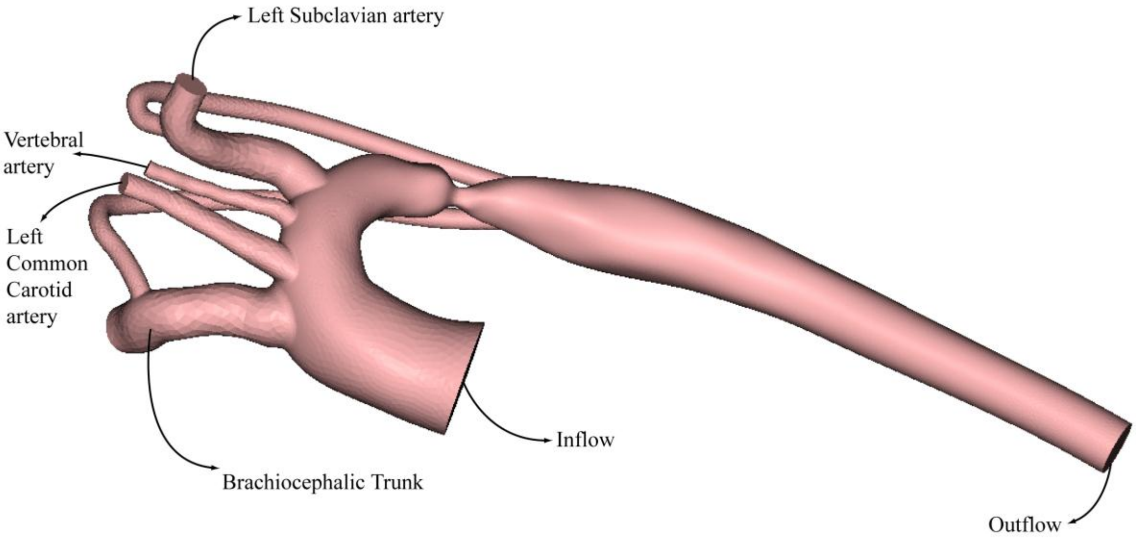

Figure 5-14: Preoperative geometry of a patient-specific thoracic aorta coarctation model, including inflow and outflow faces.

The cardiac cycle is T=1.1 s and the mean flow rate is Q=5 L/min. We utilized resistance boundary conditions for all five outlet faces of the model based on the flow distribution acquired with MRI and complemented with literature data [81]. The resistance values imposed at each outlet face are shown in Table 5-3.

	Btrunk	Carotid	Vertebral	Subclavian	Aorta
Resistance (dynes · s · cm^{-5})	1,843	5,911	53,424	2,862	296

Table 5-3: Resistances imposed at the outlet faces of the patient-specific aortic coarctation model

We have used a constant outlet pressure offset p_0 =87,500 dyn/cm^2 (65.6 mmHg) at the descending aorta outflow face and p_0 =82,000 dyn/cm^2 (61.5 mmHg) at the other outlets in order to obtain a physiologically realistic range of pressures in the solution. The different parameters of the mesh, boundary conditions and material constants are given in Table 5-4:

# of elements	# of nodes	T (s)	Outlet BC	Δt (ms)	E (dyn/cm^2)	ρ^s (gr/cm^3)	ζ (cm)	ν	ρ (gr/cm^3)	μ (dyn/cm^2)
656,512	133,913	1.1	Resistance w/ offset	0.01	4.144E+06	1.0	0.15	0.5	1.06	0.04

Table 5-4: Mesh, boundary conditions and material constant parameters used for the pre-operative patient-specific model of the thoracic aorta coarctation.

The wall is fixed by constraining the degrees-of-freedom of the nodes located at the inlet and outlet rings. The solution was obtained using 4 nonlinear iterations per time step, for a total of two cardiac cycles.

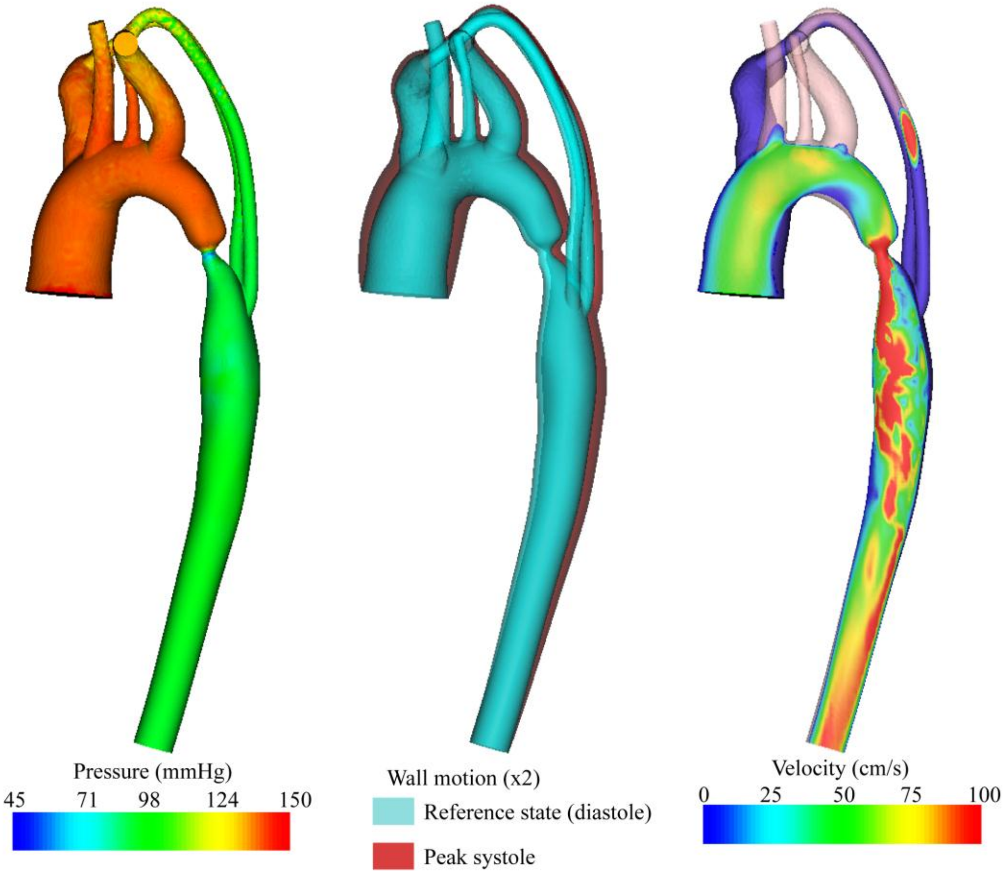

Figure 5-15: Pre-operative blood pressure, wall motion and blood velocity shown at peak systole.

Figure 5-15 shows the pressure, wall deformation and velocity magnitude (along a slice plane) fields. Pressure (shown at peak systole) presents a very large gradient across the stenosis, with a maximum value at peak systole of $\Delta P_{sys} = 50.8$ mmHg (see Figure 5-16).

Wall motion is shown in Figure 5-15 at two different points of the cardiac cycle. The reference state given in blue corresponds to diastole, whereas the peak systolic geometry is shown in red. We can observe a significant distension of the aorta upstream of the stenosis in peak systole due to the large values of the pressure field. This is not seen downstream of the stenosis, where the pressure field takes on much smaller values. The vessel wall motion distal to the stenosis exhibits a high-frequency fluttering pattern due to the impinging flow coming from the collateral vessels and the stenosis. The flow field is turbulent, (max. Reynolds number at peak systole is 15,000), and therefore a very small time step size was required to solve this problem. No turbulence model was used.

Figure 5-16 shows the average pressures and flows at the outlet faces of the model. We can observe the very large pressure drop across the stenosis occurring at peak systole. The flow graph shows the phase lag between the prescribed inflow and the outflow waves of the model, due to the finite wave speed and "storage" of the systolic flow by the highly compliant aortic wall, subsequently released to the distal aorta during diastole. This storage of flow is the physiologic hallmark of the aorta that can be replicated by our formulation and that of deformable models in general.

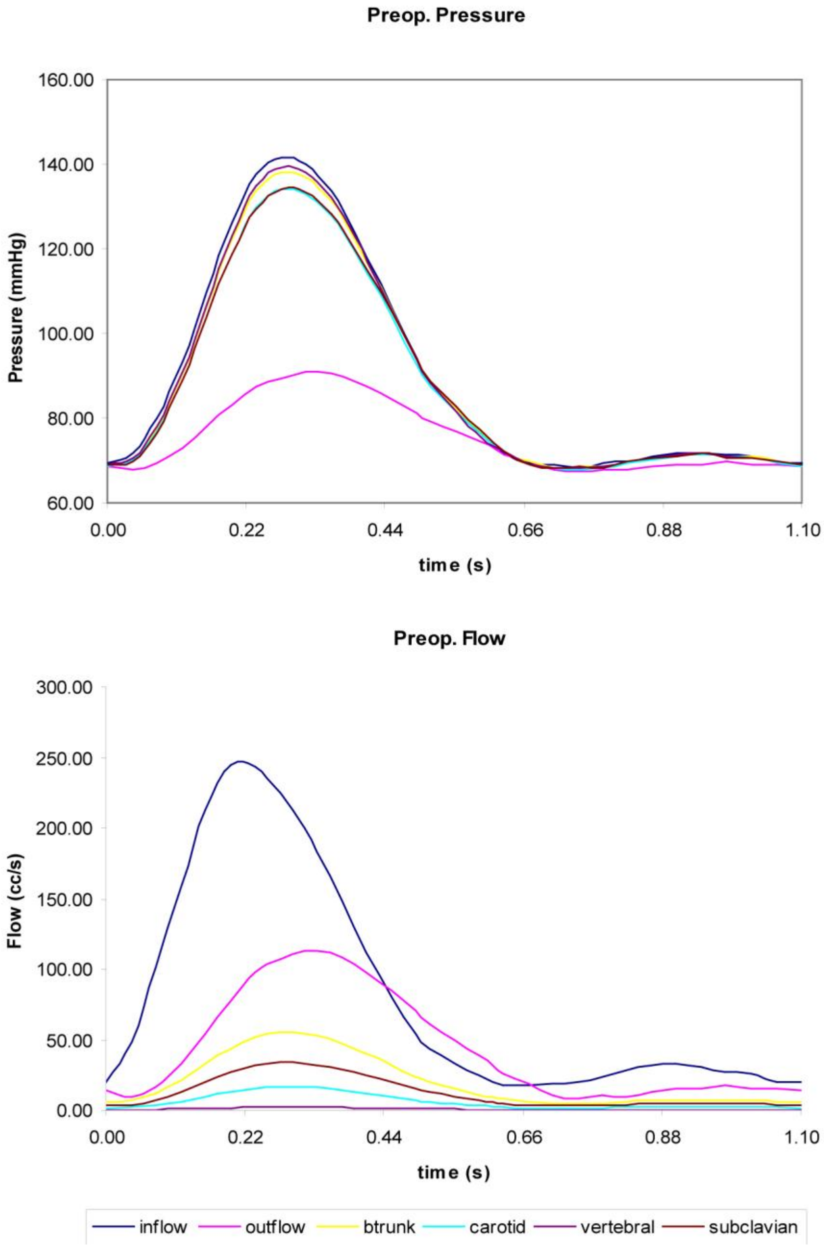

Figure 5-16: Average pressure and flow over the cardiac cycle at the outlet faces of the patient-specific pre-operative model of the thoracic aorta coarctation.

5.6.2 Patient-specific Post-operative Model of an Aortic Coarctation after Stent Placement

In this problem we simulate the effects of stent implantation on the blood flow and vessel wall motion for the thirteen-year-old patient with thoracic aortic coarctation. The stent is represented as a rigid section; due to its much higher stiffness compared to that of the aortic wall. The same measured inlet flow wave, wall mechanical properties, constant outlet pressure offsets and resistances from the previous case are considered here. Note that in this example, we neglect vasodilation and vasoconstriction of the distal vascular beds that would ordinarily accompany treatment of vascular obstructions. For this problem, the solution was obtained using a 504,885 element and 98,885 node mesh with a time step of 0.4 ms, and 4 nonlinear iterations per time step, for a total of two cardiac cycles.

Figure 5-17 shows the pressure, wall deformation and velocity magnitude fields. The effects of the stent implantation on all these fields are remarkable. First of all, the pressure drop across the stenosis is reduced dramatically. The maximum pressure drop at peak systole is now ΔP_{sus}=9.7 mmHg (see Figure 5-18). Currently the residual gradient is the most commonly used clinical parameter of success. Application of this formulation will greatly enhance our current understanding of coarctation in the aorta and lead to new determinants of “success”.

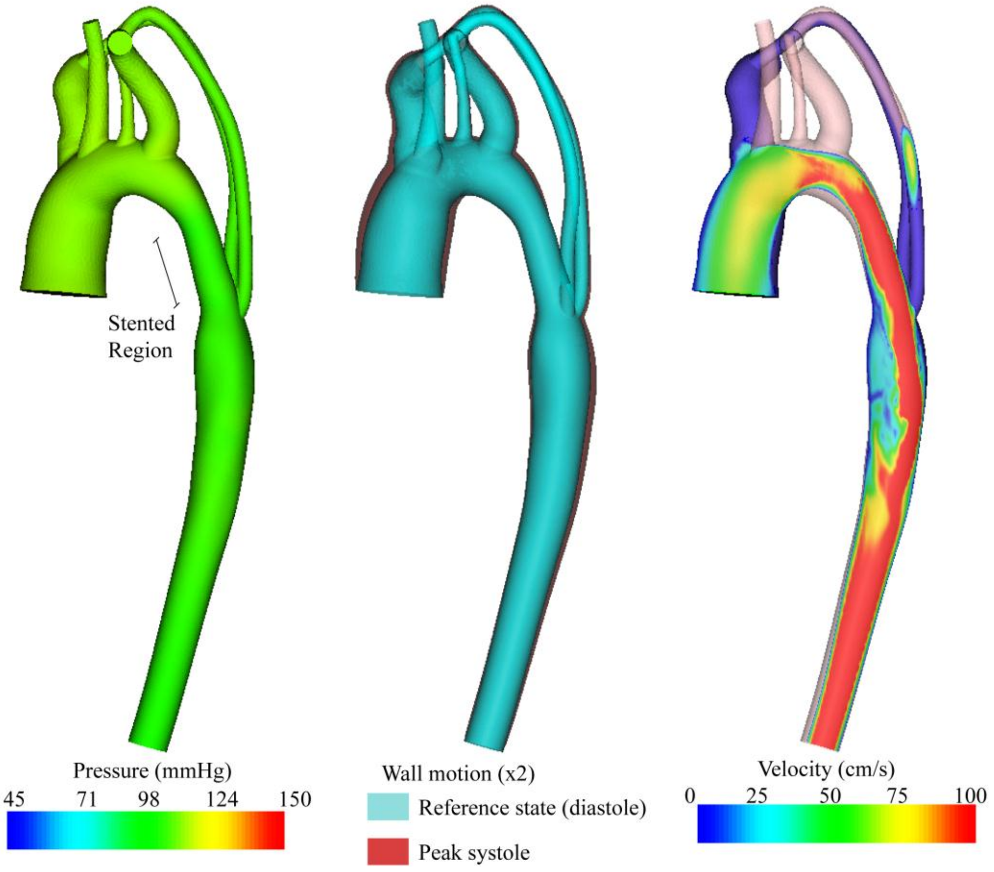

Figure 5-17: Post-operative blood pressure, wall motion and blood velocity shown at peak systole.

Furthermore, wall motion is significantly reduced upstream of the stenosis due to the much smaller driving pressure. Lastly, the level of turbulence of the velocity field is also dramatically reduced due to the relief of the coarctation.

Consequently, the high-frequency fluttering of the vessel wall downstream of the stenosis is almost completely eliminated.

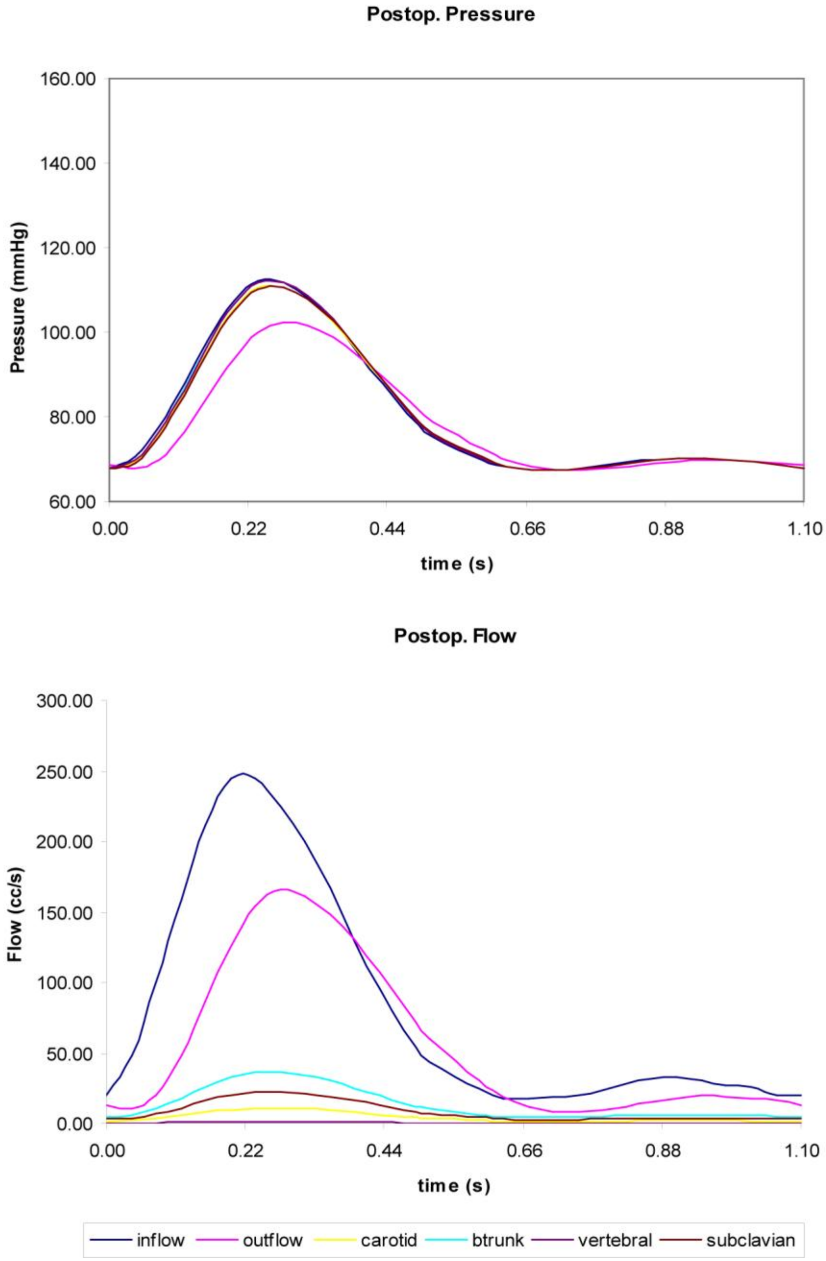

Figure 5-18: Average pressure and flow over the cardiac cycle at the outlet faces of the patient-specific post-operative model of the thoracic aorta coarctation.

Figure 5-18 also shows that the amount of flow going through the outlet face of the descending aorta is larger now than in the preoperative case (3.25 L/min versus 2.56 L/min). This is another consequence of the significant reduction in flow resistance in the thoracic aorta after the implantation of the stent.

5.7 Blood Flow in an Abdominal Aortic Aneurysm Model: Application to Disease Research I

In this section, we present the first of two examples devoted to applications of the Coupled-Momentum Method to disease research problems. Here, we consider a patient-specific model of an abdominal aortic aneurysm (AAA), including the renal arteries feeding the kidneys, the celiac and superior mesenteric arteries feeding the viscera, and the iliac arteries, including the internal iliac arteries (see Figure 5-19). The model corresponds to a 60-year-old female subject.

The goal of this section is to understand how the dynamics of blood flow in a patient with an abdominal aortic aneurysm change when going from rest to exercise conditions. As we will observe, the patterns of wall motion (and therefore wall stress) differ very significantly and may provide some insight into whether or not moderate exercise is advisable for these types of patients.

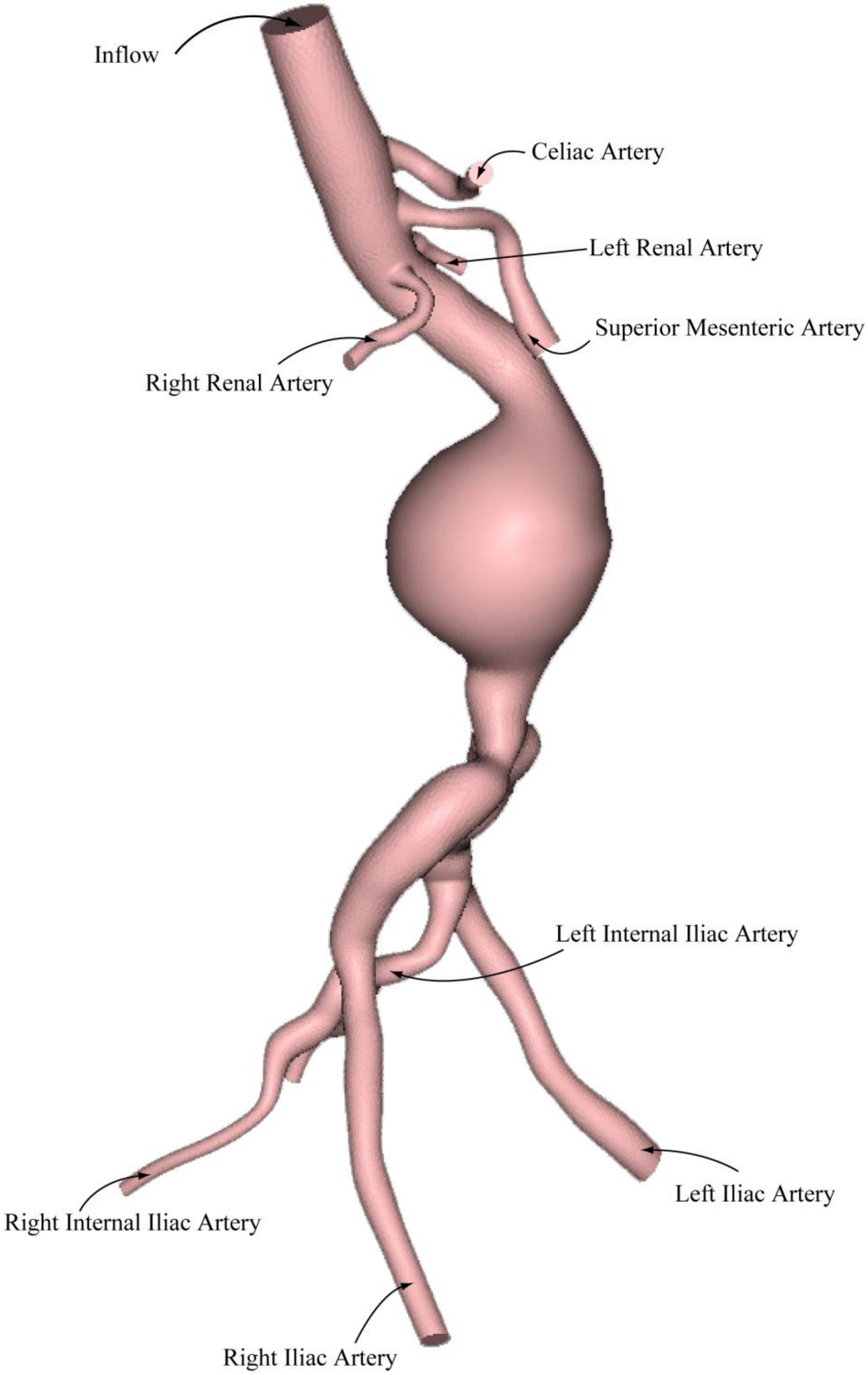

Figure 5-19: Geometry of a patient-specific abdominal aorta aneurysm model, including the renal, celiac, mesenteric and iliac arteries.

5.7.1 Patient-specific AAA Model under Rest Conditions

The geometry and volumetric flow rates for this model were obtained from magnetic resonance imaging data. The measured flow rate at the level of the diaphragm was specified on the inlet face of the model, mapped to a Womersley velocity profile. The cardiac cycle is T=1.05 s and the flow is Q=3.59 L/min. We utilized resistance boundary conditions for all eight outlet faces of the model based on the flow distribution acquired with MRI.

The resistance values imposed at each of the outlet faces are shown in Table 5-5. We have used a constant pressure offset p_0 =72,870 dyn/cm^2 (55 mmHg) in order to obtain a physiologically realistic range of pressures in the solution.

	Celiac	SMA	Left renal	Right renal	Left iliac	Left int-iliac	Right Iliac	Right int-iliac
Resistance (dynes · s · cm^{-5})	1,946	2,622	2,622	2,622	2,912	6,790	2,912	6,790

Table 5-5: Resistances imposed at the outlet faces of the patient-specific AAA model under rest conditions.

The different parameters of the mesh, boundary conditions and material constants are given in Table 5-6:

# of elements	# of nodes	T (s)	Outlet BC	Δt (ms)	E (dyn/cm^2)	ρ^s (g/cm^3)	ζ (cm)	ν	ρ (g/cm^3)	μ (dyn/cm^2)
663,243	135,522	1.05	Resistance w/ offset	0.4	4.144E+06	1.0	0.10	0.5	1.06	0.04

Table 5-6: Mesh, boundary conditions and material constant parameters used for the patient-specific AAA model under rest conditions.

The wall is fixed by constraining the degrees-of-freedom of the nodes located at the inlet and outlet rings. The solution was obtained using 5 nonlinear iterations per time step, for a total of three cardiac cycles.

Figure 5-20 shows the pressure, wall deformation and velocity magnitude (along a slice plane) fields during peak systole. In this problem, we observe that the pressure field shows a maximum value of 95 mmHg, and a relatively small pressure gradient through the model. This is an indicator that the pressure losses are not significant. On the other hand, the velocity contour shows complex recirculating patterns with maximum velocities on the order of 50 cm/s at the upper level of the abdominal aorta. The vessel wall deformation is moderate, consisting primarily of a radial expansion and contraction pattern at the level of the aneurysm. A net forward and downward motion of the iliac bifurcation can also be observed. These motion patterns are certainly not radially symmetric and may be related to the evolution of the level of tortuosity of the vessels with aging and aneurysm growth.

These computations were performed with minimal increase (about a factor of two) in computational time compared to that of rigid wall theory.

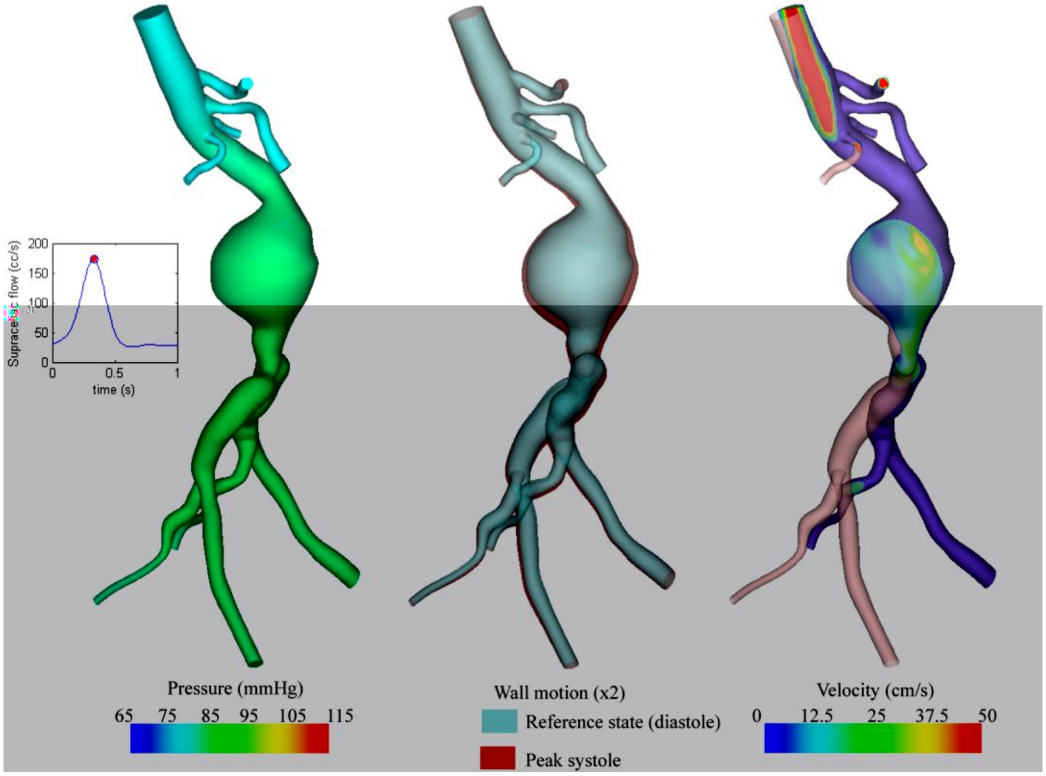

Figure 5-20: Pressure, wall motion and blood velocity shown at peak systole for the AAA model under rest conditions. Blood pressure and velocity magnitude (along a slice plane) are shown at peak systole.

5.7.2 Patient-specific AAA Model under Simulated Exercise Conditions

In this problem we consider the same model as in the previous example but under simulated exercise conditions. The cardiac cycle is now T=0.7 s and the flow is Q=10.77 L/min, representing a three-fold increase.

We have used a constant outlet pressure offset p_0 =68,726 dyn/cm^2 (51.2 mmHg) and the resistance values shown in Table 5-7 in order to obtain a physiologically realistic range of pressures. Note that the resistance values of the celiac, SMA and renal arteries increase with respect to the values considered for resting conditions (given in Table 5-5), whereas the resistance of the arteries supplying blood to the leg decreases. These new values account for the changes in blood flow distribution between the viscera and legs that occur during exercise conditions.

	Celiac	SMA	Left renal	Right renal	Left iliac	Left int-iliac	Right Iliac	Right int-iliac
Resistance (dynes · s · cm^{-5})	2,694	3,630	3,630	3,630	2,912	6,790	2,912	6,790

Table 5-7: Resistances imposed at the outlet faces of the patient-specific AAA model under exercise conditions.

Figure 5-21 shows the pressure, wall deformation and velocity contour along a slice plane at peak systole. We can observe that the pressure at the level of the aneurysm has increased by 20 mmHg with respect to that seen in rest conditions. Similarly, the velocity field shows larger values throughout the model. But perhaps the most remarkable difference between this example and the previous one can be seen in the patterns of the wall deformation. In this case, the deformation of the wall is no longer occurring in a radial expansion and contraction mode, but rather as a net motion forward and backwards due to the much larger inertial forces exerted on the wall by the impinging blood stream.

There are undoubtedly many important factors neglected in the present simulation, like the effects of the surrounding tissue and the tethering of the vessel wall to the spine, just to name a few. However, despite these limitations, it seems clear that the patterns of the wall motion and blood flow change very significantly when going from rest to moderate exercise conditions. Expanding the methods presented in this thesis to account for the effects of the factors mentioned above may make it possible to better assess the changes in the dynamic loading on the vessel wall and therefore evaluate the risk of aneurysm rupture in these patients.

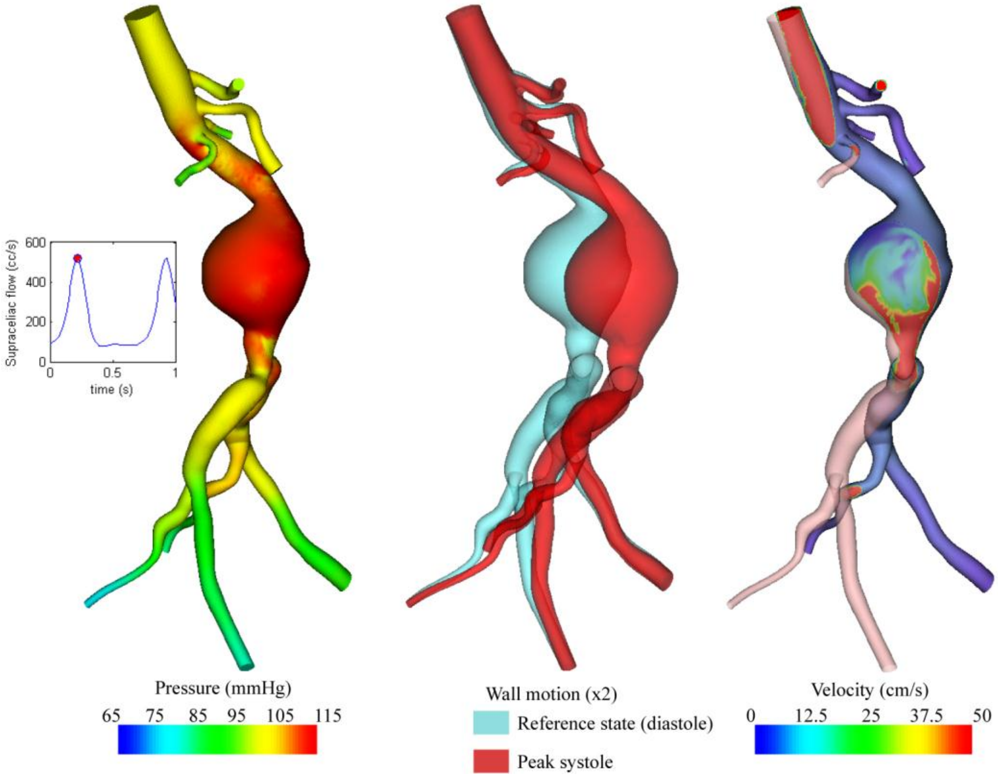

Figure 5-21: Pressure, wall motion and blood velocity shown at peak systole for the AAA model under simulated exercise conditions. Blood pressure and velocity magnitude (along a slice plane) are shown at peak systole.

5.8 Blood Flow in a Model of the circle of Willis: Application to Disease Research II

In this section, we present the last example dedicated to disease research problems. Here, we consider a patient-specific model of the main arteries of the cerebro-vasculature. The arteries providing blood supply to the brain form a complex system as can be seen in Figure 5-22. The total Cerebral Blood Flow (CBF) consists of the sum of the flows carried by three different vessels: the internal carotid arteries (left and right) and the basilar artery. These arteries branch off in different locations and usually form redundant pathways to flow. Quite often, these redundant paths constitute a complete loop known as the circle of Willis.

We are interested in exploring the hemodynamics of blood flow in these parts of the vascular system that are particularly prone to the development of aneurysms, especially of the saccular type [82]. These aneurysms typically form in the areas close to the intersection of the middle and anterior cerebral arteries with the internal carotid artery. However, fusiform aneurysms also develop in other parts of the cerebro-vasculature (like the basilar artery). Once the hemodynamic forces acting on the vessel wall are known, they can be used as inputs in stress-mediated algorithms of growth and development of arterial tissue [83].

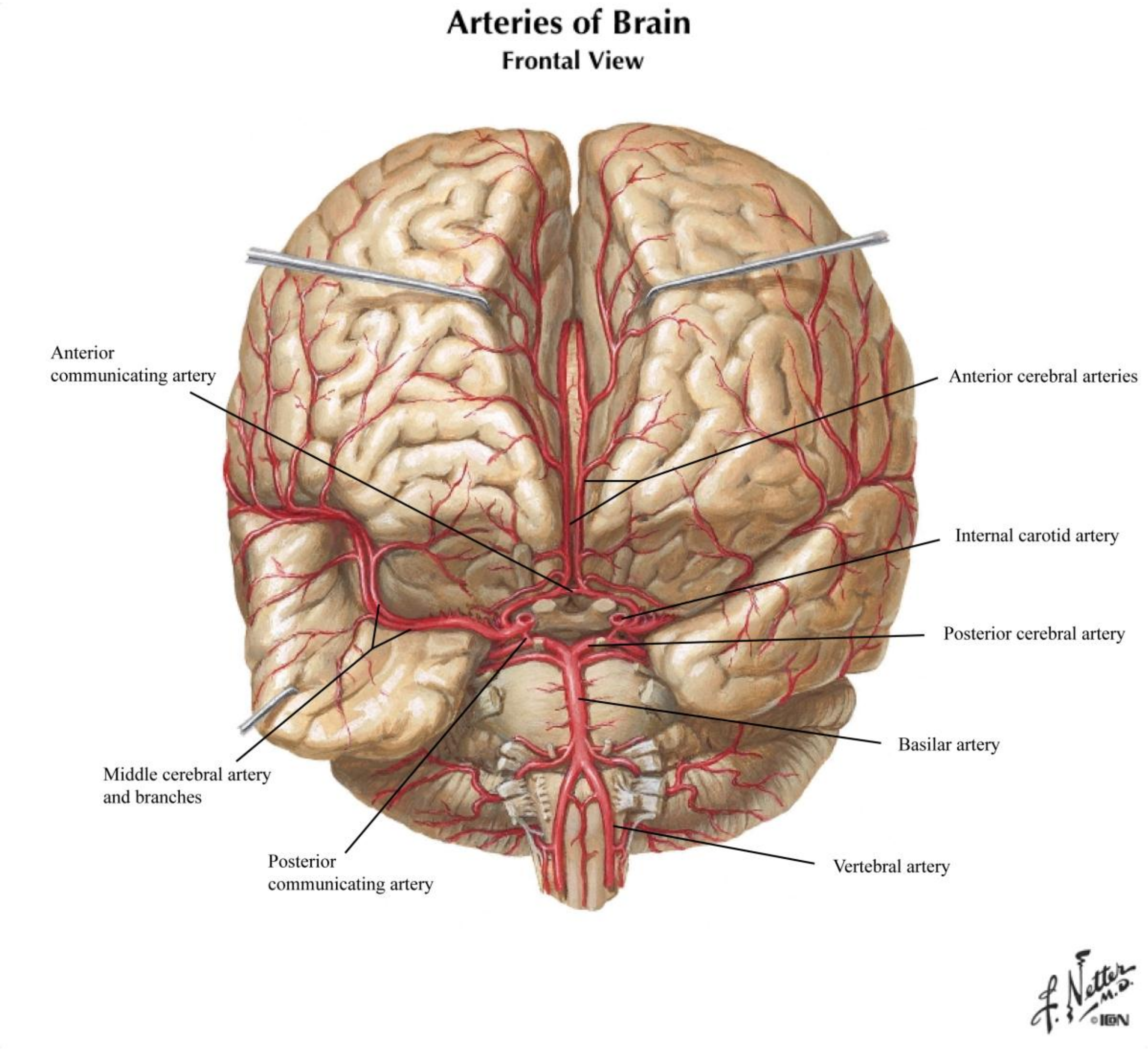

Figure 5-22: Main arteries of the cerebro-vasculature. Modified from Netter [84].

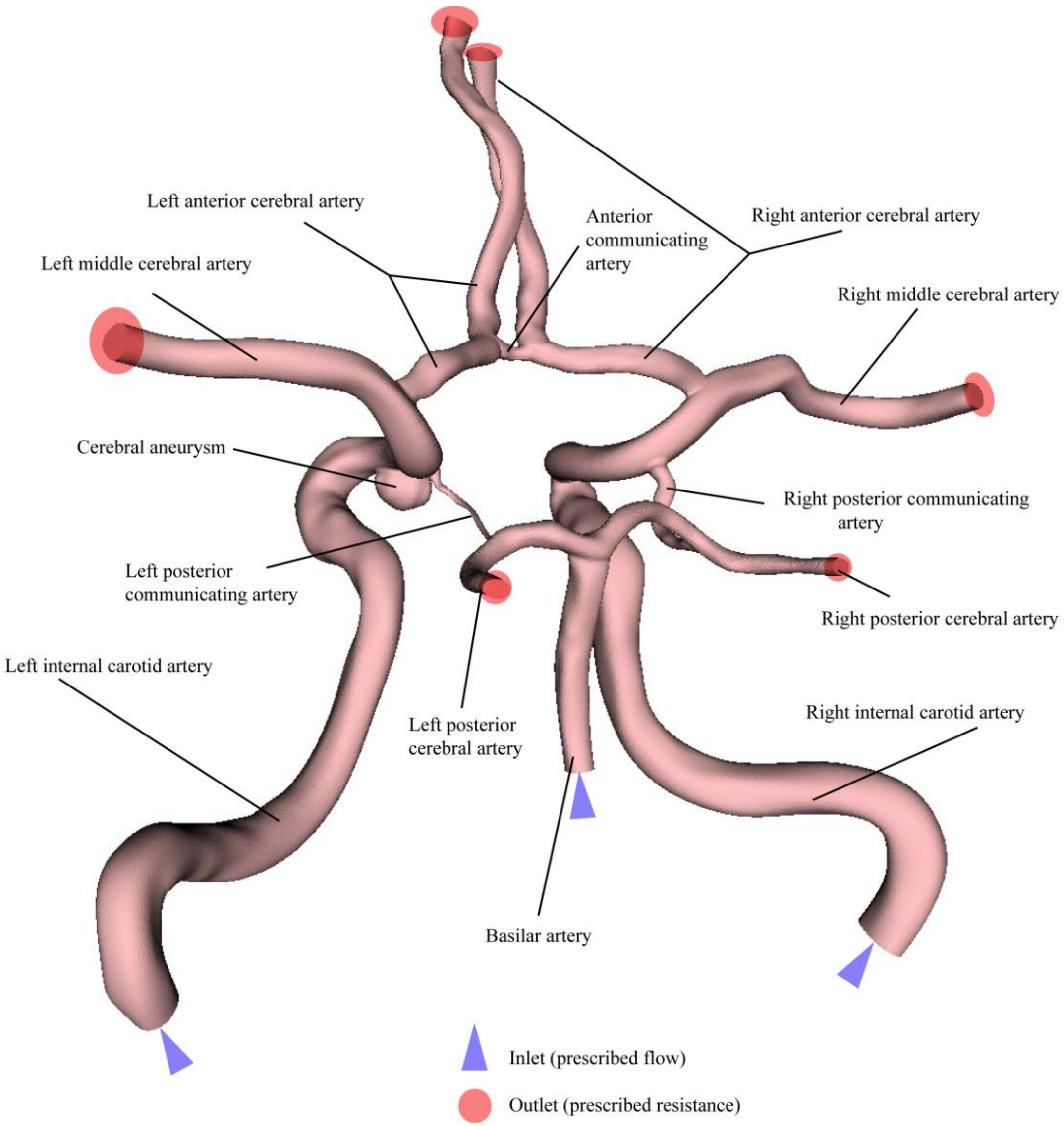

Figure 5-23: Patient-specific model and boundary conditions of a complete circle of Willis with a saccular aneurysm.

Figure 5-23 shows the patient-specific model considered in this section. The model corresponds to an adult subject with a saccular aneurysm in the left internal carotid artery immediately proximal to the circle of Willis. We consider the three inlets described before, and a total of six outlets: the anterior cerebral arteries (left and right), middle cerebral arteries (left and right), and posterior cerebral arteries (also left and right). The model at hand presents a complete circle of Willis, although the left posterior communicating artery is very small and probably does not carry much flow.

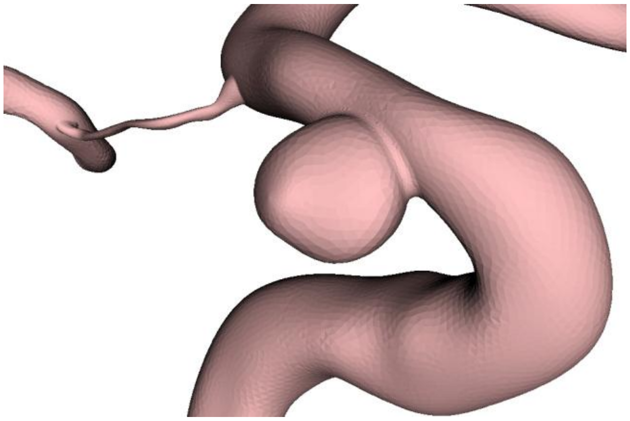

Figure 5-24: Close-up view of the saccular aneurysm present in the left internal carotid artery of the model.

A close-up view of the saccular aneurysm present in the left internal carotid artery of the model can be seen in Figure 5-24.

For this problem, the geometry was obtained from magnetic resonance imaging data. The left and right internal carotid and basilar artery flow rates were prescribed based on the literature [85]. The cardiac cycle is T=1.1 s. We utilized resistance boundary conditions with pressure offset for all six outlet faces of the model. The resistance and pressure offset values imposed at each outlet face are shown in Table 5-8. These values were prescribed after performing an iterative process in order to obtain a physiologic distribution of flow and pressure. This process can be streamlined by using optimization algorithms to obtain the values of the parameters of the outflow boundary conditions that best mimic physiologic data [86].

	Left Middle	Right Middle	Left Post	Right Post	Left Ant	Right Ant
Resistances R ($\mathrm{dyn}\cdot\mathrm{s}\cdot\mathrm{cm}^{-5}$)	25,132.22	32,304.98	25,179.05	24,324.32	10,000.00	10,500.00
Pressure Offsets p_0 ($\mathrm{dyn/cm^2}$)	57,783.80	57,783.80	72,000.00	72,000.00	85,000.00	85,000.00

Table 5-8: Resistances and pressure offset ($p = p_0 + Q \cdot R$) imposed at the outlet faces of the model.

The Young's modulus of the vessel wall was prescribed to be $5.92 \cdot 10^6$ dynes/cm^2. The Poisson's ratio was set to 0.5, the wall density 1.0 g/cm^3, the shear correction parameter k is 5/6, and the mean wall thickness is 0.01 cm. The assignment of these parameters can be further improved upon availability of experimental data. The vessel wall is kept fixed by constraining the degrees-of-freedom of the nodes located at the inlet and outlet rings. The solution was obtained using a 1,012,145 element and 203,452 node mesh with a time step of 0.25 ms, 5 nonlinear iterations per time step, and two cardiac cycles. This problem was solved on a SGI Altix computer using 54 processors and required a modest increase in computational effort (about 2-3 times) over that required to solve the rigid wall problem.

Figure 5-25 shows a volume-rendering of the blood flow velocity magnitude and a surface rendering of the pressure at peak-systole and mid-diastole. Figure 5-26 shows the flow and pressure waves obtained at different inlet and outlet faces of the model.

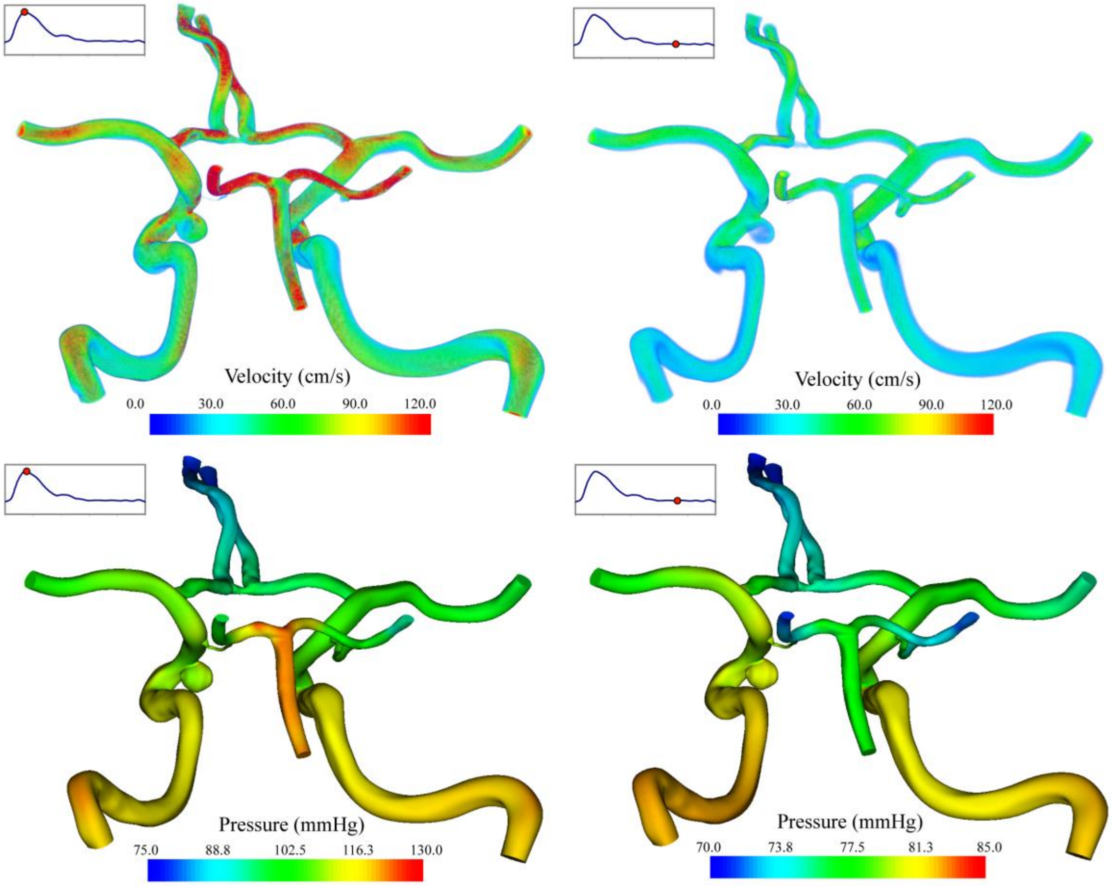

Figure 5-25: Volume-rendering of the velocity field (top) and surface rendering of the pressure (bottom) at peak-systole (left) and mid-diastole (right).

Note that the values of the pressure solution are within the physiologically-relevant range. Furthermore, the flow waves show a unique characteristic of deformable wall simulations: the phase lag of the different curves illustrating the finite wave propagation speed in the computational domain.

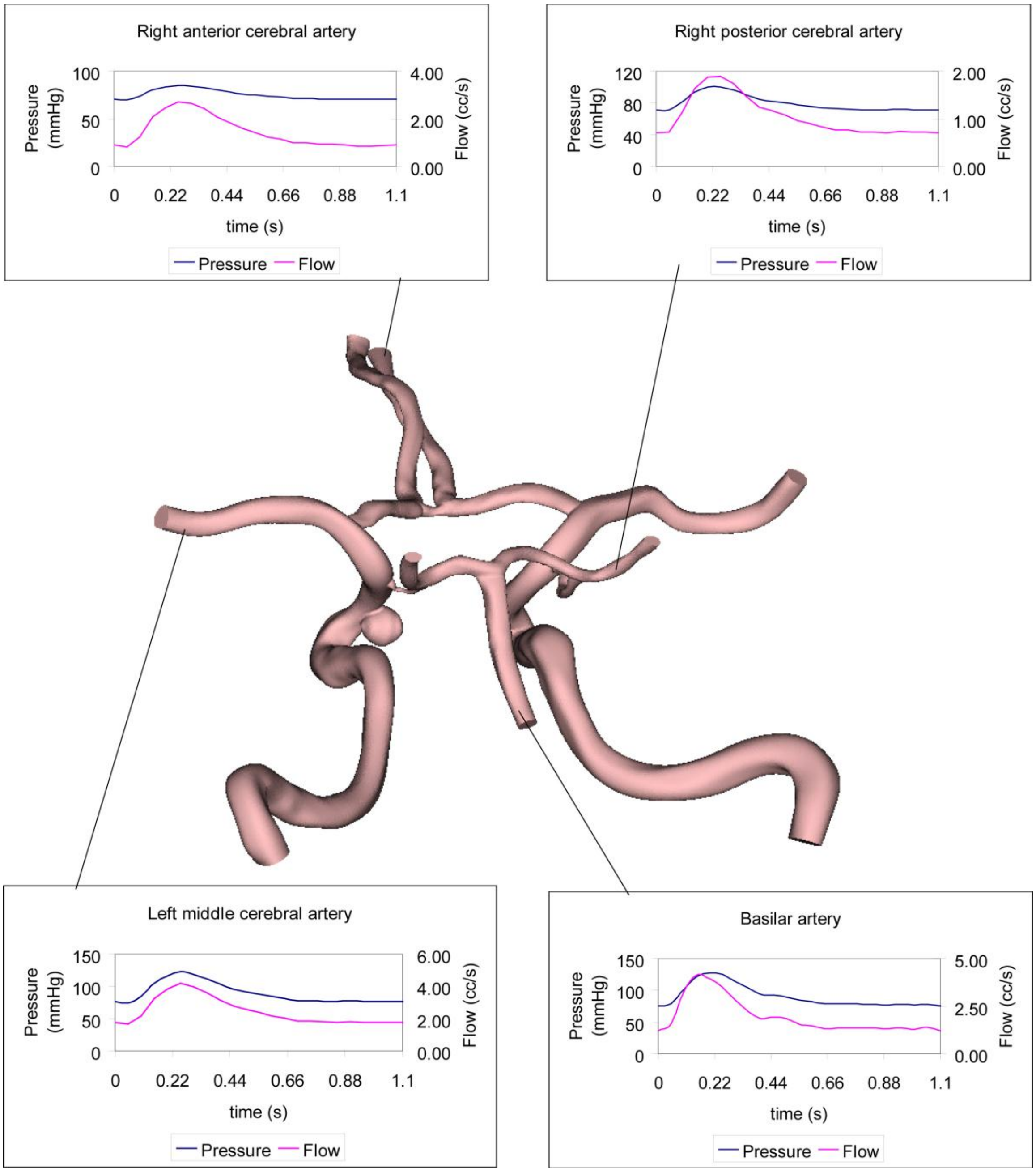

Figure 5-26: Flow and pressure waves at different inlet and outlet faces of the circle of Willis model.

Figure 5-27 shows a close-up view of the blood velocity magnitude, wall shear stress and vessel wall displacement fields around the saccular aneurysm at two different points of the cardiac cycle: peak-systole (left panels) and mid-diastole (right panels).

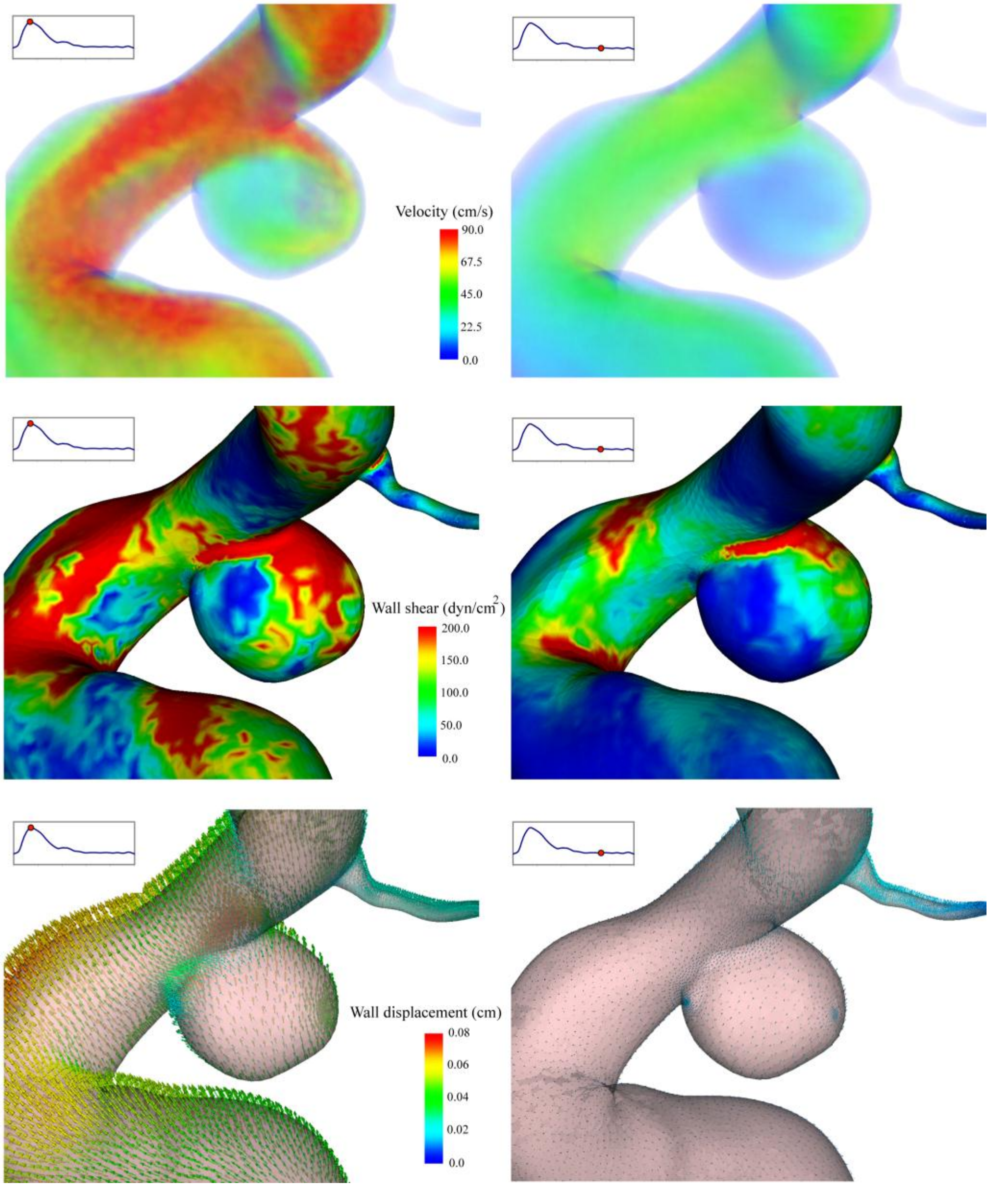

Figure 5-27: Close-up view of the blood velocity magnitude, wall shear stress and wall displacement fields around the saccular aneurysm at two different times in the cardiac cycle: peak-systole (left) and mid-diastole (right).

We can observe that the variations in these fields during the cycle are remarkable. The accurate description of these magnitudes, together with the pressure, is crucial in order to represent the loads the blood flow is exerting on the wall. The tensile stress in the aneurysm wall is determined by the blood pressure, the wall shear stress and the dynamic inertial forces acting on the wall.

5.9 Clinical Relevance of the Application Examples

The results presented in this chapter show great promise for the application of computational methods representing fluid-solid interactions to clinically-relevant problems. We can now study the behavior of deformable, patient-specific cardiovascular models at realistic levels of pressure, with realistic material properties and therefore have access to a number of different fields that are interesting to physicians and biologists: flow velocities, flow distribution, pressure, wall deformation, wall shear stress and wall tensile stress.

The methods in this thesis can be applied to a number of other biologically and clinically relevant problems, including:

1. Investigating hemodynamic factors in the localization of atherosclerosis in the carotid artery, coronary arteries, and abdominal aorta.
2. Quantifying shear and tensile stress in vascular bypass junctions.
3. Quantifying forces acting on endovascular devices.

4. Optimization of surgical procedures.

Finally, as discussed in the next chapter, additional improvements to the methods described in this thesis could open up new horizons in vascular disease research, device design and treatment planning.

Chapter 6

Chapter 6. Conclusions and Future Work

6.1 Conclusions

In this thesis, we described a novel algorithm to model blood flow and vessel motion in large, patient-specific models of the cardiovascular system. We were motivated to reduce the computational cost associated with standard ALE formulations when applied to such large-scale models. By reducing the computational cost of the simulations, we can investigate applications related to disease-research and simulation-based medical planning in a clinically-relevant time frame.

The method developed in this thesis couples the equations of the deformation of the wall with the equations governing the fluid motion using basic assumptions of a thin-walled structure. Furthermore, the coupling is done in such a way that the degrees-of-freedom of the wall and the fluid boundary are enforced to be identical. While ALE formulations can take advantage of the computational efficiencies of a fixed mesh simply by freezing the mesh update, this approach still requires the solution of additional equations representing the wall mechanics. However, the method we have proposed, using a transverse-shear stabilized membrane, does not necessitate the solution of any additional equations or inclusion of degrees of freedom beyond those of the wall fluid velocity. This greatly simplifies the development of the model, enables a pure fluids code to be generalized to include wave propagation and represents a computationally efficient alternative to ALE formulations for modeling blood flow in large deformable models of the vasculature. While our method will not produce results that are equivalent to ALE since, in its current implementation, we utilize a fixed fluid mesh and linearized kinematics, the algorithmic simplicity enables the solution of larger portions of the vasculature as is often required in surgical planning.

We have shown the application of the method to several geometries. The first one was an idealized model of a carotid artery. The simplicity of this geometry provides a clear interpretation of the results, and stresses the fundamental differences in the pressure and flow fields obtained with rigid and deformable wall formulations. Furthermore, this problem illustrates the importance of having adequate boundary conditions to provide the right level of pressure to the vessel wall. With the second geometry, an idealized model of a carotid stenosis with 75% and 88% area reductions, we have demonstrated the robustness of the method when applied to problems featuring complex, transitional velocity fields. In addition, we have also shown that the method is able to qualitatively represent the vessel wall behavior under high-frequency loads demonstrating the potential to be applied to many biological problems. This is further illustrated with a number of large patient-specific models of the vasculature, including a healthy adult abdominal aorta model, a thoracic aorta coarctation model, an abdominal aortic aneurysm model and a model of a complete circle of Willis. We have demonstrated that these complicated geometries can be easily solved with a small increase in computational effort (about 2-3 times) with respect to rigid wall formulations. This relatively small increase in computational time with respect to rigid wall formulations can be further improved by exploring specific linear algebra pre-conditioners for deformable wall problems, since all the results presented here have been obtained using the pre-conditioner scheme of rigid wall formulations.

In addition to applying the method to the examples described above, we have also verified it against Womersley's theoretical model for pulsatile flow in a cylindrical deformable vessel, showing an excellent agreement with the analytical solution.

6.2 Future Work

Further work is needed to improve and validate the method as presented here. The physical description of the vessel wall can be improved by incorporating spatially-varying material properties for the wall, namely the tensor of material parameters, the vessel wall thickness ζ , and the initial stress of the wall. The elasticity of the vessel wall varies depending on the ratio of collagen and elastin fibers in the tissue. For example, the abdominal aorta is stiffer than the thoracic aorta because the ratio of elastin to collagen decreases [25,87]. The vessel wall constitutive equation needs to be expanded to consider anisotropy, since arteries show different behaviors in the circumferential and axial directions [63,88].

Extension of the wall constitutive equation to include viscoelastic effects involves no essential complications and will enable the inclusion of additional physical dissipation in the mathematical model. Experimental evidence shows that wall viscoelasticity is an important source of dissipation. Indeed, this is manifest by damping and dispersion of the pressure and flow waves, and results in a distinct time lag between the pressure and radial deformation waves in the large arteries [89].

The stiffness effects of the surrounding tissue on the vessel wall can be represented by an elastic foundation – a Winkler model [65]: this is similar to Womersley's approach to the incorporation of the elastic constraints of the surrounding tissue on the vessel wall [73].

It is also possible to improve the behavior of the enhanced membrane model of the vessel wall in regions of significant bending using rotation-free shell triangles as proposed by Oñate and Zárate [90].

In this thesis, we have presented the linearized kinematics implementation of the method. However, keeping the domain fixed is not a requirement of the formulation. For the first, and arguably simplest, implementation of the Coupled-Momentum Method, we have fixed the fluid domain for computational efficiency and since this approach requires the fewest changes to a standard finite element fluids solver. However, the method as given by equation (3.34) could be expanded to moving grids, and the structure could be generalized to include large displacements and nonlinear material models. In this case, while we could still embed the solid degrees of freedom into the fluid equations, we would have to update the fluid mesh. In doing so, we would likely lose some of the advantages in the computational efficiency of our current method and will effectively transform it into an ALE formulation with a monolithic treatment of the fluid-solid boundary interface degrees-of-freedom.

Additional work is needed to improve the boundary conditions of both the fluid and the solid domains. The fixed inlet and outlet rings of the vessel wall add artificial wave reflections in the structure. This constraint can be removed by prescribing velocity profiles at the inlet rings using Womerseley's elastic wave theory and traction conditions at the outlet rings of the model. Further work is required to combine the deformable wall formulation presented here with more sophisticated outflow boundary conditions (i.e., impedance or one-dimensional linear and nonlinear wave theory) in order to further improve the simulation of wave propagation in three-dimensional models of the vasculature [24].

A thorough study of turbulence is necessary in order to better assess the flow characteristics present in complex geometries such as stenosis or aneurysms. The transitional nature of the flow in these models precludes using standard turbulence models derived in many cases for situations of fully developed turbulence.

Finally, the method should be compared with other more general numerical formulations, like ALE methods, and validated with *in vitro* and *in vivo* experiments. While experiment validation studies are challenging to conduct, it is only by comparison with such data that the ultimate realism of this method will be discerned.

In closing, the goal of this Ph.D. research, to develop a mathematical formulation to enable the solution of large scale patient-specific deformable models of the vasculature with computational costs similar to those of rigid wall formulations, has been attained. We expect that the application of this method to cardiovascular research will eliminate the use of rigid wall formulations in the future. We anticipate that, as more physiologic data characterizing the mechanical behavior of the vessel wall and surrounding tissues becomes available, this method can enable the simulation of vascular models as large as needed in order to represent the parts of the cardiovascular where the three-dimensional features of the flow are important.

Chapter 7. Bibliography

[1] AHA, 2001 heart and stroke statistical update. Dallas, Texas, American Heart Association (2000).

[2] C.K. Zarins, D.P. Giddens, B.K. Bharadvaj, V.S. Sottiurai, R.F. Mabon and S. Glagov, Carotid bifurcation atherosclerosis quantitative correlation of plaque localization with flow velocity profiles and wall shear-stress, Circulation Research 53(4) (1983) 502-514.

[3] D.N. Ku, D.P. Giddens, C.K. Zarins and S. Glagov, Pulsatile flow and atherosclerosis in the human carotid bifurcation positive correlation between plaque location and low and oscillating shear stress, Arteriosclerosis 5(3) (1985) 293-302.

[4] M.H. Friedman, G.M. Hutchins, C.B. Bargeron, O.J. Deters and F.F. Mark, Correlation between intimal thickness and fluid shear in human arteries, Atherosclerosis 39(3) (1981) 425-436.

[5] M.H. Friedman, C.B. Bargeron, O.J. Deters, G.M. Hutchins and F.F. Mark, Correlation between wall shear and intimal thickness at a coronary artery branch, Atherosclerosis 68(1-2) (1987) 27-33.

[6] K. Perktold, M. Resch and R.O. Peter, Three-dimensional Numerical Analysis of pulsatile flow and wall shear stress in the carotid artery bifurcation, Journal of Biomechanics 24(6) (1991) 409-420.

[7] D.A. Steinman, Image-based computational fluid dynamics modeling in realistic arterial geometries, Annals of Biomedical Engineering 30(4) (2002) 483-497.

[8] C.A. Taylor, T.J.R. Hughes and C.K. Zarins, Finite Element modeling of three-dimensional pulsatile flow in the abdominal aorta: Relevance to atherosclerosis, Annals of Biomedical Engineering 26(6) (1998) 1-14.

[9] J.F. LaDisa, Jr., I. Guler, L.E. Olson, D.A. Hettrick, J.R. Kersten, D.C. Warltier and P.S. Pagel, Three-dimensional computational fluid dynamics modeling of alterations in coronary wall shear stress produced by stent implantation, Annals of Biomedical Engineering 31(8) (2003) 972-980.

[10] X. Song, A.L. Throckmorton, H.G. Wood, P.E. Allaire and D.B. Olsen, Transient and quasi-steady computational fluid dynamics study of a left ventricular assist device, ASAIO J 50(5) (2004) 410-417.

[11] G.R. Stuhne and D.A. Steinman, Finite-element modeling of the hemodynamics of stented aneurysms, Transactions of the ASME. Journal of Biomechanical Engineering 126(3) (2004) 382-387.

[12] M.R. de Leval, G. Dubini, F. Migliavacca, H. Jalali, G. Camporini, A. Redington and R. Pietrabissa, Use of computational fluid dynamics in the design of surgical procedures: Application to the study of competitive flows in cavo-pulmonary connections, Journal of Thoracic and Cardiovascular Surgery 111(3) (1996) 502-513.

[13] K. Lagana, G. Dubini, F. Migliavacca, R. Pietrabissa, G. Pennati, A. Veneziani and A. Quarteroni, Multiscale modelling as a tool to prescribe realistic boundary conditions for the study of surgical procedures, Biorheology 39(3-4) (2002) 359-364.

[14] F. Migliavacca, P.J. Kilner, G. Pennati, G. Dubini, R. Pietrabissa, R. Fumero and M.R. de Leval, Computational fluid dynamic and magnetic resonance analyses of flow distribution between the lungs after total cavopulmonary connection, IEEE Transactions on Biomedical Engineering 46(4) (1999) 393-399.

[15] C.A. Taylor, M.T. Draney, J.P. Ku, D. Parker, B.N. Steele, K. Wang and C.K. Zarins, Predictive medicine: Computational techniques in therapeutic decision-making, Computer Aided Surgery 4(5) (1999) 231-247.

[16] C.A. Taylor, T.J.R. Hughes and C.K. Zarins, Finite Element modeling of blood flow in arteries, Computer Methods in Applied Mechanics and Engineering 158 (1998) 155-196.

[17] M. Oshima, R. Torii, T. Kobayashi, N. Taniguchi and K. Takagi, Finite Element simulation of blood flow in the cerebral artery, Computer Methods in Applied Mechanics and Engineering 191(6-7) (2001) 661-671.

[18] J.R. Cebral, M.A. Castro, O. Soto, R. Lohner and N. Alperin, Blood-flow models of the circle of Willis from magnetic resonance data, Journal of Engineering Mathematics 47(3-4) (2003) 369-386.

[19] M. Shojima, M. Oshima, K. Takagi, R. Torii, M. Hayakawa, K. Katada, A. Morita and T. Kirino, Magnitude and role of wall shear stress on cerebral aneurysm - computational fluid dynamic study of 20 middle cerebral artery aneurysms, Stroke 35(11) (2004) 2500-2505.

[20] S. Salmon, M. Thiriet and J.F. Gerbeau, Medical image-based computational model of pulsatile flow in saccular aneurisms, Mathematical Modelling and Numerical Analysis 37(4) (2003) 663-679.

[21] K. Perktold and G. Rappitsch, Computer simulation of local blood flow and vessel mechanics in a compliant carotid artery bifurcation model, Journal of Biomechanics 28(7) (1995) 845-856.

[22] F.N. van de Vosse, J. de Hart, C.H.G.A. van Oijen, D. Bessems, T.W.M. Gunther, A. Segal, B.J.B.M. Wolters, J.M.A. Stijnen and F.P.T. Baaijens, Finite-Element-based computational

methods for cardiovascular fluid-structure interaction, Journal of Engineering Mathematics 47(3/4) (2003) 335-368.

[23] L. Formaggia, J.F. Gerbeau, F. Nobile and A. Quarteroni, On the coupling of 3D and 1D Navier-Stokes equations for flow problems in compliant vessels, Computer Methods in Applied Mechanics and Engineering 191(6/7) (2001) 561-582.

[24] I.E. Vignon-Clementel, C.A. Figueroa, K.E. Jansen and C.A. Taylor, Outflow boundary conditions for three-dimensional Finite Element modeling of blood flow and pressure in arteries, accepted for publication in Computational Methods in Applied Mechanics and Engineering (2006).

[25] W.W. Nichols and M.F. O'Rourke, McDonald's blood flow in arteries: Theoretical, experimental and clinical principles. (1998) New York, Oxford University Press.

[26] L. De Pater and J. Van Den Berg, An electric analogue of the entire human circulatory system, Medical electronics and biological engineering 2 (1964) 161-166.

[27] N. Westerhof, F. Bosman, C.J. De Vries and A. Noordergraaf, Analog studies of the human systemic arterial tree, Journal of Biomechanics 2 (1969) 121-143.

[28] V. Milisic and A. Quarteroni, Analysis of lumped parameter models for blood flow simulations and their relation with 1D models, ESAIM-Mathematical Modelling and Numerical Analysis-Modelisation Mathematique et Analyse Numerique 38(4) (2004) 613-632.

[29] T.J.R. Hughes and J. Lubliner, On the one-dimensional theory of blood flow in the larger vessels, Mathematical Biosciences 18(1-2) (1973) 161-170.

[30] J. Wan, B.N. Steele, S.A. Spicer, S. Strohband, G.R. Feijoo, T.J.R. Hughes and C.A. Taylor, A one-dimensional Finite Element Method for simulation-based medical planning for cardiovascular disease, Computer Methods in Biomechanics and Biomedical Engineering 5(3) (2002) 195-206.

[31] L. Formaggia, D. Lamponi and A. Quarteroni, One-dimensional models for blood flow in arteries, Journal of Engineering Mathematics 47(3/4) (2003) 251-276.

[32] S.J. Sherwin, L. Formaggia, J. Peiro and V. Franke, Computational modelling of 1D blood flow with variable mechanical properties and its application to the simulation of wave propagation in the human arterial system, International Journal for Numerical Methods in Fluids 43(6-7) (2003) 673-700.

[33] T.J.R. Hughes, W.K. Liu and T.K. Zimmermann, Lagrangian-Eulerian Finite Element formulation for incompressible viscous flows, Computer Methods in Applied Mechanics and Engineering 29 (1981) 329-349.

[34] J. Donea, S. Giuliani and J.P. Halleux, An Arbitrary Lagrangian-Eulerian Finite Element method for transient dynamic fluid-structure interactions, Computer Methods in Applied Mechanics and Engineering 33(1-3) (1982) 689-723.

[35] T.E. Tezduyar, M. Behr and J. Liou, A new strategy for finite element computations involving moving boundaries and interfaces--the deforming-spatial-domain/space-time procedure: I. The concept and the preliminary numerical tests, Computer Methods in Applied Mechanics and Engineering 94(3) (1992) 339-351.

[36] S. Mittal and T.E. Tezduyar, Massively parallel finite element computation of incompressible flows involving fluid-body interactions, Computer Methods in Applied Mechanics and Engineering 112(1-4) (1994) 253-282.

[37] C. Farhat, P. Geuzaine and C. Grandmont, The discrete geometric conservation law and the nonlinear stability of ALE schemes for the solution of flow problems on moving grids, Journal of Computational Physics 174(2) (2001) 669-694.

[38] C. Farhat and P. Geuzaine, Design and analysis of robust ALE time-integrators for the solution of unsteady flow problems on moving grids, Computer Methods in Applied Mechanics and Engineering 193(39-41) (2004) 4073-4095.

[39] P. Le Tallec and J. Mouro, Fluid structure interaction with large structural displacements, Computer Methods in Applied Mechanics and Engineering 190(24-25) (2001) 3039-3067.

[40] A. Leuprecht, K. Perktold, M. Prosi, T. Berk, W. Trubel and H. Schima, Numerical study of hemodynamics and wall mechanics in distal end-to-side anastomoses of bypass grafts, Journal of Biomechanics 35(2) (2002) 225-236.

[41] A. Leuprecht, S. Kozerke, P. Boesiger and K. Perktold, Blood flow in the human ascending aorta: A combined MRI and CFD study, Journal of Engineering Mathematics 47(3/4) (2003) 387.

[42] M. Heil, An efficient solver for the fully coupled solution of large-displacement fluid-structure interaction problems, Computer Methods in Applied Mechanics and Engineering 193(1-2) (2004) 1-23.

[43] A. Quarteroni, M. Tuveri and A. Veneziani, Computational vascular fluid dynamics: Problems, models and methods, Computing and Visualization in Science 2(4) (2000) 163-197.

[44] C. Grandmont and Y. Maday, Fluid-Structure Interaction: A theoretical point of view. (2003) London, Kogan Page Science.

[45] J. De Hart, F.P.T. Baaijens, G.W.M. Peters and P.J.G. Schreurs, A computational fluid-structure interaction analysis of a fiber-reinforced stentless aortic valve, Journal of Biomechanics 36(5) (2003) 699-712.

[46] C.S. Peskin and D.M. McQueen, A general method for the computer simulation of biological systems interacting with fluids, Symposia Soc. Experimental Biology 49 (1995) 265-276.

[47] M.A. Fernandez and P. Le Tallec, Linear stability analysis in fluid-structure interaction with transpiration. Part II: Numerical analysis and applications, Computer Methods in Applied Mechanics and Engineering 192(43) (2003) 4837-4873.

[48] S. Deparis, M.A. Fernandez and L. Formaggia, Acceleration of a fixed point algorithm for fluid-structure interaction using transpiration conditions, Mathematical Modelling and Numerical Analysis 37(4) (2003) 601-616.

[49] K.E. Jansen, Parallel Hierarchic Adaptive Stabilized Transient Analysis (PHASTA), Scientific Computation Research Center. Rensselaer Polytechnic Institute.

[50] M. Zamir, The physics of pulsatile flow. (2000) London, Ontario, Springer-Verlag.

[51] J. Womersley, An elastic tube theory of pulse transmission and oscillatory flow in mammalian arteries, Wright Air Development Center, Air Research and Development Command, United States Air Force, Wright-Patterson Air Force Base, Ohio (1957).

[52] F. Nobile, Numerical approximation of fluid-Structure Interaction problems with application to haemodynamics, École Polytechnique Fédérale de Lausanne (2001).

[53] H. Morand and R. Ohayon, Fluid Structure Interaction. Applied Numerical Methods. (1995) Paris, Wiley.

[54] C. Michler, E.H. van Brummelen and R. de Borst, An interface newton-krylov solver for fluid-structure interaction, International Journal for Numerical Methods in Fluids 47(10-11) (2005) 1189-1195.

[55] M. Heil and O.E. Jensen, Flows in deformable tubes and channels. Theoretical models and biological applications. Flow in collapsible tubes and past other highly compliant boundaries. P. W. Carpenter and T. J. Pedley.(2003) Dordrecht, The Netherlands, Kluwer: 15-50.

[56] J.-F. Gerbeau, M. Vidrascu and P. Frey, Fluid-structure interaction in blood flows on geometries based on medical imaging, Computers & Structures 83(2-3) (2005) 155-165.

[57] J.R. Womersley, Oscillatory motion of a viscous liquid in a thin walled elastic tube-I: The linear approximation for long waves, The Philosophical Magazine 7 (1955) 199-221.

[58] C.H. Whiting and K.E. Jansen, A Stabilized Finite Element Method for the incompressible Navier-Stokes equations using a hierarchical basis, International Journal for Numerical Methods in Fluids 35 (2001) 93-116.

[59] P.M. Gresho and R.L. Sani, Incompressible flow and the Finite Element method. (2000), Wiley.

[60] T.J.R. Hughes, L.P. Franca and M. Balestra, New Finite Element formulation for computational fluid dynamics: V. Circumventing the Babuska-Brezzi condition: A stable Petrov-Galerkin formulation of the Stokes problem accomodating equal-order interpolations, Computer Methods in Applied Mechanics and Engineering 59(1) (1986) 85-99.

[61] L.P. Franca and S.L. Frey, Stabilized Finite Element methods. II. The incompressible Navier-Stokes equations, Computer Methods in Applied Mechanics and Engineering 99(2/3) (1992) 209-233.

[62] F. Shakib, Finite Element Analysis of the compressible euler and Navier-Stokes equations, PhD Thesis, Stanford University (1988).

[63] Y.-C. Fung and J. Zhou, The degree of nonlinearity and anisotropy of blood vessel elasticity, Proceedings National Academy of Sciences 94 (1997) 14255-14260.

[64] P. Causin, J.F. Gerbeau and F. Nobile, Added-mass effect in the design of partitioned algorithms for fluid-structure problems, Computer Methods in Applied Mechanics and Engineering 194(42-44) (2005) 4506-4527.

[65] T.J.R. Hughes, The Finite Element Method. Linear static and dynamic Finite Element Analysis. (2000) New York, Dover.

[66] R.D. Cook, D.S. Malkus, M.E. Plesha and R.J. Witt, Concepts and applications of Finite Element Analysis. (2002) New York, John Wiley & Sons.

[67] F. Shakib, Acusolve, http://www.acusim.com.

[68] K.E. Jansen, C.H. Whiting and G.M. Hulbert, Generalized-alpha method for integrating the filtered Navier-Stokes equations with a stabilized Finite Element method, Computer Methods in Applied Mechanics and Engineering 190(3-4) (2000) 305-319.

[69] J. Chung and G.M. Hulbert, A time integration algorithm for structural dynamics with improved Numerical dissipation: The Generalized-alpha Method, Journal of Applied Mechanics 60 (1993) 371-375.

[70] C.W. Gear, Numerical initial value problems in ordinary differential equations. (1971), Prentice-Hall, Inc., Englewood Cliffs, N.J.

[71] I. Babuska and J. Oden, Verification and validation in computational engineering adn science: Basic concepts, Computer Methods in Applied Mechanics and Engineering 193 (2004) 4057-4066.

[72] I. Vignon and C.A. Taylor, Outflow boundary conditions for one-dimensional Finite Element modeling of blood flow and pressure waves in arteries, Wave Motion 39(4) (2004) 361-374.

[73] J.R. Womersley, Oscillatory flow in arteries: The constrained elastic tube as a model of arterial flow and pulse transmission, Physics in Medicine and Biology 2 (1957) 178-187.

[74] R.L. Maurice, J. Ohayon, Y. Fretigny, M. Bertrand, G. Soulez and G. Cloutier, Noninvasive vascular elastography: Theoretical framework, IEEE transactions on medical imaging 23(2) (2004) 164-180.

[75] J.R. Cebral, R. Lohner, O. Soto and P.J. Yim, On the modelling of carotid blood flow from magnetic resonance images, Proceedings of the 2001 Summer Bioengineering Meeting (2001), 619-620.

[76] D.W. Holdsworth, C.J.D. Norley, R. Frayne, D.A. Steinman and B.K. Rutt, Characterization of common carotid artery blood-flow waveforms in normal subjects, Physiological Measurement 20 (1999) 219-240.

[77] W.R. Milnor, Hemodynamics. (1989), Williams & Wilkins.

[78] D.R. Boughner and M.R. Roach, Effect of low frequency vibration on the arterial wall, Circulation Research 29 (1971) 136-144.

[79] J.J. Yeung, H.J. Kim, T.A. Abbruzzese, I.E. Vignon-Clementel, M.T. Draney, J.K. Yeung, I. Karwowski, I. Perkash, R.J. Herfkens, C.A. Taylor and R.L. Dalman, Aortoiliac hemodynamic and morphologic adaptation to chronic spinal cord injury, Circulation (submitted) (2006).

[80] W.F.M. Ganong, Review of medical physiology. (1995) Englewood Cliffs, Appleton & Lange.

[81] A.C. Guyton, M.D., Physiology of the human body. (1984) San Francisco, Saunders College Publishing.

[82] J.D. Humphrey and P.B. Canham, Structure, mechanical properties, and mechanics of intracranial saccular aneurysms, Journal of Elasticity 61(1 - 3) (2000) 49-81.

[83] J.D. Humphrey and K.R. Rajagopal, A constrained mixture model for growth and remodeling of soft tissues, Mathematical models & methods in applied sciences 12(3) (2002) 407-430.

[84] F.H. Netter, Atlas of human anatomy. (1997) New Jersey, Icon Learning Systems.

[85] J. Hendrikse, A.F. van Raamt, Y. van der Graaf, Y.W. Mali and J.W. van der Grond, Distribution of cerebral blood flow in the circle of Willis, Radiology 235(1) (2005) 184-189.

[86] R.L. Spilker, J.A. Feinstein, D.W. Parker, V.M. Reddy and C.A. Taylor, Morphometry-based impedance boundary conditions for patient-specific modeling of blood flow in pulmonary arteries, Annals of Biomedical Engineering (submitted) (2006).

[87] H. Wolinsky and S. Glagov, Comparison of abdominal and thoracic aortic medial structure in mammals. Deviation of man from the usual pattern, Circulation Research 25(6) (1969) 677-686.

[88] J.D. Humphrey, Cardiovascular solid mechanics. Cells, tissues and organs. (2002) New York, Springer.

[89] R. Holenstein, P. Niederer and M. Anliker, A viscoelastic model for use in predicting arterial pulse waves, Journal of Biomechanical Engineering 102(4) (1980) 318-325.

[90] E. Oñate and F. Zárate, Rotation-free triangular plate and shell elements, International Journal for Numerical Methods in Engineering 47(1) (2000) 557-603.